J Mater Sci (2006) 41:6547–6590
DOI 10.1007/s10853-006-0197-2

Multi-scale modeling, stress and failure analyses of 3-D woven composites

A. E. Bogdanovich

Abstract The very complex, multi-level hierarchical construction of textile composites and their structural components commonly manifests via significant property variation even at the macro-level. The concept of a ‘‘meso-volume’’ (introduced by this author in early 1990s) is consistently applied in this work to 3-D stress/strain and failure analyses of 3-D woven composites at several levels of structural hierarchy. The meso-volume is defined as homogeneous, anisotropic block of composite material with effective elastic properties determined through volumetrically averaged 3-D stress and strain fields computed at a lower (‘‘finer’’) level of structural hierarchy and application of generalized Hooke’s law to the averaged fields. The meso-volume can represent a relatively large, homogenized section of a composite structural component, a lamina in laminated composite structure, a homogenized assembly of several textile composite unit cells, a single homogenized unit cell, a resin-impregnated yarn, a single carbon fiber, even a carbon nanotube assembly. When composed together, distinct meso-volumes constitute a 3-D Mosaic model at the respective hierarchy level. A multi-scale methodology presented in this paper first illustrates 3-D stress/strain analysis of the Mosaic unidirectional composite, computation of its effective elastic properties and their further use in 3-D stress/strain analysis of the Mosaic model of 3-D woven composite Unit Cell. The obtained 3-D stress/strain fields are then volumetrically averaged within the Unit Cell, and its effective elastic properties are computed. The predicted effective elastic properties of 3-D woven composite are compared with experimental data and show very good agreement. Further, those effective elastic properties are used in 3-D simulations of three-point bending tests of 3-D woven composite; theoretical predictions for central deflection show excellent agreement with experimental data. Finally, a 3-D progressive failure analysis of generic 3-D Mosaic structure is developed using ultimate strain criterion and illustrated on the 3-D woven composite Unit Cell. The predicted strength values are compared to experimental results. The presented comparisons of theoretical and experimental results validate the adequacy and accuracy of the developed material models, mathematical algorithms, and computational tools.

Introduction

Many performance benefits, manufacturing advantages and cost reduction opportunities offered by modern 3-D woven textile preforms for composites (which were addressed in many recent publications, see [1–12] for example), are now well understood and appreciated. The performance benefits include controllable suppression of delamination, dramatically improved fracture toughness, damage tolerance, impact and ballistic resistance, reduced notch sensitivity, extended fatigue life, etc. The manufacturing advantages primarily manifest through the use of a relatively thick (though sufficiently conformable) single-layer preform instead of a stack of thin, multi-layer tapes or 2-D fabrics, thus allowing to eliminate the labor intensive and time consuming lay-up and stitching operations, minimize cutting and other similar procedures. Particularly, it

A. E. Bogdanovich (✉)
3TEX, Inc., 109 MacKenan Drive, Cary, NC 27511, USA
e-mail: bogdanovicha@3tex.com

was shown in [3] that relatively thick, complex shape composite parts can be machined from standard flat ''billets'' of 3-D woven composites, just like metal parts can be machined from bulk metal. Alternatively, relatively thick complex shape composite parts can be fabricated by infusing polymeric resins into 3-D woven preforms by using vacuum bags or special closed molds, with subsequent cure at room or elevated temperature. Importantly, experimental observations first reported in [2] and then independently confirmed by other investigators, showed that advanced integral 3-D orthogonal woven preforms possess much higher permeability characteristics and, consequently, provide much higher resin infusion rates than equivalent thickness stacks of 2-D fabric preforms. This effect enables to either produce larger composite structures, or reduce resin infusion time, or use higher viscosity resin systems.

In spite of significant progress in the field of 3-D woven preforms and composites, there are certain issues that obstruct a broader and faster penetration of this class of advanced materials into different industrial markets. The following should be mentioned as the major ones: (i) very minimal amount of mechanical characterization data and lack of any considerable property database; (ii) concerns about applicability of traditional mechanical characterization methods (documented as ASTM standards) to this class of materials, and (iii) lack of established, thoroughly validated, computationally efficient and accurate structural analysis and design tools. Indeed, complex and very diverse three-dimensional fiber architectures, their inhomogeneity, significant variability of mechanical characteristics of 3-D textile composites, along with some other features, seriously challenge application of the routine Strength of Materials and Classical Lamination Theory analysis approaches. Yet, these types of analysis are commonly used (often without any doubts or warnings) for processing experimental data, for material property predictions, for structural analysis and design.

Further on, relatively large (typically several mm long, wide, and sometimes also thick) unit cell size in the in-plane and through-thickness directions of textile composites challenges traditional strain measurement methodologies, particularly due to experimental specimens typically contain only few unit cells along the width and thickness. The consequence shows in significant dependency of the measured strains upon the strain gage base length and its location, as discussed and illustrated in [13–16]. Small gages mounted on the specimen surface may incidentally measure local deformation of the yarn, local matrix deformation, or any mixture of the two. Obtaining macroscopic mechanical properties (i.e. ''effective'' elastic and shear moduli, Poisson's ratios) of textile composite from such strain measurement data by using equations which are only applicable to homogeneous materials, with no account of property variability in the width and thickness directions, may not only be methodologically incorrect, but also very inaccurate.

Furthermore, the actual load transfer mechanisms from the grips to the specimen middle zone (in which the strains are actually measured) may be very different from the load transfer mechanisms assumed in the respective ASTM standards. This problem is usually most evident in shear and compressive tests.

Finally, the anticipated ''dominating'' failure mode (if such can be identified at all) of 3-D textile composites is often not realized with the use of specimen dimensions and loading schemes recommended by ASTM standards. This may result in obtaining totally inadequate strength characteristics. The above assessments are based on an extensive practical experience of this author working in the area of 3-D textile preforms and composites for nearly two decades. Some of the aforementioned analytical and experimental issues have been addressed in reference book [15], recent report [17] and papers [18, 19].

Computational modeling, predictive analysis and design optimization of 3-D textile composites constitute a challenging field of research, which includes many distinct topics. Among those are (the sequence below is arbitrary):

i. fabric geometry modeling in free and compressed states
ii. resin flow modeling through textile preforms
iii. elastic property predictions of textile composites
iv. elastic structural response under complex loading cases
v. damage mechanisms, initial and progressive failure modeling, and strength predictions
vi. fatigue life and durability predictions
vii. analysis of stress concentration in the presence of holes, notches, bolts, fasteners, etc.
viii. analysis of bonded joints of different configurations
ix. impact modeling, including theoretical quantification of impact damage
x. compression after impact and other problems associated with damage tolerance
xi. ballistic impact, penetration and perforation phenomena
xii. stress wave propagation and attenuation, damping and energy dissipation
xiii. blast effect prediction and mitigation.

The above list is not exhaustive. In this paper only few of the listed topics are addressed or touched, mainly (i), (iii), (iv), and (v). Very few of the aforementioned topics have been seriously studied for 3-D woven composites; probably (iii), (v), (ix) and (xi) gained most of attention. Geometric modeling of 3-D woven preforms, including conformability and shape variation effects under typical industrial composites fabrication conditions demands much more attention. Recent publications [20, 21] provide examples of advanced theoretical and experimental research in this area. Very few studies have been reported up to date on computational modeling and analysis of 3-D woven composites under impact, ballistic and blast effects, see [22–26].

References [15, 16, 18, 27–48] well represent major theoretical studies of effective elastic properties of 3-D woven fabric composites and elastic response of their structural components. The main challenges in this area of research are determined by the presence of continuous through thickness (commonly called ‘‘Z-directional’’) reinforcement and its substantial effect on the preform architecture and composite material behavior. Due to this essential feature, any modeling/analysis approach has to be three-dimensional, simply because it shall explicitly account for the through-thickness variation of the reinforcement architecture and for the presence of through-thickness fibers. Accordingly, any two-dimensional model or analysis method that is borrowed from the computational toolbox available for thin laminates and based on through-thickness property homogenization, may be inadequate. A review of modeling and analysis methods which are, in principle, applicable to 3-D woven composites, is presented next. It is concluded with state-of-the-art assessments and practical recommendations how to approach modeling and analysis of textile composites in general and 3-D woven composites in particular.

History and state-of-the-art in modeling and analysis of 3-D woven composites

Analytical models and first 3-D finite element analysis

To start this historic overview, one of the pioneering publications [27], which makes the group of its own, has to be briefly analyzed. It presents several analytical and numerical analysis approaches applicable to 3-D orthogonal weave unit cells. The approaches were illustrated on specific numerical examples, and comparison between theoretical and experimental data was provided. The first approach is 3-D finite element analysis with 8-noded hexahedral orthotropic brick element. Today this is, of course, a very common analysis method, however in the mid-1980s is was a rarity. Elastic properties of the elements used in the analysis corresponded to the resin-impregnated graphite fiber tows (which were modeled as unidirectional composites). The second approach (called ‘‘analytical’’) represented the same unit cell as an assemblage of blocks with different material properties connected in series or in parallel. In one variant of this approach, each series of strips was first replaced by a single homogeneous block having effective elastic properties, then all such homogeneous blocks (assembled in parallel) were reduced to a single orthotropic homogeneous block, which represented fully homogenized unit cell of the 3-D orthogonal woven composite. In the other variant of the same analytical approach the first step was to replace each set of parallel slabs by a homogeneous block having effective elastic properties. Then the obtained blocks (assembled in series) were replaced by a single homogeneous orthotropic block corresponding to the entire unit cell. Elastic properties of each homogeneous block were estimated by the use of rule of mixtures or classical lamination theory.

Numerical results presented in the discussed work showed surprisingly good agreement with experimental data for in-plane Young’s moduli and shear moduli. Particularly, results of 3-D finite element analysis deviated from experimental data only by 4.5% for elastic modulus in warp direction, by 1.8% for elastic modulus in fill direction, and by 9.7% for in-plane shear modulus. Considering that fiber waviness was not taken into account, the success of theoretical predictions of effective elastic properties was mainly attributed by authors of [27] to ‘‘the lack of fiber waviness in the orthogonal fabric’’. This early work showed that 3-D orthogonal woven fabrics and composites are very suitable objects for validating various type 3-D modeling and analysis tools.

Orientation Averaging Method

Many works on elastic property predictions of 3-D woven fabric composites, see for example [29, 34, 35, 41, 42], used Orientation Averaging Method (OAM), which includes two versions: Stiffness Averaging Method (SAM) and Compliance Averaging Method (CAM). The first one corresponds to isostrain, while the second one to isostress hypotheses. This theoretical approach was originated at the Institute of Polymer

Mechanics (Riga, Latvia) in the late 1970s, see [49–53]. The general presentation of this approach can be found in [54]. A detailed description of this approach can be also found in books [15, 30] and many articles. Also, the concept of ''blending'' both SAM and CAM in one analysis approach was proposed in [15].

The OAM is relatively simple and it is limited to effective elastic property predictions. Due to its simplicity, most of researchers and engineers dealing with analysis and design of textile composites either developed their own code or have access to a code realizing one or the other version of OAM. Therefore, this analysis approach has some ''universal'' value—many analysts can solve some selected benchmark problem for textile composite and then mutually compare the obtained results. Another advantage of this approach is in its ability to predict upper and lower bounds of the elastic characteristics; experimental data typically fit between the bounds. On the other hand, mechanistic hypotheses in the foundation of OAM are very simplistic and highly idealized. For many practical textile architectures they may not be adequate to actual fiber architectures and micromechanics mechanisms. Besides, OAM is not capable for accounting realistic details of the yarn geometry (i.e., continuously varying curvature of its centerline, actual cross-sectional shape and its variation), as well as yarn interactions at the crossover points in dry preforms and composites. Also, it is not possible to estimate a priori how accurate results provided by OAM will be. As our practical experience shows, the accuracy of effective elastic property predictions by OAM significantly depends on specific fabric architecture, elastic properties of fiber and matrix, and partial fiber volume fraction in each reinforcement direction.

Modified Matrix Method

Another approach which can be used for elastic property predictions of textile composites is the Modified Matrix Method (MMM). This approach has also been originated at the Institute of Polymer Mechanics in early 1970s and originally published in [55]. Later generalizations were presented in reference book [31]. Some authors associate this method with the OAM, however the two methods have very different theoretical backgrounds. MMM involves very specific micromechanics into the derivation of effective property equations. In fact, the MMM version presented in [55] is, essentially, the generalization of the earlier analysis approach [56] (also developed at the Institute of Polymer Mechanics), which considered composites with two-directional orthogonal planar reinforcement. To its disadvantage, MMM is very limited; it can only be applied to composites reinforced in three orthogonal directions (fortunately, 3-D orthogonal woven composites belong to this category). Note that original equations given in [55] contain some minor inconsistencies in the hypotheses and typo errors; the revised equations with corrections can be found in [15] and [41]. In these works the revised versions of MMM were applied to some glass fiber and carbon fiber 3-D orthogonal woven composites and showed very good agreement with experimental data, particularly for shear moduli and Poisson's ratios, which were predicted less accurately with OAM. Though MMM predictions may be more accurate than the OAM ones for specific 3-D orthogonal weave composites, severe limitations embedded in MMM make its range of applicability very narrow. Besides, there are probably only few available computer codes realizing MMM.

Probabilistic/stochastic analysis

It is a common belief that fiber waviness and misalignment are the two major technological reasons of commonly observed discrepancies between theoretical and experimental data for elastic properties of textile composites. Experimentally observed waviness and misalignment of warp, fill and through thickness yarns of 3-D interlock weave composites have been discussed and analyzed in [35, 57, 58] and other publications. Such waviness may be caused by a variety of manufacturing artifacts imparted during fabric formation, handling, placement in the mold or vacuum bag, resin flow, shrinkage and warpage during curing and cooling. A simple analytical approach developed in [35] allows one to estimate the effect of warp (called ''stuffers'') and fill (called ''fillers'') tow waviness on elastic properties of 3-D interlock weave composites. Monte-Carlo method was applied in [36, 37] to 3-D interlock weave composites in conjunction with the finite element ''Binary Model'', which is discussed in the next section. Application of Monte-Carlo simulations has also been demonstrated in [57].

A general analytical approach, which can be viewed as the probabilistic extension of the classical OAM, was developed in [59]; the approach is based on the theory of random functions. The theory has been used for the derivation of probabilistic characteristics of random tow paths in some generic fabric that may have any number of reinforcement directions in three-dimensional space. This approach has been applied in [41, 47, 59] to various specific types of textile composites, including 3-D woven ones. The advantage of this approach is its ability to solve practically any textile architecture with very little computational time and expense. Generating numerical results by a computer code implementing this approach requires 3-4 orders of magnitude less computational time than Monte-Carlo simulations, with essentially the same results. Actually, in this analytical approach only one analysis run (‘‘trial’’) is required, while Monte-Carlo simulation requires to conduct at least hundreds, more commonly thousands, tens and hundreds of thousands ‘‘trials’’ in order to obtain statistically meaningful distribution functions for elastic characteristics. For example, 100,000 trials were carried out in [57] for generating each probability distribution. While such a number of Monte-Carlo simulations is feasible for simple problems, in practical finite element analysis cases of complex structures even tens or hundreds of trials may take too long time and be prohibitively expensive.

Binary Model

Another original, rather generic and extensively demonstrated in publications approach, aimed primarily at failure modeling in various types of textile composites, is called ‘‘Binary Model’’. The Binary Model is, essentially, a special type of 3-D finite element analysis. This approach was first introduced in [36] and applied to 3-D interlock weave composites in [37]. As suggested in [36], the goal of this approach was to provide ‘‘the simplest possible formulation of such computational model which emphasis is placed on realistic representation of the pattern of reinforcing tows, random irregularity of tow positioning, randomness of the strength of constituent elements, and the mechanics of stress redistribution around sites of local failure’’. As one could have expected, in order to accomplish the above stated very ambitious goal, certain compromises have to be accepted. The most principal of them becomes obvious when dwelling a little bit into the model formulation. While resin-impregnated yarns, each containing thousands and tens of thousands of fibers, form the reinforcement of textile composite, in the Binary Model all of the yarns are treated as bodiless, one-dimensional ‘‘line elements’’. Such model assumption seems, without further insight, a very strange idea, because in reality reinforcing yarns may occupy 50%, 60%, even 70% of the total composite volume, while they are assigned zero volume in the model. However, if we forget for a while about Real Materials and Physics associated with them and think of this model assumption in the framework of Solid Mechanics, it does not look strange anymore and becomes quite appealing.

Indeed, Solid Mechanics (which is, essentially, a mathematical science) is full of contradictions between Geometry and Physics: finite volume of some material is reduced to a point; its elongations and distortions are converted into six mathematical strain components assigned to that point; surface tractions acting on the volume are converted into six mathematical stress components applied to the point; failure of that material volume (which is, of course, a complex physical phenomenon) is commonly expressed through mathematically constructed ‘‘phenomenological failure criteria’’ which relate, in one or more equations, the aforementioned mathematical strains or stresses on one side and some ‘‘ultimate material characteristics’’ on the other. The latter ones have to be obtained from mechanical tests by loading macroscopic material specimens. Obviously, equalizing mathematical strains and stresses (determined at the point) in one side of equation with macroscopically measured characteristics (expressed through elongations and forces at the instant when specimen fails in the grips of testing machine) in the other side of the same equation is not a trivial task. This explains why it is so difficult to accurately predict ‘‘strength’’, and especially strength of complex textile composites. But, that is what Solid Mechanics of composite basically does.

Now, returning to the Binary Model and evaluating it in the framework of Solid Mechanics, we can accept the assumption that reinforcement of textile composites is geometrically manifested by centerlines of the reinforcing yarns which are modeled in terms of one-dimensional (1-D) finite elements. Next question is: how do the model takes account of all mechanical properties carried out by the reinforcement? And this is done in Binary Model very elegantly: each resin-impregnated yarn retains only longitudinal properties, which are associated with the bodiless centerline and its respective 1-D finite elements. The rest of mechanical properties are delegated to the bulk of homogeneous anisotropic 3-D medium via special variational formulation of the respective 3-D finite element. As the result, textile composite is modeled as a set of infinitely thin elastic or inelastic curved ‘‘strings’’ embedded in 3-D medium; effective anisotropic properties of the medium include transverse properties of all individual resin-impregnated yarns and all properties of matrix material. The 3-D effective medium elements and the 1-D impregnated yarn elements are coupled at the mutual nodes. Important feature of this model is that none of line elements representing two distinct impregnated yarns interact directly; they can only influence each other through effective medium elements.

The argument made by Binary Model developers that the tows are mainly carrying longitudinal tensile and compressive loads, thus its transverse properties are secondary, can be accepted. However, it still looks like significant shortcoming of this model that there is no transfer, in the sense of the same Solid Mechanics, of shear and transverse normal tractions between the resin impregnated yarn and matrix, or between different resin impregnated yarns. In order to make some improvements of the model from this point of view, different kind of ''springs'' were additionally incorporated in the Binary Model. As suggested in [36], ''coupling springs'' could be used between the nodes of broken tows and the nodes of effective medium in progressive failure modeling. More springs were introduced for coupling ''warp weavers'' (through thickness tows) with the fill tows around which the warp weaver wraps. Of course, any kind of ''springs'' are foreign elements in the Solid Mechanics analysis development, thus their involvement deduces the elegancy and consistency of the Binary Model. Also worth noting that the model contains certain parameters which cannot be specified a priori and require ''calibration'' of the model against experimental data. Such calibration was demonstrated for the case of 3-D interlock weave composites in [37] with the use of experimental data from [35].

Being a little critical in the previous paragraph, we have to admit yet that there are several important advantages provided by the Binary Model in comparison with the other known analysis tools. Particularly, the size of computational problems, when analyzing complex textile composites, is significantly reduced in the Binary Model versus any direct 3-D finite element analysis approach, where yarns are treated as 3-D solids. Also, there are no singularity points or lines in this finite element formulation (see discussed in the next section). Another advantage is that Binary Model allows one to relatively easily incorporate non-linear properties into both the reinforcing tow and effective medium behavior. Further, the model showed capability to simulate various failure mechanisms experimentally observed in textile composites. Also importantly, the model enables for analyzing stochastic effects of tow misalignment via Monte-Carlo simulation, as demonstrated in [37].

''Meso-volume'' and ''3-D Mosaic'' concepts

Considering that textile composites have very complex hierarchical construction that leads to significant property variations at different levels, this author attempted since the early 1990's to develop a consistent, Solid Mechanics based multi-scale 3-D analysis methodology, that would enable to predict static and dynamic stress/strain fields, failure and fracture phenomena in various textile composites. The initial idea was to develop some unified analysis tool that would be applicable to any level of structural hierarchy. Particularly, the methodology has to allow one to perform analysis anywhere from the ''global'' analysis with totally smeared mechanical properties to the finest ''micro'' analysis at the level of individual fiber and matrix, or even at the level of individual fiber microstructure. As the result, two principal concepts have been introduced. The first is the concept of ''meso-volume'' [60], which is defined at some level of structural hierarchy as a homogeneous anisotropic material block having effective elastic properties. The second is the concept of 3-D Mosaic model [61], which represents composite structure at any hierarchical level as a Mosaic assemblage of an arbitrary number of distinct homogeneous anisotropic material blocks (meso-volumes) in the three coordinate directions. These two concepts have been incorporated in the 3-D variational analysis approach developed and implemented in [14, 15, 60–62]. The approach used special ''deficient'' spline functions of an arbitrary degree for displacement approximation in the three coordinate directions within 3-D Mosaic body.

Effective properties of each specific meso-volume can be predicted using more detailed build-up model of a composite at the next lower level of structural hierarchy. For example, if unidirectional composite is treated as a meso-volume, its effective elastic properties are predicted from elastic properties of individual fibers and matrix, fiber geometry and their arrangement in the composite. If the meso-volume representation is used for a unit cell a textile composite, its effective elastic properties are determined via elastic properties of resin-impregnated yarns (which are in this case treated as homogeneous unidirectional composites oriented in two, three, or more different directions), their geometry, spatial arrangement and, of course, on elastic properties of matrix material. Another important example is a laminated composite consisting of some number of layers with planar reinforcement but different fiber orientation within each layer. Each individual layer in this case is treated as distinct meso-volume having effective elastic properties of the respective unidirectional composite oriented at some angle with respect to the global coordinate axes associated with the laminate. Having effective properties of all individual layers, one can further determine effective properties of the whole laminate, which thus becomes the next level, ''global'' meso-volume. A practical composite structural part, which may consist of many dissimilar layers and contain joints, connections, stiffeners, patches and other features, can then be analyzed as 3-D Mosaic assembly of ‘‘global’’ meso-volumes, see for example analysis of laminated composite skin with integral 3-D braided composite stiffener in [61]. Other examples of this analysis applications to various textile composites can be found in [14, 15, 32, 33, 62–65]. The analysis approach also showed exceptional accuracy and efficiency when solving 3-D static elasticity problems of laminated composite plates, see [15, 60, 66–69, 71, 72] and thick cylindrical shells [15, 70]; see also summary of above works in [73].

The new version of variational 3-D Mosaic model approach presented in [74] utilizes Bernstein approximation polynomials of an arbitrary degree instead of ‘‘deficient’’ splines used for displacement approximations in the earlier version. This makes the mathematical formulations and computational algorithms much simpler, more open to various generalizations, and very close to conventional finite element analysis methodology. Actually, the approach can be identified as the hybrid *p-s*-type 3-D 8-noded hexahedral finite element on an arbitrary order. The element allows one to add degrees of freedom (d.o.f) either by increasing the power of basis functions, or by refining discretization mesh, or by doing both things simultaneously. There are several advantages of such element versus higher-order 3-D hexahedral elements based on Lagrange interpolation polynomials, as discussed in [74]; among its most important features are simplicity of analytical derivations, computational stability with increasing order of element, and higher convergence rate of strains and stresses.

In its current version, 3-D Mosaic analysis tool enables for accurate and computationally efficient predictions of 3-D displacement/strain/stress fields, initial and progressive failure, 2-D planar crack propagation in three orthogonal directions, and various type transient dynamic responses (specifically caused by blast and rigid body impact) of laminated, sandwich and different kind textile composite materials and structures. This has been demonstrated on various static, crack propagation and dynamic deformation problems in [18, 22, 23, 26, 73–78]. Importantly, this is inherently multi-scale approach, meaning that the output data provided by the analysis performed at a lower hierarchical level can be used as input data for the analysis at a higher hierarchical level, as originally demonstrated in [33].

Now, returning to the basic ‘‘Meso-volume’’ and ‘‘3-D Mosaic’’ concepts, the following four important aspects of this methodology will be briefly discussed in this section (they will be more thoroughly analyzed and illustrated in the rest of this paper): (a) determination of effective properties of meso-volumes; (b) division of the material/structural component into meso-volumes, (c) boundary conditions between adjacent meso-volumes, and (d) artificial mathematical singularities created by the ‘‘Meso-volume/3-D Mosaic’’ modeling approach.

Elastic property homogenization can be performed for each specific meso-volume type using various available analytical and numerical methods, particularly OAM, MMM, ‘‘sequential-parallel’’ analytical models discussed in Sections ‘‘Analytical models and first 3-D finite element analysis, Orientation Averaging Method, and Modified Matrix Method’’ above, and various numerical methods (finite element analysis specifically). Also, as shown in [18], 3-D Mosaic model itself is self-sufficient—it can be used for this purpose at different levels of structural hierarchy. What is needed for performing effective elastic property predictions using 3-D Mosaic approach is the involvement of special procedures for volumetric averaging of stress and strain fields, in conjunction with material stress–strain relations for each individual meso-volume.

Division of the analyzed composite material or its structure into meso-volumes may be categorized as (A) obvious and unique, or (B) intuitive and arbitrary. Some examples belonging to category (A) are: unidirectional composites with well-defined interfaces between fibers and matrix, laminates with well-defined interfaces between layers, sandwiches with well-defined interfaces between skins and core, stiffened structures with well-defined interfaces between skins and stiffeners, bonded joints with well-defined interfaces between adherends and adhesive. In practice, the requirement of ‘‘well-defined interface’’ may not be satisfied and, as was suggested in [60], some transitional ‘‘interphase’’ material can be added to the model. Its geometry and properties have to be determined from experimentally measured gradual property variation in the transition zone. This case falls between categories (A) and (B).

Fabric geometry modeling and voxel sorting

Further, when modeling textile composites it is possible, ideally, to distinguish between reinforcing yarns and matrix, then assign respective meso-volumes to the yarns and to the matrix, and construct 3-D Mosaic model. This is relatively simple task if the yarns are straight and orthogonal, a more complex task if the yarns are straight but non-orthogonal (due to meso-volumes of more complex shapes than parallelepipeds have to be used). The task becomes very complex if the yarns are curved, because mechanical properties of each curved yarn continuously change with respect to the global coordinate system. And further serious complication adds if the yarns change their cross-sectional shape and/or mutually penetrate (which always happens in the crossover regions). With all above complications taken into account, the goal to develop sufficiently general modeling and analysis tool for textile composites at the hierarchical level of individual yarns turns to be quite illusive.

What can be done in such challenging situation? The approach described in [14, 15, 62] and applied to several different textile composite systems in [14, 15, 32, 33, 61–63] offers one viable alternative to quantify and simplify actual yarn geometry and spatial architecture. First, textile composite element is divided, quite arbitrarily, into a number of meso-volumes; so, this approach obviously belongs to category (B) above. Then, the reinforcement geometry is modeled within each meso-volume, using information about the preform manufacturing method and composite processing technique. Different Processing Science Models can be used to relate manufacturing parameters to the reinforcement architecture in final composite product, resulting in 3-D geometric model identifying which part of the meso-volume is occupied by each reinforcing yarn, and which parts are occupied by matrix. The geometry representation is in a numerical (as well as graphical) form, to make it possible to quantify each yarn centerline path and local cross section. From this it is also possible to quantify twist and bending associated with the yarn at each point in space. The points corresponding to the swept cross-sections can be smoothed with a Beziér patch. The result can be presented as graphical rendering of selected fabric element.

If assumed, for simplicity, that the fabric element does not change during resin infusion and composite consolidation, the obtained graphical image can be used as the final reinforcement architecture in textile composite. The computation of effective mechanical properties of the meso-volumes from this geometric model is achieved by partitioning each meso-volume into sub-meso-volumes (called ‘‘voxels’’) and applying ‘‘voxel sorting’’ technique. Each voxel is tagged as either yarn voxel or matrix voxel. Voxels belonging to yarns made of different fiber materials (like in hybrid fiber preforms) are tagged differently. Also, each yarn voxel is tagged to its orientation.

As the result of applying voxel sorting technique (see further details in [14, 15]), one obtains total volume fraction of each fiber type within meso-volume and can further determine effective elastic properties of the meso-volume. Numerical examples illustrating application of this method to plain weave composites can be found in [14, 15, 62, 63, 65]. Same approach has been used for predicting effective elastic properties of 3-D interlock weave composites in [15, 32, 33, 62], 2-D triaxial braid composites in [15, 63], and 3-D braid composite in [61]. In work [46] of other authors, who were not aware of the aforementioned earlier publications, analogous voxel sorting technique was used for computing effective elastic properties of 3-D orthogonally reinforced composite Unit Cell.

From general perspective, voxel sorting technique in a combination with OAM is, probably, the simplest method of predicting effective elastic properties of some generic homogenized volumetric element of complex textile composite. Irrelevantly to particular numerical analysis method applied, the predicted effective elastic properties of all meso-volumes can serve as the necessary input data for the analysis. Specifically, each individual 3-D finite element in the mesh of elements generated for 3-D analysis of some composite structure can be called a meso-volume. Accordingly, its distinct set of elastic characteristics can be determined using methods discussed above.

3-D Mosaic structures and internal continuity conditions

After the division of composite structure into meso-volumes and the subsequent computation of effective elastic properties of all meso-volumes has been performed, one can compose the respective 3-D Mosaic model of the structure, which would possibly include step-wise variations of elastic properties along one, two, or three coordinates. Generic Mosaic parallelepiped introduced in [74] and shown in Fig. 1 can be used as the model applicable to many specific materials and structural components. Each individual brick in the parallelepiped may have its distinct anisotropic elastic properties. As one particular example, step-wise variation of elastic properties in only one (through thickness) direction obviously corresponds to the cases of flat laminated or sandwich plates. The other particular example is unidirectional composites where there are step-wise variations of certain elastic characteristics in two directions transverse to the fiber axis.

More complex examples, where there are step-wise variations of elastic characteristics in all three coordinates, are less obvious. Probably, the simplest of them is two orthogonal dissimilar material fibers in contact with each other and with surrounding dissimilar matrix,

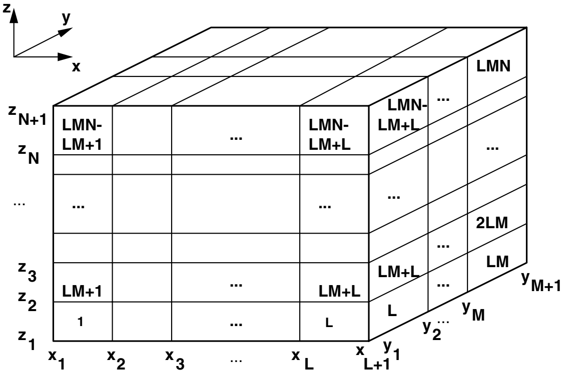

Fig. 1 Generic 3-D Mosaic model of a composite material/structure [74]

as illustrated in Fig. 2a. In this case there is a step-wise *z*-axis property variation between the fibers, and step-wise property variations in *x*- and *y*-axes between each fiber and matrix. A more complex example is shown in Fig. 2b, where there are three orthogonal dissimilar material fibers in contact, surrounded by matrix. These two material assemblies represent specific cases of 3-D Mosaic structure, and they can be modeled in terms of generic Mosaic parallelepiped of Fig. 1.

If the type models of Fig. 2 are further elaborated, they would lead to the structural models of many practical composites reinforced with 2-D weave, 2-D triaxial braid, 3-D weave, and 3-D braid illustrated in Fig. 3. Now we come to a fundamental understanding that, if performing 3-D analysis of any type textile composite, containing reinforcement in two or more directions, in terms of 3-D meso-volumes, there will be inevitable discontinuities of elastic properties in all three coordinates.

A very similar situation is faced when performing 3-D analysis of non-uniform textile composite which is divided into meso-volumes (or finite elements) having distinct elastic properties, following the methodology described above. This effect has been recognized in the earlier 3-D analysis studies, where 3-D brick-type Mosaic model was applied to various textile composites, see [14, 15, 32, 33, 61–64]. In this case the jumps of elastic properties between adjacent meso-volumes (or discrete elements) may be created artificially, but they become a reality in the computational model. Similarly, to our case, their presence may be hidden in the depth of some 3-D finite element analysis routines (like extrapolation and averaging of material input data and smoothing stress/strain output results), and not even realized by the user. Yet, being aware of their presence and understanding their possible effects on the output stress/strain fields, failure characteristics, etc. (rather than taking the commercial finite element code as ‘‘black box’’) may be helpful when evaluating and interpreting numerical results.

One specific problem is that having elastic property discontinuities within analyzed structure makes it very difficult to exactly satisfy all of the necessary internal continuity conditions. This issue has been discussed in detail in [60, 61] with some illustrative examples and practical suggestions. Indeed, when analyzing homogeneous material with discretization into 3-D elements, it is sufficient to satisfy continuity of all displacements and their first derivatives between the elements everywhere within the structure, thus assuring continuity of all strain and stress components. Contrary to that, when analyzing, for example, a laminate, adding continuity of first derivatives of all displacements within the structure to continuity of displacements, would result in a totally wrong solution. Obviously, the achieved continuity of all strain components at the interfaces between dissimilar materials would be in contradiction with the required continuity of transverse stresses. Therefore, strain continuity can be imposed

Fig. 2 Examples of simple 3-D Mosaic models with step-wise material property variations in three coordinate directions

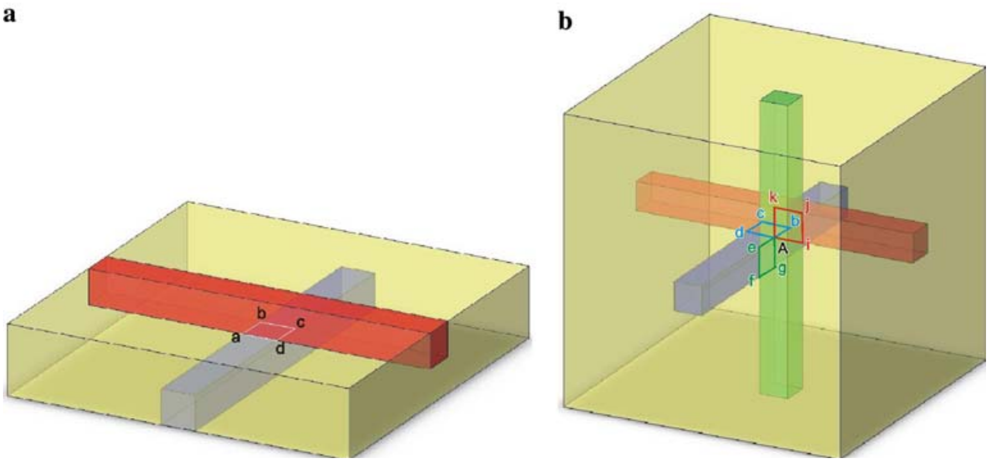

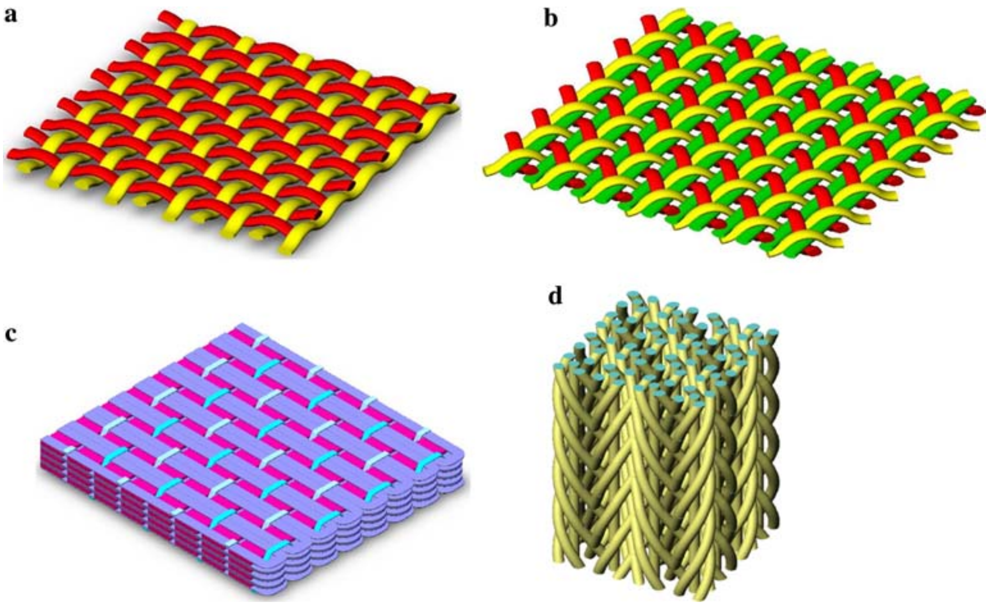

Fig. 3 Models of 2-D woven (**a**), 2-D triaxial braided (**b**), 3-D woven (**c**) and 3-D braided (**d**) fabric preforms for composites

anywhere within the structure with exception of all interfaces. Same is valid in a general case of 3-D Mosaic structure, where interfaces can be oriented in different directions.

It may seem unrealistic to impose selective strain continuity, however 3-D Mosaic analysis approach with the use of Bernstein polynomials developed in [74] allowed us to elegantly solve this task. Yet it should be understood that imposing continuity of displacements and selective continuity of strains within the structure having step-wise variations of elastic properties does not automatically provide continuous transverse stresses at the interfaces between dissimilar materials. Without using extremely cumbersome and limited in applications ‘‘mixed’’ variational formulations (see reviews of this type finite element analysis approaches in [15, 60, 66]), the transverse stress continuity can be satisfied only approximately, with their jumps at the interfaces controlled by the computational mesh refinement and/or increase of the polynomial degree. As illustrated by numerical examples in [15, 60, 66, 71–75], the jumps can be reduced to any desired level though will never become exactly zero.

3-D stress singularities

Another serious challenge of 3-D analysis in the presence of internal discontinuities of elastic properties is possible stress singularities. The general principle of solid mechanics, which can be used to identify possible sites of stress singularity is, that it can take place at any point or line where junction of three or more dissimilar materials, or junction of two or more dissimilar materials and ‘‘air’’ takes place. The well-known examples of this kind: free edge of composite laminate (singularities may take place at the lines on free surface between two dissimilar layers), hole or opening in composite laminate (as above, singularities at the lines on free surface between two dissimilar layers), bonded joints (singularities at the corner lines between adherend and adhesive, or between two dissimilar adherends if thickness of adhesive layer is neglected), stiffened panels (singularities at the corner lines between dissimilar skin and stiffener), bolted joints (singularities at the contour lines among two dissimilar joined materials and the bolt).

Now, looking back at simple models of Fig. 2, one can easily recognize that there are several lines, where three dissimilar materials come in contact. Specifically, in Fig. 2a those are: ab, bc, cd, and da, where two distinct fibers and matrix are in contact. And in Fig. 2b those lines are: Ab, bc, cd, dA, Ae, ef, fg, gA, Ai, ij, jk, and kA, where also two distinct fibers and matrix are in contact. In the latter model, point ‘‘A’’ is of particular interest, because four distinct materials (three orthogonal fibers and matrix) are in contact there. If one could perform a rigorous singularity analysis for this model, the results would likely show that point ‘‘A’’ corresponds to the highest order of singularity and, accordingly, it should be treated as the point of most probable initial failure of this composite. Unfortunately, there are no analytical tools which would be applicable to such 3-D elasticity problem, contrary to the case of 2-D elasticity, where theory of complex variables can be, and has been successfully applied to the stress singularity analysis.

Obviously, possible stress singularity lines and points add another substantial complication to 3-D solid mechanics analysis of textile composites. First, those lines and points of singularity give sharp rise to strains and stresses in respective sites of textile composite, which may be difficult to capture with lower order finite elements and/or coarse element meshes. Secondly, stress/strain convergence can not be achieved with the use of "regular" elements. One may try using special "singular" finite elements (which exist), but the order of singularity has to be assigned to the element a priori; thus, another empirical parameter would be involved in the analysis. Thirdly, it would be impossible to perform initial or progressive failure analysis using phenomenological failure criteria, because "initial failure load" will be infinitesimal, in accordance with the stresses being infinite.

Is it worth chasing such stress singularities in 3-D elasticity analysis of textile composites for any practical purpose? How to reasonably avoid or defeat them? How to predict failure of textile composite using different analysis approaches and computational tools reviewed above? Does the multi-level hierarchical analysis help to avoid stress singularities? Some of these issues will be discussed later in the paper when analyzing numerical results obtained for one specific 3-D woven composite Unit Cell.

Concluding remarks

In conclusion of the presented outlook at the history and state-of-the-art in the area of modeling and analysis of textile composites and, specifically, 3-D woven fabric composites, it has to be first emphasized that any structural analysis problem for this class of composite materials is very complex. No existing material model and analysis tool can overcome all of the difficulties and answer all of the questions. Especially when it is required to predict progressive damage and failure, ultimate failure loads, response to multi-axial loading, sensitivity to stress raisers, impact and ballistic resistance, probabilistic and stochastic effects caused by random misalignment, waviness of the reinforcement, and other manufacturing artifacts. OAM and MMM are only applicable to predicting effective elastic properties, besides the latter one can rigorously be used only for orthogonally reinforced composites. Various type 3-D finite element analysis tools are, of course, much more capable, however simply using some 3-D finite element from available commercial package, even with a seemingly fine mesh, does not guarantee adequacy and accuracy of numerical results. Of course, usually hidden extrapolation and averaging of input data and smoothing output stress/strain fields between the elements can make an impression that there are no difficulties or concerns whatsoever. Yet, results provided by analysis may fail the comparison with experimental data, which is the only true validation criterion. Particularly, finite element predictions of failure, damage and fracture with the use of algorithms that involve extrapolations and smoothing of input and/or output data should be always taken with certain suspicion.

In any case, it is highly advisable to validate any numerical results obtained with generic commercial finite element codes by experimental data and/or by benchmark theoretical results provided by analysis tools specialized for textile composites. It is believed that 3-D Mosaic and Binary Model tools are the primary candidates to be used for generating such benchmark data, due to all important aspects of material models and computational algorithms in those tools are transparent, can be thoroughly understood and evaluated. Unfortunately, the amount of published experimental data, especially for 3-D textile composites, is very limited.

This paper further describes essential aspects of 3-D Mosaic model and variational analysis approach, including 3-D stress/strain analysis, volumetric averaging of stress/strain fields, computation of effective elastic characteristics, and 3-D progressive failure analysis that considers nine principal failure modes and utilizes ultimate strain criteria.

Theoretical background of present 3-D Mosaic approach

Generic Mosaic parallelepiped and its discretization

Paper [74] provides all mathematical details of 3-D variational analysis approach associated with generic Mosaic parallelepiped of Fig. 1. As explained in Section "Meso-volume" and "3-D Mosaic" concepts", such parallelepiped can be composed of an arbitrary number of homogeneous material bricks (meso-volumes) in x, y and z directions; total number of material bricks is $L \cdot M \cdot N$. Each of the bricks may have its distinct mechanical properties characterized by 21 independent elastic constants in the case of general anisotropy, 13 constants in the case of monoclinic symmetry, 9 constants in the case of orthotropic symmetry, 5 constants in the case of monotropic (transversely isotropic) symmetry, and 2 constants in the case of isotropic material. All equations used in the analysis automatically apply to any specific case of anisotropy. This feature allows including in the unified model such materials as polymer matrices, adhesives, isotropic or anisotropic fibers, unidirectional composites, 2-D fabric composites, 3-D fabric composites, as well as metals, wood, concrete, homogenized cores, and other traditional and non-traditional structural materials.

The representation of given composite material or structure in terms of this generic Mosaic parallelepiped is the first necessary step of analysis. Each material contained in composite structure of interest, and its location within the structure, have to be put in correspondence with one or more bricks in the Mosaic parallelepiped. Of course, generic model of Fig. 1 includes numerous particular cases. Specifically, 3-D Mosaic model of a laminated plate can be readily obtained by assuming that all material bricks in each ‘‘Z-layer’’ have identical properties (i.e., material properties are independent of the in-plane coordinates x and y), while those properties change from one Z-layer to the other in a step-wise manner. Further, in accordance with original 3-D Mosaic model [61] some of the bricks may be ‘‘dummy’’, meaning that they fill empty spaces when developing Mosaic parallelepiped model of some structural part. The following are examples of some previously studied problems, where addition of dummy material bricks was necessary: plates with parallel or orthogonal sets of stiffeners [61], double box-beam spar [65], various configurations of adhesive lap joints [75–77], and composite patch repair of metal or composite panel [78]. Of course, elastic characteristics assigned to each dummy material brick have to be carefully selected (relative to elastic properties of all other materials incorporated), in order to make any effect of dummy material bricks on the stress/strain fields negligible. Typically, isotropic dummy bricks with Young's modulus 3–4 orders of magnitude lower than the lowest modulus among all ‘‘physical’’ bricks would satisfy this condition. Such lowest modulus may be Young's modulus of polymer matrix or adhesive, transverse modulus of unidirectional composite, the lowest effective modulus of core material, etc.

Next step of discretization used in 3-D Mosaic model is not directly related to material properties of the bricks, and its purpose is to establish computational mesh of discrete elements that would provide sufficient accuracy of numerical solution. In this step, each interval $(x_\xi, x_{\xi+1}), (y_\eta, y_{\eta+1}), (z_\zeta, z_{\zeta+1})$, where $\xi = 1, 2, \ldots, L$; $\eta = 1, 2, \ldots, M$; $\zeta = 1, 2, \ldots, N$ in accordance with Fig. 1, is divided (uniformly or non-uniformly) into some number of subintervals. It has to be mentioned that selected mesh in x direction applies to all y-directional and z-directional ‘‘layers’’. Analogously, selected mesh in y direction applies to all x-directional and z-directional ‘‘layers’’, and selected mesh in z direction applies to all x-directional and y-directional ‘‘layers’’. In the result, Mosaic parallelepiped of Fig. 1 is represented as an assemblage of a greater number of smaller parallelepipeds; their total number can vary from $L \cdot M \cdot N$ (when ‘‘computational mesh’’ coincides with ‘‘material mesh’’) to any higher number, depending on the computational mesh density. A through notation of coordinates corresponding to subinterval ends, x_l, y_m, z_n is now introduced, while the coordinates corresponding to the interval ends are noted x_ξ, y_η, z_ζ. In other words, sets of integers $\{\xi\}, \{\eta\}$ and $\{\zeta\}$ (those play special role in the analysis, as will be explained in Section ‘‘Displacement and strain continuity conditions’’) form subsets of the respective sets of integers $\{l\}$, $\{m\}$ and $\{n\}$. Now we visualize in Fig. 4 the basic computational discrete element.

3-D displacement approximation

A 3-D displacement field in the qth discrete element is represented in terms of the following triple series (analogously to [60, 61, 74]):

$$u_\alpha^{(q)}(x, y, z) = \sum_{i=0}^{I} \sum_{j=0}^{J} \sum_{k=0}^{K} U_{ijk}^{\alpha(q)} X_i(x) Y_j(y) Z_k(z) \tag{1}$$

Here α =1, 2, 3; integers I, J and K define number of d.o.f.; $U_{ijk}^{\alpha(q)}$ are undetermined coefficients; $X_i(x)$, $Y_j(y)$ and $Z_k(z)$ are three sets of basis functions, which can be, generally, any appropriate sets of polynomials. Total potential energy function of the qth discrete element $U^{(q)}$ can be then written as follows:

$$U^{(q)} = W^{(q)} - P^{(q)} \tag{2}$$

where $W^{(q)}$ is the work of external surface tractions acting on the element, and $P^{(q)}$ is its total strain energy. These energy components have been derived in the following explicit form [74]:

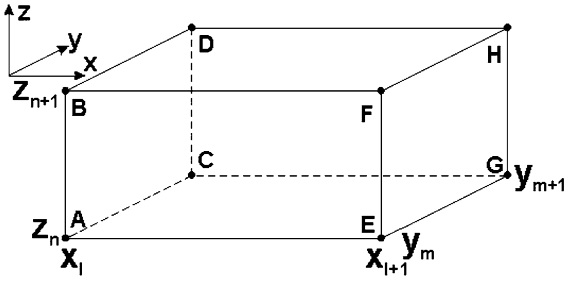

Fig. 4 The basic discrete element used in 3-D Mosaic model approach

$$P^{(q)} = \frac{1}{2}\sum_{i=0}^{I}\sum_{j=0}^{J}\sum_{k=0}^{K}\sum_{p=0}^{I}\sum_{q=0}^{J}\sum_{r=0}^{K}\sum_{\alpha=1}^{3}\sum_{\beta=1}^{3} U_{ijk}^{\beta(q)} a_{ijk,pqr}^{\alpha\beta(q)} U_{pqr}^{\alpha(q)} = \frac{1}{2}\mathbf{U}^{(q)\mathrm{T}}\mathbf{A}^{(q)}\mathbf{U}^{(q)} \tag{3}$$

$$W^{(q)} = \sum_{i=0}^{I}\sum_{j=0}^{J}\sum_{k=0}^{K}\sum_{\alpha=1}^{3} U_{ijk}^{\alpha(q)} Q_{ijk}^{\alpha(q)} = \mathbf{U}^{(q)\mathrm{T}}\mathbf{Q}^{(q)} \tag{4}$$

Here, $\mathbf{U}^{(q)}$ is vector of undetermined displacement coefficients, $\mathbf{A}^{(q)}$ is "stiffness matrix", and $\mathbf{Q}^{(q)}$ is vector of external surface tractions; their explicit expressions can be found in [74]. After that the total potential energy of the whole Mosaic parallelepiped is written as the sum of all respective energies corresponding to individual discrete elements (Q is their total number):

$$U = W - P = \sum_{q=1}^{Q}\left[W^{(q)} - P^{(q)}\right] \tag{5}$$

To further proceed with algorithmic development, we need to specify the form of basis functions $X_i\,(x)$, $Y_j\,(y)$ and $Z_k\,(z)$ in (1). Following [74], the basis functions taken for the qth discrete element confined between three orthogonal sets of parallel planes x_l and x_{l+1}, y_m and y_{m+1}, z_n and z_{n+1} are assumed in the form of Bernstein approximation polynomials:

$$X_i(x) = \begin{cases} B_i^I(x) = \frac{I!}{i!(I-i)!}\left(\frac{x-x_l}{x_{l+1}-x_l}\right)^i\left(\frac{x_{l+1}-x}{x_{l+1}-x_l}\right)^{I-i} & \text{for } x \in [x_l, x_{l+1}] \\ 0 \text{ else} \end{cases} \tag{6}$$

$$Y_j(y) = \begin{cases} B_j^J(y) = \frac{J!}{j!(J-j)!}\left(\frac{y-y_m}{y_{m+1}-y_m}\right)^j\left(\frac{y_{m+1}-y}{y_{m+1}-y_m}\right)^{J-j} & \text{for } y \in [y_m, y_{m+1}] \\ 0 \text{ else} \end{cases} \tag{7}$$

$$Z_k(z) = \begin{cases} B_k^K(z) = \frac{K!}{k!(K-k)!}\left(\frac{z-z_n}{z_{n+1}-z_n}\right)^k\left(\frac{z_{n+1}-z}{z_{n+1}-z_n}\right)^{K-k} & \text{for } z \in [z_n, z_{n+1}] \\ 0 \text{ else} \end{cases} \tag{8}$$

Integers l, m and n define location of all boundaries between discrete elements.

Displacement and strain continuity conditions

Next steps in the algorithmic development are to modify the total potential energy expression (5) by imposing internal displacement continuity conditions and external kinematic boundary conditions. With the use of displacement representation (1) and basis functions (6)–(8), the "perfect bonding" condition, e.g., continuity of all three displacements between any two discrete elements in the Mosaic body can be expressed through the following set of relations [74]:

$$\begin{aligned} &U_{Ijk}^{\alpha,q(l,m,n)} = U_{0jk}^{\alpha,q(l+1,m,n)}; \quad U_{iJk}^{\alpha,q(l,m,n)} = U_{i0k}^{\alpha,q(l,m+1,n)}; \\ &U_{ijK}^{\alpha,q(l,m,n)} = U_{ij0}^{\alpha,q(l,m,n+1)} \end{aligned} \tag{9}$$

External kinematic boundary conditions should be stated for each specific boundary value problem and imposed accordingly. Further details of the energy modification by incorporating internal kinematic boundary conditions (9) and some types of external kinematic boundary conditions can be found in [74].

It should be noted that imposing displacement continuity conditions (9) only does not ensure that the computed strains and stresses will be continuous within a homogeneous material brick (meso-volume). Additional analytical relations shall be included to satisfy this requirement. As shown in [74], the following equations ensure that all strain and stress components are continuous within all homogeneous material bricks in the Mosaic parallelepiped of Fig. 1:

$$\begin{aligned} &U_{1jk}^{\alpha,q(\bar{l}+1,m,n)} = \frac{x_{\bar{l}+1} - x_{\bar{l}-1}}{x_{\bar{l}} - x_{\bar{l}-1}} U_{Ijk}^{\alpha,q(\bar{l},m,n)} - \frac{x_{\bar{l}+1} - x_{\bar{l}}}{x_{\bar{l}} - x_{\bar{l}-1}} U_{I-1jk}^{\alpha,q(\bar{l},m,n)}; \\ &j = 0,1,\ldots,J; \;\; k = 0,1,\ldots,K \end{aligned} \tag{10}$$

$$\begin{aligned} &U_{i1k}^{\alpha,q(l,\bar{m}+1,n)} = \frac{y_{\bar{m}+1} - y_{\bar{m}-1}}{y_{\bar{m}} - y_{\bar{m}-1}} U_{iJk}^{\alpha,q(l,\bar{m},n)} - \frac{y_{\bar{m}+1} - y_{\bar{m}}}{y_{\bar{m}} - y_{\bar{m}-1}} U_{iJ-1k}^{\alpha,q(l,\bar{m},n)}; \\ &i = 0,1,\ldots,I; \;\; k = 0,1,\ldots,K \end{aligned} \tag{11}$$

$$\begin{aligned} &U_{ij1}^{\alpha,q(l,m,\bar{n}+1)} = \frac{z_{\bar{n}+1} - z_{\bar{n}-1}}{z_{\bar{n}} - z_{\bar{n}-1}} U_{ijK}^{\alpha,q(l,m,\bar{n})} - \frac{z_{\bar{n}+1} - z_{\bar{n}}}{z_{\bar{n}} - z_{\bar{n}-1}} U_{ijK-1}^{\alpha,q(l,m,\bar{n})}; \\ &i = 0,1,\ldots,I; \;\; j = 0,1,\ldots,J \end{aligned} \tag{12}$$

Details of derivation and notations used in (10)–(12) can be found in [74]. The use of indices $\bar{l}, \bar{m}, \bar{n}$ in these equations instead of indices l, m, n used in Eq. 9 has principal meaning. This emphasizes, that Eqs. 10–12 should not be applied at the interfaces between dissimilar material bricks. In other words, sets of integers $\{\bar{l}\}, \{\bar{m}\}, \{\bar{n}\}$ are obtained from the respective sets of integers $\{l\}$, $\{m\}$, $\{n\}$ by elimination of the subsets $\{\xi\}, \{\eta\}, \{\zeta\}$. This feature of the developed analysis approach allows calling it a "*material-adaptive*" approach. Numerical example presented in [74] have illustrated that imposing Eqs. 10–12 in addition to Eq. 9 eliminated all jumps of computed strains and stresses within each homogeneous layer of a laminated plate and also significantly improved overall accuracy of the solution without increasing degree of basis functions or mesh density.

Crack propagation modeling

Another important feature of 3-D Mosaic analysis approach is that it enables to solve 3-D stress/strain problems in the presence of 2-D planar cracks between any two discrete elements in Mosaic parallelepiped of Fig. 1. Each individual crack is introduced by detaching two adjacent discrete elements. Planes of the cracks may be perpendicular to one of coordinate axes x, y or z. Dimensions of "elementary" cracks perpendicular to x, y and z-axis respectively, are $(y_{m+1} - y_m)\times(z_{n+1} - z_n), (x_{l+1} - x_l) \times (z_{n+1} - z_n)$, and $(x_{l+1} - x_l)\times(y_{m+1} - y_m)$ in accordance with notations in Fig. 4. From algorithmic viewpoint, detaching two adjacent bricks means that certain equations are eliminated from the full set of displacement continuity conditions (9). The cracks can be located either within a homogeneous material brick (meso-volume) or between two adjacent material bricks. Any number of cracks can be imposed. The discrete elements can be detached in one, two or three displacements simultaneously, by selectively eliminating continuity conditions for u_x, u_y, and/or u_z. This allows one to model Fracture Modes I, II and III.

Further, initial crack can be extended in one or two in-plane directions for the other neighboring discrete elements in the respective coordinate directions. Hence, by sequential analysis runs one can model (a) 2-D planar crack growing in its plane, (b) crack orientation change and further growth in one of the other two orthogonal planes, and (c) branching of a single crack into two or three cracks oriented in mutually orthogonal planes. These opportunities provided by the algorithm open the door to the crack growth analysis; this only requires adding an appropriate crack propagation criterion.

The crack propagation analysis approach has been developed and implemented in the framework of 3-D Mosaic model with the use of Critical Strain Energy Release Rate Criterion (CSERRC) in [75–77]. It appears that having all analytical tools described above, this is a relatively simple task. The strain energy of any discrete element can be evaluated from Eq. 3. Then, the total strain energy of entire Mosaic parallelepiped is expressed as $P = \sum_{q=1}^{Q} P^{(q)}$, where Q is total number of discrete elements in the Mosaic parallelepiped. This strain energy can be computed for the initial state with no crack, P_0, and for any number of subsequent states, each characterized by its total strain energy value: $P_1, P_2, \ldots$ Accordingly, the strain energy release between two consecutive states are expressed as $\Delta P_1 = P_0 - P_1, \Delta P_2 = P_1 - P_2, \ldots$ Simultaneously, the growth of crack area is characterized by increments $\Delta S_1, \Delta S_2, \ldots$ Then, the sought strain energy release rates are defined as

$$R_1 = \frac{\Delta P_1}{\Delta S_1}, \quad R_2 = \frac{\Delta P_2}{\Delta S_2}; \ \ldots, \quad R_r = \frac{\Delta P_r}{\Delta S_r}, \ \ldots \tag{13}$$

In each crack growth step the computed value R_r is compared with its respective CSERRC denoted R_r^{cr}. If $R_r \geq R_r^{cr}$ and the respective stress component(s) allow for crack opening in Modes I, II or III, the crack gets next increment at the load level applied. Contrary to that, if $R_\gamma < R_\gamma^{cr}$, the crack will not grow at the given load level. In the latter case the load can be increased, and analysis continued in the iterative manner. Following this algorithm, a propagation of any number of cracks can be considered simultaneously, with their possible growth paths in different planes having mutually orthogonal orientations.

Other computational procedures

After all dependent variables have been eliminated from the total potential energy function (5), as the result of imposing all or the part of displacement continuity conditions (9), strain continuity conditions (10)–(12), and external geometric boundary conditions, a Ritz-type procedure can be applied. This allows one to derive a system of linear simultaneous equations with respect to remaining undetermined coefficients $U_{ijk}^{\alpha,q}$. The system can be solved by applying standard computational routines, resulting in numerical values of all undetermined coefficients entering in the series (1). After that the 3-D displacement, strain and stress values at any point of Mosaic parallelepiped can be computed by summation of their respective triple series. Specifically, displacements are computed directly from series (1), strains are computed from the series obtained by substitution of (1) into strain–displacement relations of linear elasticity, and stresses are computed by substitution of strains into equations of generalized Hooke's law.

Summation of the respective triple series is performed numerically, point-wise; the displacements, strains and stresses can be computed for any combination of coordinates $\{x, y, z\}$ belonging to Mosaic parallelepiped. Special attention is paid to interfaces between dissimilar materials, where certain strain and stress components may be discontinuous. To show such discontinuities explicitly, those discontinuous strains and stresses have to be computed at two very close points within adjacent material bricks. Note that this analysis approach does not require extrapolations to Gaussian points, stress/strain averaging, or other usual finite element post processing procedures. Particularly remarkable, analytical expressions have been derived in [74] for all integrals of Bernstein basis functions and their derivatives involved in the equations defining stiffness matrix $\mathbf{A}^{(q)}$; thus, even numerical evaluation of those integrals is not used.

Relation to conventional 3-D hexahedral finite element

The above description of 3-D Mosaic variational analysis approach has probably made it obvious that its mathematical formulation has many similarities with 3-D hexahedral finite element. For example, if the first degree basis functions ($I=J=K=1$) are taken, see Fig. 5a, the basic discrete element of Fig. 4 is degenerated into conventional first order hexahedral finite element. However, when considering higher degree Bernstein basis functions defined by (6)–(8) and shown in Fig. 5b, c and d, the difference between them and other special polynomials used in applied mathematics and computation mechanics shows significant. Among those other we can mention Lagrange, Hermite, Bernoulli, Legendre, Laguerre, and Tschebyscheff polynomials (information on them can be found, for example, in [79]). Particularly, the principal difference between Bernstein and Lagrange polynomials is that the first ones are *approximation* polynomials, while the second ones are *interpolation* polynomials. This means that Bernstein polynomials of any degree do not oscillate between the interval ends, as seen in Fig. 5, while Lagrange polynomials have increasing number of internal nodes within the interval when degree of the polynomials grows. Accordingly, Bernstein basis functions always define an *8-noded element* (shown in Fig. 4), independently of the polynomial degree.

There are several important mathematical and computational advantages provided by Bernstein polynomials vs. other polynomial types:

(i) Bernstein polynomials of higher degree provide much better computational stability than their Lagrange counterparts (this is valid for all approximation vs. interpolation polynomials).

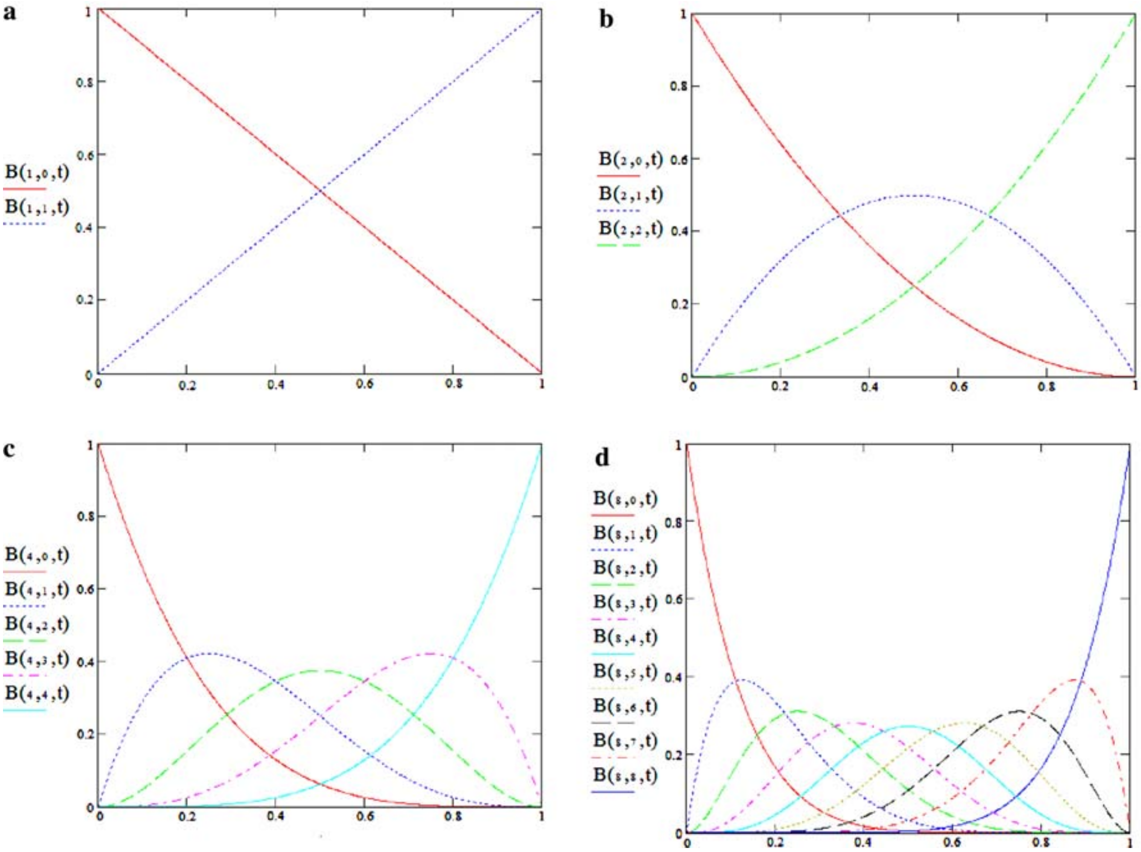

Fig. 5 Bernstein polynomials in [0, 1] interval for degrees 1 (**a**), 2 (**b**), 4 (**c**) and 8 (**d**)

(ii) Bernstein polynomials yield ‘‘smooth approximation’’, which means that if the approximated function is differentiable, then the convergence (with increasing polynomial degree) is ensured not only for approximated function, but also for its derivatives. This is a very important advantage versus other modes of approximation, like Tschebyscheff polynomials or best uniform approximation, see [79]. When applying this property to the problems of our interest, we can thus ensure that convergence of strains and stresses within homogeneous material bricks will be achieved by increasing degree of Bernstein basis functions.

(iii) External boundary condition of uniformly distributed displacement over some surface element can be imposed analytically and exactly satisfied in the analysis, see [74].

(iv) A relatively simple form of Bernstein polynomials (6)–(8) allowed this author to derive all of the necessary mathematical algorithms in closed analytical form [74].

(v) The described 3-D variational analysis approach with displacement representation in terms of triple series (1) and Bernstein basis functions (6)–(8) can be re-formulated in conventional terms of 3-D hexahedral finite element, see [74]. For that, the primary displacement approximation (1) can be first rewritten in the following equivalent form:

$$u_\alpha^{(q)}(x,y,z) = \sum_{f=1}^{F} U_f^{\alpha(q)} N_f(x,y,z); \quad \alpha = 1,2,3 \tag{14}$$

where

$$N_f(x,y,z) = N_{ijk}(x,y,z) = B_i^I(x) B_j^J(y) B_k^K(z) \tag{15}$$

$$f = f(i,j,k) = (k+1) + j(K+1) + i(J+1)(K+1) \tag{16}$$

$$F = (I+1)(J+1)(K+1) \tag{17}$$

It is easy to verify that Bernstein basis functions (6)–(8) provide the following properties to the ‘‘shape functions’’ (15):

$$\begin{aligned}
&N_1(x_l, y_m, z_n) = 1;\\
&N_{K+1}(x_l, y_m, z_{n+1}) = 1;\\
&N_{1+J(K+1)}(x_l, y_{m+1}, z_n) = 1;\\
&N_{(J+1)(K+1)}(x_l, y_{m+1}, z_{n+1}) = 1;\\
&N_{1+I(J+1)(K+1)}(x_{l+1}, y_m, z_n) = 1;\\
&N_{(K+1)[1+I(J+1)]}(x_{l+1}, y_m, z_{n+1}) = 1;\\
&N_{1+(K+1)[J+I(J+1)]}(x_{l+1}, y_{m+1}, z_n) = 1;\\
&N_{(I+1)(J+1)(K+1)}(x_{l+1}, y_{m+1}, z_{n+1}) = 1
\end{aligned} \tag{18}$$

For each of the above eight combinations of the coordinate triads in Eq. 18 (those combinations correspond to eight corners A, B, C, D, E, F, G and H of discrete element shown in Fig. 4), all shape functions N_f other than the ones listed in (18) take zero values. Therefore, Eqs. 14–18 supplemented by (6)–(8) define an arbitrary order hexahedral finite element, which is compatible with any other 3-D finite element methodology. At the same time, as was explained above, this element has its distinct features.

Volumetric averaging of stress/strain fields in 3-D Mosaic structures

The 3-D Mosaic model and computational approach described in Section ‘‘Theoretical background of present 3-D Mosaic approach’’ can be directly applied to predicting effective elastic properties of various type composite materials based on their 3-D micromechanics stress/strain analysis results. Considering again generic Mosaic parallelepiped shown in Fig. 1, we can conduct several ‘‘computational experiments’’ which will allow us to obtain nine independent effective elastic characteristics of homogenized orthotropic material. The algorithms applicable to more general cases of anisotropy can be developed analogously. We start here with deriving algorithm for the case of applied displacements (strains), then will address the case of applied surface tractions (stresses).

Effective elastic properties under applied strains

Consider the case of applied displacements, for which the respective ‘‘applied’’ strains can be calculated as applied displacement divided over the length of Mosaic parallelepiped in the corresponding loading direction. The following nine computational experiments can be conducted with some uniformly distributed displacement component at the loaded surface in each case (a, b and c are dimensions of Mosaic parallelepiped in x, y and z directions, respectively):

(i) Symmetric loading in x direction with applied displacement u_x^0 (normal strain $\varepsilon_x^0 = u_x^0/a$).

(ii) Symmetric loading in y direction with applied displacement u_y^0 (normal strain $\varepsilon_y^0 = u_y^0/b$).

(iii) Symmetric loading in z direction with applied displacement u_z^0 (normal strain $\varepsilon_z^0 = u_z^0/c$).

(iv) Uniformly distributed tangential displacement u_x^0 applied in opposite directions to the opposite sides of the parallelepiped perpendicular to axis y; the applied shear strain is $\varepsilon_{xy}^0 = 2u_x^0/b$.

(v) Same as in (iv) but for displacement u_y^0 applied to the sides which are perpendicular to axis x; the applied shear strain is $\varepsilon_{yx}^0 = 2u_y^0/a$.

(vi) Same as in (iv) but for displacement u_x^0 applied to the sides which are perpendicular to axis z; the applied shear strain is $\varepsilon_{xz}^0 = 2u_x^0/c$.

(vii) Same as in (iv) but for displacement u_z^0 applied to the sides which are perpendicular to axis x; the applied shear strain is $\varepsilon_{zx}^0 = 2u_z^0/a$.

(viii) Same as in (iv) but for displacement u_y^0 applied to the sides which are perpendicular to axis z; the applied shear strain is $\varepsilon_{yz}^0 = 2u_z^0/c$.

(ix) Same as in (iv) but for displacement u_z^0 applied to the sides which are perpendicular to axis y; the applied shear strain is $\varepsilon_{yz}^0 = 2u_z^0/b$.

In the case of orthotropic materials, the normal stress/strain components are separated from the shear ones. Accordingly, the group of computational experiments (i)–(iii) is independent from the group (iv)–(ix). Moreover, due to each pair of shear stress/strain components is not related to the other two pairs, the three groups of two computational experiments (iv), (v); (vi), (vii); and (viii), (ix) are independent. Also, within each of these three groups, the pairs of computational experiments (iv) and (v), (vi) and (vii), (viii) and (ix) shall, theoretically, provide identical results for effective shear moduli. However, due to various possible computational inaccuracies this may not be achieved. In such situation it is advisable to compute all six effective shear moduli from respective six computational experiments, then compare results, and calculate mean values for each of the three pairs; the resulting three values have to be taken as effective shear moduli.

The nine values of applied strains are known from the imposed boundary conditions described above. Then, by using 3-D Mosaic analysis approach, the remaining stress/strain components are computed in each case. After that, computational averaging of those stress/strain components is performed in all three coordinates throughout 3-D Mosaic parallelepiped. The density of rendering points can be methodically increased until it does not affect the averaging results. This procedure yields the following averaged strain and stress components:

In case (i): $\left\langle \varepsilon_y^x \right\rangle, \langle \varepsilon_z^x \rangle, \langle \sigma_x^x \rangle, \left\langle \sigma_y^x \right\rangle, \langle \sigma_z^x \rangle$

In case (ii): $\langle \varepsilon_x^y \rangle, \langle \varepsilon_z^y \rangle, \langle \sigma_x^y \rangle, \left\langle \sigma_y^y \right\rangle, \langle \sigma_z^y \rangle$

In case (iii): $\langle \varepsilon_x^z \rangle, \left\langle \varepsilon_y^z \right\rangle, \langle \sigma_x^z \rangle, \left\langle \sigma_y^z \right\rangle, \langle \sigma_z^z \rangle$

In case (iv): $\langle \sigma_{xy} \rangle$

In case (v): $\langle \sigma_{yx} \rangle$

In case (vi): $\langle \sigma_{xz} \rangle$

In case (vii): $\langle \sigma_{zx} \rangle$

In case (viii): $\langle \sigma_{yz} \rangle$

In case (ix): $\langle \sigma_{zy} \rangle$

In above normal strains and stresses the superscript indicates ‘‘loading’’ direction, while the subscript indicates direction of ‘‘measured response’’. In above shear stresses first subscript corresponds to the loading direction while the second to the measured response direction.

The applied and the computed averaged normal strains and stresses are related through Hooke's law for orthotropic material written below in the following matrix form:

$$\widehat{\mathbf{E}} \cdot \vec{\mathbf{C}} = \vec{\mathbf{S}} \tag{19}$$

where stress vector $\vec{\mathbf{S}}$, strain matrix $\widehat{\mathbf{E}}$, and vector of unknown effective material stiffness components $\vec{\mathbf{C}}$ are defined as following

$$\vec{\mathbf{S}} = \begin{bmatrix} \langle \sigma_x^x \rangle \\ \langle \sigma_y^x \rangle \\ \langle \sigma_z^x \rangle \\ \langle \sigma_x^y \rangle \\ \langle \sigma_y^y \rangle \\ \langle \sigma_z^y \rangle \\ \langle \sigma_x^z \rangle \\ \langle \sigma_y^z \rangle \\ \langle \sigma_z^z \rangle \end{bmatrix}; \quad \widehat{\mathbf{E}} = \begin{bmatrix} \varepsilon_x^0 & \langle \varepsilon_y^x \rangle & \langle \varepsilon_z^x \rangle & 0 & 0 & 0 & 0 & 0 & 0 \\ 0 & 0 & 0 & \varepsilon_x^0 & \langle \varepsilon_y^x \rangle & \langle \varepsilon_z^x \rangle & 0 & 0 & 0 \\ 0 & 0 & 0 & 0 & 0 & 0 & \varepsilon_x^0 & \langle \varepsilon_y^x \rangle & \langle \varepsilon_z^x \rangle \\ \langle \varepsilon_x^y \rangle & \varepsilon_y^0 & \langle \varepsilon_z^y \rangle & 0 & 0 & 0 & 0 & 0 & 0 \\ 0 & 0 & 0 & \langle \varepsilon_x^y \rangle & \varepsilon_y^0 & \langle \varepsilon_z^y \rangle & 0 & 0 & 0 \\ 0 & 0 & 0 & 0 & 0 & 0 & \langle \varepsilon_x^y \rangle & \varepsilon_y^0 & \langle \varepsilon_z^y \rangle \\ \langle \varepsilon_x^z \rangle & \langle \varepsilon_y^z \rangle & \varepsilon_z^0 & 0 & 0 & 0 & 0 & 0 & 0 \\ 0 & 0 & 0 & \langle \varepsilon_x^z \rangle & \langle \varepsilon_y^z \rangle & \varepsilon_z^0 & 0 & 0 & 0 \\ 0 & 0 & 0 & 0 & 0 & 0 & \langle \varepsilon_x^z \rangle & \langle \varepsilon_y^z \rangle & \varepsilon_z^0 \end{bmatrix}; \quad \vec{\mathbf{C}} = \begin{bmatrix} \langle C_{11} \rangle \\ \langle C_{12} \rangle \\ \langle C_{13} \rangle \\ \langle C_{21} \rangle \\ \langle C_{22} \rangle \\ \langle C_{23} \rangle \\ \langle C_{31} \rangle \\ \langle C_{32} \rangle \\ \langle C_{33} \rangle \end{bmatrix} \tag{20}$$

After multiplying Eq. 19 by inverse matrix $\hat{\mathbf{E}}^{-1}$ it is obtained

$$\vec{\mathbf{C}} = \hat{\mathbf{E}}^{-1} \cdot \vec{\mathbf{S}} \tag{21}$$

This equation allows one to compute nine components of vector $\vec{\mathbf{C}}$. For convenience of further manipulations we arrange them in equivalent 3×3 matrix form

$$\hat{\mathbf{C}} = \begin{pmatrix} \langle C_{11}\rangle & \langle C_{12}\rangle & \langle C_{13}\rangle \\ \langle C_{21}\rangle & \langle C_{22}\rangle & \langle C_{23}\rangle \\ \langle C_{31}\rangle & \langle C_{32}\rangle & \langle C_{33}\rangle \end{pmatrix} \tag{22}$$

and then obtain the respective matrix of effective compliances

$$\hat{\mathbf{A}} = \hat{\mathbf{C}}^{-1} = \begin{pmatrix} \langle A_{11}\rangle & \langle A_{12}\rangle & \langle A_{13}\rangle \\ \langle A_{21}\rangle & \langle A_{22}\rangle & \langle A_{23}\rangle \\ \langle A_{31}\rangle & \langle A_{32}\rangle & \langle A_{33}\rangle \end{pmatrix} \tag{23}$$

From the nine effective compliance components above we can further derive nine effective engineering constants:

$$\langle E_1\rangle = \frac{1}{\langle A_{11}\rangle}, \quad \langle E_2\rangle = \frac{1}{\langle A_{22}\rangle}, \quad \langle E_3\rangle = \frac{1}{\langle A_{33}\rangle} \tag{24}$$

$$\begin{gathered} \langle \nu_{12}\rangle = -\frac{\langle A_{21}\rangle}{\langle A_{11}\rangle}, \quad \langle \nu_{13}\rangle = -\frac{\langle A_{31}\rangle}{\langle A_{11}\rangle}, \quad \langle \nu_{23}\rangle = -\frac{\langle A_{32}\rangle}{\langle A_{22}\rangle}, \\ \langle \nu_{21}\rangle = -\frac{\langle A_{12}\rangle}{\langle A_{22}\rangle}, \quad \langle \nu_{31}\rangle = -\frac{\langle A_{13}\rangle}{\langle A_{33}\rangle}, \quad \langle \nu_{32}\rangle = -\frac{\langle A_{23}\rangle}{\langle A_{33}\rangle} \end{gathered} \tag{25}$$

Theoretically, nine effective engineering constants should satisfy the reciprocity equations

$$\langle E_1\rangle\langle \nu_{21}\rangle = \langle E_2\rangle\langle \nu_{12}\rangle, \langle E_1\rangle\langle \nu_{31}\rangle = \langle E_3\rangle\langle \nu_{13}\rangle, \langle E_2\rangle\langle \nu_{32}\rangle = \langle E_3\rangle\langle \nu_{23}\rangle \tag{26}$$

however in a view of inevitable computational inaccuracies, they may not be satisfied exactly. If so, one can compute all six Poisson's ratios from (25), substitute them into (26) and check discrepancy between the right and left sides. The result can be used as the accuracy indicator of performed analysis. Then, the following symmetric compliance matrix can be defined:

$$\hat{\mathbf{A}} = \begin{pmatrix} \langle A_{11}\rangle & \frac{\langle A_{12}\rangle + \langle A_{21}\rangle}{2} & \frac{\langle A_{13}\rangle + \langle A_{31}\rangle}{2} \\ \frac{\langle A_{21}\rangle + \langle A_{12}\rangle}{2} & \langle A_{22}\rangle & \frac{\langle A_{23}\rangle + \langle A_{32}\rangle}{2} \\ \frac{\langle A_{31}\rangle + \langle A_{13}\rangle}{2} & \frac{\langle A_{32}\rangle + \langle A_{23}\rangle}{2} & \langle A_{33}\rangle \end{pmatrix} \tag{27}$$

and respective Poisson's ratios can be determined from the equations

$$\begin{gathered} \langle \nu_{12}\rangle = -\frac{\langle A_{21}\rangle + \langle A_{12}\rangle}{2\langle A_{11}\rangle}; \quad \langle \nu_{13}\rangle = -\frac{\langle A_{31}\rangle + \langle A_{13}\rangle}{2\langle A_{11}\rangle}; \\ \langle \nu_{23}\rangle = -\frac{\langle A_{32}\rangle + \langle A_{23}\rangle}{2\langle A_{22}\rangle} \\ \langle \nu_{21}\rangle = -\frac{\langle A_{12}\rangle + \langle A_{21}\rangle}{2\langle A_{22}\rangle}; \quad \langle \nu_{31}\rangle = -\frac{\langle A_{13}\rangle + \langle A_{31}\rangle}{2\langle A_{33}\rangle}; \\ \langle \nu_{32}\rangle = -\frac{\langle A_{23}\rangle + \langle A_{32}\rangle}{2\langle A_{33}\rangle} \end{gathered} \tag{28}$$

In this case the reciprocity conditions (25) will be satisfied exactly.

Further, in order to compute effective shear moduli, we relate applied shear strains to volumetrically averaged shear stresses obtained from six computational experiments (iv)–(ix):

$$\begin{gathered} \langle \sigma_{xy}\rangle = \langle G_{12}\rangle \varepsilon^0_{xy}, \quad \langle \sigma_{yx}\rangle = \langle G_{21}\rangle \varepsilon^0_{yx}, \quad \langle \sigma_{xz}\rangle = \langle G_{13}\rangle \varepsilon^0_{xz}, \\ \langle \sigma_{zx}\rangle = \langle G_{31}\rangle \varepsilon^0_{zx}, \quad \langle \sigma_{yz}\rangle = \langle G_{23}\rangle \varepsilon^0_{yz}, \quad \langle \sigma_{zy}\rangle = \langle G_{32}\rangle \varepsilon^0_{zy} \end{gathered} \tag{29}$$

The respective effective shear moduli are then obtained as follows:

$$\begin{gathered} \langle G_{12}\rangle = \frac{\langle \sigma_{xy}\rangle}{\varepsilon^0_{xy}}, \quad \langle G_{21}\rangle = \frac{\langle \sigma_{yx}\rangle}{\varepsilon^0_{yx}}, \quad \langle G_{13}\rangle = \frac{\langle \sigma_{xz}\rangle}{\varepsilon^0_{xz}}, \\ \langle G_{31}\rangle = \frac{\langle \sigma_{zx}\rangle}{\varepsilon^0_{zx}}, \quad \langle G_{23}\rangle = \frac{\langle \sigma_{yz}\rangle}{\varepsilon^0_{yz}}, \quad \langle G_{32}\rangle = \frac{\langle \sigma_{zy}\rangle}{\varepsilon^0_{zy}} \end{gathered} \tag{30}$$

Of course, theoretically the following pairs of shear moduli have to be identical

$$\langle G_{21}\rangle = \langle G_{12}\rangle, \quad \langle G_{31}\rangle = \langle G_{13}\rangle, \quad \langle G_{32}\rangle = \langle G_{23}\rangle \tag{31}$$

However, computational inaccuracies may result in certain discrepancies between the right and left hand sides of (31). The following mean values can be adopted in such case:

$$\begin{gathered} \langle G_6\rangle = \frac{\langle G_{12}\rangle + \langle G_{21}\rangle}{2}; \quad \langle G_5\rangle = \frac{\langle G_{13}\rangle + \langle G_{31}\rangle}{2}; \\ \langle G_4\rangle = \frac{\langle G_{23}\rangle + \langle G_{32}\rangle}{2} \end{gathered} \tag{32}$$

Effective elastic properties under applied stresses

In the case of applied surface tractions (in the context of this theoretical development they can also be termed ''stresses'') we also perform nine computational ''experiments'', similar to the ones (i)–(ix) described in Section ''Effective elastic properties under applied strains''. For this purpose we just have to replace strains with stresses and vice versa. In all nine computational experiments the applied stresses are assumed uniformly distributed over the respective sides of Mosaic parallelepiped. The following notations are used to denote applied stresses: σ_x^0 in case (I), σ_y^0 in case (II), σ_z^0 in case (III), σ_{xy}^0 in case (IV), σ_{yx}^0 in case (V), σ_{xz}^0 in case (VI), σ_{zx}^0 in case (VII), σ_{yz}^0 in case (VIII), and σ_{zy}^0 in case (IX). The computed and then volumetrically averaged stresses and strains are denoted:

In case (I): $\left\langle \sigma_y^x \right\rangle, \left\langle \sigma_z^x \right\rangle, \left\langle \varepsilon_x^x \right\rangle, \left\langle \varepsilon_y^x \right\rangle, \left\langle \varepsilon_z^x \right\rangle$

In case (II): $\left\langle \sigma_x^y \right\rangle, \left\langle \sigma_z^y \right\rangle, \left\langle \varepsilon_x^y \right\rangle, \left\langle \varepsilon_y^y \right\rangle, \left\langle \varepsilon_z^y \right\rangle$

In case (III): $\left\langle \sigma_x^z \right\rangle, \left\langle \sigma_y^z \right\rangle, \left\langle \varepsilon_x^z \right\rangle, \left\langle \varepsilon_y^z \right\rangle, \left\langle \varepsilon_z^z \right\rangle$

In case (IV): $\left\langle \varepsilon_{xy} \right\rangle$

In case (V): $\left\langle \varepsilon_{yx} \right\rangle$

In case (VI): $\left\langle \varepsilon_{xz} \right\rangle$

In case (VII): $\left\langle \varepsilon_{zx} \right\rangle$

In case (VIII): $\left\langle \varepsilon_{yz} \right\rangle$

In case (IX): $\left\langle \varepsilon_{zy} \right\rangle$

For normal strains and stresses above, the superscript indicates ‘‘loading’’ direction, while the subscript indicates direction of ‘‘measured response’’. For shear strains above, first subscript corresponds to the loading direction while the second corresponds to the measured response direction. The applied and the measured normal stresses and strains are related through Hooke’s law for orthotropic material written in the following matrix form:

$$\hat{\mathbf{S}} \cdot \vec{\mathbf{A}} = \vec{\mathbf{E}} \tag{33}$$

Here, the following strain vector, stress matrix, and effective compliance vector are introdused:

$$\vec{\mathbf{E}} = \begin{bmatrix} \left\langle \varepsilon_x^x \right\rangle \\ \left\langle \varepsilon_y^x \right\rangle \\ \left\langle \varepsilon_z^x \right\rangle \\ \left\langle \varepsilon_x^y \right\rangle \\ \left\langle \varepsilon_y^y \right\rangle \\ \left\langle \varepsilon_z^y \right\rangle \\ \left\langle \varepsilon_x^z \right\rangle \\ \left\langle \varepsilon_y^z \right\rangle \\ \left\langle \varepsilon_z^z \right\rangle \end{bmatrix}; \; \hat{\mathbf{S}} = \begin{bmatrix} \sigma_x^0 & \left\langle \sigma_y^x \right\rangle & \left\langle \sigma_z^x \right\rangle & 0 & 0 & 0 & 0 & 0 & 0 \\ 0 & 0 & 0 & \sigma_x^0 & \left\langle \sigma_y^x \right\rangle & \left\langle \sigma_z^x \right\rangle & 0 & 0 & 0 \\ 0 & 0 & 0 & 0 & 0 & 0 & \sigma_x^0 & \left\langle \sigma_y^x \right\rangle & \left\langle \sigma_z^x \right\rangle \\ \left\langle \sigma_x^y \right\rangle & \sigma_y^0 & \left\langle \sigma_z^y \right\rangle & 0 & 0 & 0 & 0 & 0 & 0 \\ 0 & 0 & 0 & \left\langle \sigma_x^y \right\rangle & \sigma_y^0 & \left\langle \sigma_z^y \right\rangle & 0 & 0 & 0 \\ 0 & 0 & 0 & 0 & 0 & 0 & \left\langle \sigma_x^y \right\rangle & \sigma_y^0 & \left\langle \sigma_z^y \right\rangle \\ \left\langle \sigma_x^z \right\rangle & \left\langle \sigma_y^z \right\rangle & \sigma_z^0 & 0 & 0 & 0 & 0 & 0 & 0 \\ 0 & 0 & 0 & \left\langle \sigma_x^z \right\rangle & \left\langle \sigma_y^z \right\rangle & \sigma_z^0 & 0 & 0 & 0 \\ 0 & 0 & 0 & 0 & 0 & 0 & \left\langle \sigma_x^z \right\rangle & \left\langle \sigma_y^z \right\rangle & \sigma_z^0 \end{bmatrix}; \; \vec{\mathbf{A}} = \begin{bmatrix} \langle S_{11} \rangle \\ \langle S_{12} \rangle \\ \langle S_{13} \rangle \\ \langle S_{21} \rangle \\ \langle S_{22} \rangle \\ \langle S_{23} \rangle \\ \langle S_{31} \rangle \\ \langle S_{32} \rangle \\ \langle S_{33} \rangle \end{bmatrix} \tag{34}$$

By multiplying Eq. 33 with matrix $\hat{\mathbf{S}}^{-1}$, we obtain the following equation for the vector of effective compliances:

$$\vec{\mathbf{A}} = \hat{\mathbf{S}}^{-1} \cdot \vec{\mathbf{E}} \tag{35}$$

Then this vector is written in the form of 3×3 matrix

$$\hat{\mathbf{A}} = \begin{pmatrix} \langle A_{11} \rangle & \langle A_{12} \rangle & \langle A_{13} \rangle \\ \langle A_{21} \rangle & \langle A_{22} \rangle & \langle A_{23} \rangle \\ \langle A_{31} \rangle & \langle A_{32} \rangle & \langle A_{33} \rangle \end{pmatrix} \tag{36}$$

which yields effective engineering constants (24)–(25). If the computed matrix (36) is not exactly symmetric we can, analogously to the case of applied strains (see Section ‘‘Effective elastic properties under applied strains’’) derive symmetric matrix in the form (27) and then apply same equations for Poisson’s ratios (28).

Further, analogously with Section ‘‘Effective elastic properties under applied strains’’, we relate applied shear stresses to volumetrically averaged shear strains, obtained from six computational experiments (IV)–(IX). The following expressions are then obtained for effective shear moduli:

$$\begin{gathered} \langle G_{12} \rangle = \frac{\sigma_{xy}^0}{\left\langle \varepsilon_{xy} \right\rangle}, \quad \langle G_{21} \rangle = \frac{\sigma_{yx}^0}{\left\langle \varepsilon_{yx} \right\rangle}, \quad \langle G_{13} \rangle = \frac{\sigma_{xz}^0}{\left\langle \varepsilon_{xz} \right\rangle}, \\ \langle G_{31} \rangle = \frac{\sigma_{zx}^0}{\left\langle \varepsilon_{zx} \right\rangle}, \quad \langle G_{23} \rangle = \frac{\sigma_{yz}^0}{\left\langle \varepsilon_{yz} \right\rangle}, \quad \langle G_{32} \rangle = \frac{\sigma_{zy}^0}{\left\langle \varepsilon_{zy} \right\rangle} \end{gathered} \tag{37}$$

Like in the case of applied displacements, the pairs of computed effective shear moduli $\langle G_{12} \rangle$ and $\langle G_{21} \rangle, \langle G_{13} \rangle$ and $\langle G_{31} \rangle, \langle G_{23} \rangle$ and $\langle G_{32} \rangle$ may not be identical due to computational inaccuracies. Their mean values defined by Eq. 32 can be obtained in this case and used in applications.

Progressive failure analysis using 3-D Mosaic model

Failure modes and elastic property modification scheme

Consider again generic Mosaic parallelepiped shown in Fig. 1, now for the purpose of developing progressive failure analysis algorithm. Following the concept of Continuum Damage Mechanics, each homogeneous brick (meso-volume) is characterized by its ‘‘initial’’ elastic properties corresponding to undamaged state of the material, and a sequence of ‘‘damaged’’ states, each characterized by discounted elastic properties which are related to specific failure mode and to extent of imparted gradual damage. In the analysis approach adopted here, each brick in the Mosaic parallelepiped is assumed orthotropic in its principal axes of material symmetry (denoted 1, 2 and 3), though it can belong to more general cases of anisotropy in the global coordinate axes of Mosaic parallelepiped (denoted x, y and z). Accordingly, nine failure modes of each brick are taken into account, and the occurrence of each failure event is determined by a simple and mechanistically validated ultimate strain failure criterion. Failure analysis of each individual brick is performed in its local principal axes of symmetry. Table 1 describes the adopted failure modes and failure criteria accounted in the analysis, and also provides elastic property discount scheme.

If necessary, other suitable phenomenological failure criteria can be incorporated into the developed progressive failure analysis algorithm and computer code without any difficulty. In particular, the popular tensor-polynomial type failure criteria or Hashin’s failure conditions can replace some of the currently used ultimate strain failure conditions. However, any complication of the analysis should be justified by experimental results. If intending to apply a more complex failure criterion than the ultimate strain, one has to keep in mind that there is a lot of experimental information on failure strain values for various fibers, matrices and unidirectional composites in the literature. At the same time, experimental data for ‘‘interactive term coefficients’’, which are contained in quadratic and other higher order failure criteria, are very rare and applicable to some specific composites only. Such data can be only obtained from biaxial loading tests which are complex, expensive and require special testing machines, fixtures, and unique specimen geometries. Therefore,

Table 1 Failure modes, failure conditions, and elastic property discount scheme

Mode no.	Failure type	Failure dir. or plane	Ultimate strain	Failure criteria	Modified Young’s moduli	Modified Poisson’s ratios	Modified shear moduli
1	T	1	$\varepsilon_1^{(q)\mathrm{T}}$	$\varepsilon_1^{(q)} \geq \varepsilon_1^{(q)\mathrm{T}}$	$\tilde{E}_1^{(q)} = \alpha_1^{(q)} E_1^{(q)}$	$\tilde{\nu}_{21}^{(q)} = \nu_{21}^{(q)}/\alpha_1^{(q)}$ $\tilde{\nu}_{31}^{(q)} = \nu_{31}^{(q)}/\alpha_1^{(q)}$	$\tilde{G}_4^{(q)} = \eta_1^{(q)} G_4^{(q)}$
2	T	2	$\varepsilon_2^{(q)\mathrm{T}}$	$\varepsilon_2^{(q)} \geq \varepsilon_2^{(q)\mathrm{T}}$	$\tilde{E}_2^{(q)} = \alpha_2^{(q)} E_2^{(q)}$	$\tilde{\nu}_{12}^{(q)} = \nu_{12}^{(q)}/\alpha_2^{(q)}$ $\tilde{\nu}_{32}^{(q)} = \nu_{32}^{(q)}/\alpha_2^{(q)}$	$\tilde{G}_5^{(q)} = \eta_2^{(q)} G_5^{(q)}$
3	T	3	$\varepsilon_3^{(q)\mathrm{T}}$	$\varepsilon_3^{(q)} \geq \varepsilon_3^{(q)\mathrm{T}}$	$\tilde{E}_3^{(q)} = \alpha_3^{(q)} E_3^{(q)}$	$\tilde{\nu}_{13}^{(q)} = \nu_{13}^{(q)}/\alpha_3^{(q)}$ $\tilde{\nu}_{23}^{(q)} = \nu_{23}^{(q)}/\alpha_3^{(q)}$	$\tilde{G}_6^{(q)} = \eta_3^{(q)} G_6^{(q)}$
4	C	1	$\varepsilon_1^{(q)\mathrm{C}}$	$-\varepsilon_1^{(q)} \geq \varepsilon_1^{(q)\mathrm{C}}$	$\tilde{E}_1^{(q)} = \beta_1^{(q)} E_1^{(q)}$	$\tilde{\nu}_{21}^{(q)} = \nu_{21}^{(q)}/\beta_1^{(q)}$ $\tilde{\nu}_{31}^{(q)} = \nu_{31}^{(q)}/\beta_1^{(q)}$	$\tilde{G}_4^{(q)} = \varphi_1^{(q)} G_4^{(q)}$
5	C	2	$\varepsilon_2^{(q)\mathrm{C}}$	$-\varepsilon_2^{(q)} \geq \varepsilon_2^{(q)\mathrm{C}}$	$\tilde{E}_2^{(q)} = \beta_2^{(q)} E_2^{(q)}$	$\tilde{\nu}_{12}^{(q)} = \nu_{12}^{(q)}/\beta_2^{(q)}$ $\tilde{\nu}_{32}^{(q)} = \nu_{32}^{(q)}/\beta_2^{(q)}$	$\tilde{G}_5^{(q)} = \varphi_2^{(q)} G_5^{(q)}$
6	C	3	$\varepsilon_3^{(q)\mathrm{C}}$	$-\varepsilon_3^{(q)} \geq \varepsilon_3^{(q)\mathrm{C}}$	$\tilde{E}_3^{(q)} = \beta_3^{(q)} E_3^{(q)}$	$\tilde{\nu}_{13}^{(q)} = \nu_{13}^{(q)}/\beta_3^{(q)}$ $\tilde{\nu}_{23}^{(q)} = \nu_{23}^{(q)}/\beta_3^{(q)}$	$\tilde{G}_6^{(q)} = \varphi_3^{(q)} G_6^{(q)}$
7	S	2–3	$\varepsilon_4^{(q)\mathrm{S}}$	$\left\lvert\varepsilon_4^{(q)}\right\rvert \geq \varepsilon_4^{(q)\mathrm{S}}$	$\tilde{E}_1^{(q)} = \chi_1^{(q)} E_1^{(q)}$	$\tilde{\nu}_{21}^{(q)} = \nu_{21}^{(q)}/\chi_1^{(q)}$ $\tilde{\nu}_{31}^{(q)} = \nu_{31}^{(q)}/\chi_1^{(q)}$	$\tilde{G}_4^{(q)} = \gamma_1^{(q)} G_4^{(q)}$
8	S	1–3	$\varepsilon_5^{(q)\mathrm{S}}$	$\left\lvert\varepsilon_5^{(q)}\right\rvert \geq \varepsilon_5^{(q)\mathrm{S}}$	$\tilde{E}_2^{(q)} = \chi_2^{(q)} E_2^{(q)}$	$\tilde{\nu}_{12}^{(q)} = \nu_{12}^{(q)}/\chi_2^{(q)}$ $\tilde{\nu}_{32}^{(q)} = \nu_{32}^{(q)}/\chi_2^{(q)}$	$\tilde{G}_5^{(q)} = \gamma_2^{(q)} G_5^{(q)}$
9	S	1–2	$\varepsilon_6^{(q)\mathrm{S}}$	$\left\lvert\varepsilon_6^{(q)}\right\rvert \geq \varepsilon_6^{(q)\mathrm{S}}$	$\tilde{E}_3^{(q)} = \chi_3^{(q)} E_3^{(q)}$	$\tilde{\nu}_{13}^{(q)} = \nu_{13}^{(q)}/\chi_3^{(q)}$ $\tilde{\nu}_{23}^{(q)} = \nu_{23}^{(q)}/\chi_3^{(q)}$	$\tilde{G}_6^{(q)} = \gamma_3^{(q)} G_6^{(q)}$

Note: ‘‘T’’ stands for tension, ‘‘C’’ for compression, and ‘‘S’’ for shear.

even having one of those failure criteria incorporated in structural analysis code does mean that it will become a practical tool.

Some additional explanations of Table 1 would be in place. First, superscript q identifies sequential number of homogeneous material element, which elastic properties are discounted in the given step of gradual failure process. This can have two different meanings: it may correspond to a discrete element (see Fig. 4) determined by the chosen computational mesh, or it may correspond to a material brick (meso-volume) in Mosaic parallelepiped of Fig. 1. The first case is, obviously, more general, because it allows one to model gradual failure within each homogeneous material brick. However, its realization consistent with the general methodology adopted here is not simple. Indeed, after discounting elastic properties of some discrete element within meso-volume, a new, smaller meso-volume within the original one would be created. Accordingly, after that we have to change the primary division of Mosaic parallelepiped into material bricks, in order to account for the presence of this new meso-volume. This procedure has to be repeated after each consecutive failure of discrete elements. The computer implementations of such process is possible, but algorithmically complex, and may result in significant increase of the analysis time.

On the other hand, if superscript q used in Table 1 is assumed identical with superscript s used for notation of material bricks (meso-volumes), the failure occurrence at any point of the material brick would result in discounting its respective elastic properties. In this case the original meso-volume mesh would not be changed during entire progressive failure process. This approach is much easier for computer code realization, but may be too severe in discounting elastic properties and, accordingly, too conservative in predicting ultimate failure load.

One possible compromise to be explored here is to make addition to the algorithm which will partially discount properties of the whole meso-volume with account for the volume fraction of the failed discrete element. For example, if failure Mode 1 is realized in discrete element q having volume $V^{(q)}$, and this discrete element belongs to brick s having volume $V^{(s)}$, then instead of using the discounting rules $\tilde{E}_1^{(q)} = \alpha_1^{(q)} E_1^{(q)}$ or $\tilde{E}_1^{(s)} = \alpha_1^{(s)} E_1^{(s)}$, the following is applied: $\tilde{E}_1^{(s)} = E_1^{(s)}\left[1 - \left(1 - \alpha_1^{(s)}\right) V^{(q)}/V^{(s)}\right] = \hat{\alpha}_1^{(s)} E_1^{(s)}$. If using this approach, the original discount coefficients $\alpha_k^{(s)}, \beta_k^{(s)}, \chi_k^{(s)}, \eta_k^{(s)}, \varphi_k^{(s)}$ and $\gamma_k^{(s)} (k = 1, 2, 3)$ have to be replaced by

$$\begin{aligned}
&\hat{\alpha}_k^{(s)} = 1 - \left(1 - \alpha_k^{(s)}\right) V^{(q)}/V^{(s)}, \quad \hat{\beta}_k^{(s)} = 1 - \left(1 - \beta_k^{(s)}\right) V^{(q)}/V^{(s)},\\
&\hat{\chi}_k^{(s)} = 1 - \left(1 - \chi_k^{(s)}\right) V^{(q)}/V^{(s)},\\
&\hat{\eta}_k^{(s)} = 1 - \left(1 - \eta_k^{(s)}\right) V^{(q)}/V^{(s)}, \quad \hat{\varphi}_k^{(s)} = 1 - \left(1 - \varphi_k^{(s)}\right) V^{(q)}/V^{(s)},\\
&\hat{\gamma}_k^{(s)} = 1 - \left(1 - \gamma_k^{(s)}\right) V^{(q)}/V^{(s)}
\end{aligned} \tag{38}$$

If $V^{(q)} = V^{(s)}$, Eqs. 38 yield $\hat{\alpha}_k^{(s)} = \alpha_k^{(s)}, \hat{\beta}_k^{(s)} = \beta_k^{(s)}, \hat{\chi}_k^{(s)} = \chi_k^{(s)}, \hat{\eta}_k^{(s)} = \eta_k^{(s)}, \hat{\varphi}_k^{(s)} = \varphi_k^{(s)}$ and $\hat{\gamma}_k^{(s)} = \gamma_k^{(s)}$. Table 2 illustrates numerical values obtained from (38) for some combinations of $\alpha_k^{(s)}$ and $V^{(q)}/V^{(s)}$. Reasonably, the smaller the volume fraction of discrete element in its meso-volume, the lesser the effect of its modulus discount on overall decrease of the meso-volume modulus.

Though the proposed "intermediate" approach has no mechanistic substantiation, its logics is right and its implementation in computer code is very simple, because it only requires to add computation of $V^{(q)}/V^{(s)}$ for all discrete elements and then calculate $\hat{\alpha}_k^{(s)}, \hat{\beta}_k^{(s)}, \hat{\chi}_k^{(s)}, \hat{\eta}_k^{(s)}, \hat{\varphi}_k^{(s)}$ and $\hat{\gamma}_k^{(s)}$ from Eqs. 38. And no new empirical parameters are added to the analysis scheme. Those remain the original discount coefficients $\alpha_k^{(s)}, \beta_k^{(s)}, \chi_k^{(s)}, \eta_k^{(s)}, \varphi_k^{(s)}$ and $\gamma_k^{(s)}$, which can be obtained either from correlations between analysis results and experimental data, or from a lower level fracture mechanics analysis. The latter one usually relates these coefficients to the orientation, size and spacing of certain arrays of microcracks/damage imparted in a homogeneous meso-volume under specified load. Both ways have been extensively studied in literature on Continuum Damage Mechanics, which accumulated knowledge will be implemented in further developments of progressive failure models and algorithms within 3-D Mosaic approach.

While the discount scheme for Young's moduli adopted in Table 1 and explained above is intuitively

Table 2 Numerical values of $\hat{\alpha}_k^{(s)}$ for different combinations of $\alpha_k^{(s)}$ and $V^{(q)}/V^{(s)}$

$\alpha_k^{(s)}$	$\hat{\alpha}_k^{(s)}$		
	$V^{(q)}/V^{(s)} = 0.9$	$V^{(q)}/V^{(s)} = 0.5$	$V^{(q)}/V^{(s)} = 0.1$
0.1	0.19	0.55	0.91
0.2	0.28	0.6	0.92
0.3	0.37	0.65	0.93
0.4	0.46	0.7	0.94
0.5	0.55	0.75	0.95
0.6	0.64	0.8	0.96
0.7	0.73	0.85	0.97
0.8	0.82	0.9	0.98
0.9	0.91	0.95	0.99

clear and usually not argued, the discount schemes for Poisson's ratios and shear moduli are by far less obvious. The logics used here is, that damaged discrete element, which may contain fiber, matrix, homogenized composite, etc., is still treated as a homogeneous orthotropic solid. Accordingly, all equations of solid mechanics apply; this includes the reciprocity relations between Young's moduli and Poisson's ratios: $E_1^{(q)}\nu_{21}^{(q)} = E_2^{(q)}\nu_{12}^{(q)}$, $E_1^{(q)}\nu_{31}^{(q)} = E_3^{(q)}\nu_{13}^{(q)}$, and $E_2^{(q)}\nu_{32}^{(q)} = E_3^{(q)}\nu_{23}^{(q)}$. After some Young's modulus, $E_1^{(q)}$ for example, is multiplied by its discount coefficient $\alpha_1^{(q)}$, the respective Poisson's ratios $\nu_{21}^{(q)}$ and $\nu_{31}^{(q)}$ have to be divided over the same discount coefficient in order to keep the reciprocity equations valid. One can verify that for all possible discounting cases of Young's moduli and Poisson's ratios in Table 1, the reciprocity equations are not violated. Note that when elastic modulus is reduced, the respective two Poisson's ratios are increased.

The above seemingly formal logics can be substantiated by a reasonable mechanistic interpretation. Indeed, the reduction of Young's modulus $E_1^{(q)}$, for example, can be interpreted as the result of formation of some array of microcracks/damage in plane 2-3. By their definition, Poisson's ratios $\nu_{21}^{(q)}$ and $\nu_{31}^{(q)}$ characterize material deformation in direction 1 when material is loaded in directions 2 and 3, respectively. So, the larger these Poisson's ratios are, the greater material deformation in direction 1 is. And, obviously, crack/damage formation in material plane 2-3 increases material compliance and, respectively, its deformation in direction 1. Thus, the modification scheme for Poisson's ratios in Table 1 is in a full agreement with this mechanistic interpretation.

The above mechanistic interpretation can also be used to explain the relations between discounting schemes for Young's moduli and shear moduli in Table 1. It seems obvious that crack/damage formation in plane 2-3 results in reduction of $E_1^{(q)}$ and, at the same time, in reduction of shear modulus in that plane, $G_4^{(q)}$. Analogously, crack/damage formation in plane 1-3 or plane 1-2 results in reduction of $E_2^{(q)}$ or $E_3^{(q)}$ and, at the same time, in reduction of $G_5^{(q)}$ or $G_6^{(q)}$, respectively. So, intuitively the pairs of discount coefficients $\alpha_k^{(q)}$ and $\eta_k^{(q)}, \beta_k^{(q)}$ and $\varphi_k^{(q)}, \chi_k^{(q)}$ and $\gamma_k^{(q)}$ are implicitly related via common micromechanical mechanisms of crack/damage formation. Yet, this problem has not been well addressed in the literature. Due to that, in current version of 3-D Mosaic progressive failure analysis all of the discount coefficients in Table 1 are treated as formally independent input parameters.

Principal steps of the computational algorithm

Next we describe principal steps of the developed computational algorithm for progressive failure analysis, with account for the nine failure modes described in Table 1, and with respective modifications of the elastic characteristics.

Step 1. Run 3-D Mosaic analysis with some arbitrary magnitude of applied load, say P_0, or applied displacement, say U_0. A set of rendering points $\{x, y, z\}$ is selected by choosing number of intervals in x, y and z directions of the Mosaic structure. Strains are computed at those points.

Step 2. All of the computed strains are normalized over their respective ultimate values taken from input data for each individual brick in Mosaic parallelepiped. Of course, the normalization factors are different for distinct material bricks and even for the same material bricks having different orientation with respect to global axes x, y and z. Besides, the normalization factors may be different for the same material in same direction when exposed to tensile versus compressive stress. This step is performed for all points selected in Step 1. As the result, for each normalized (positive, negative or shear) strain component the largest magnitude is determined and further termed ''failure strain indicator''. Now, we have nine such indicators computed:

$$\begin{aligned}
&R_1^{\mathrm{T}} = \frac{\varepsilon_1^{(q_1)}(\tilde{x},\tilde{y},\tilde{z})}{\varepsilon_1^{(q_1)T}},\ R_2^{\mathrm{T}} = \frac{\varepsilon_2^{(q_2)}(\tilde{x},\tilde{y},\tilde{z})}{\varepsilon_2^{(q_2)T}},\ R_3^{\mathrm{T}} = \frac{\varepsilon_3^{(q_3)}(\tilde{x},\tilde{y},\tilde{z})}{\varepsilon_3^{(q_3)T}},\\
&R_1^{\mathrm{C}} = \frac{\varepsilon_1^{(q_4)}(\tilde{x},\tilde{y},\tilde{z})}{\varepsilon_1^{(q_4)C}},\ R_2^{\mathrm{C}} = \frac{\varepsilon_1^{(q_5)}(\tilde{x},\tilde{y},\tilde{z})}{\varepsilon_2^{(q_5)C}},\ R_3^{\mathrm{C}} = \frac{\varepsilon_3^{(q_6)}(\tilde{x},\tilde{y},\tilde{z})}{\varepsilon_3^{(q_6)C}},\\
&R_4^{\mathrm{S}} = \frac{\left|\varepsilon_{23}^{(q_7)}(\tilde{x},\tilde{y},\tilde{z})\right|}{\varepsilon_4^{(q_7)S}},\ R_5^{\mathrm{S}} = \frac{\left|\varepsilon_{13}^{(q_8)}(\tilde{x},\tilde{y},\tilde{z})\right|}{\varepsilon_5^{(q_8)S}},\ R_6^{\mathrm{S}} = \frac{\left|\varepsilon_{23}^{(q_9)}(\tilde{x},\tilde{y},\tilde{z})\right|}{\varepsilon_6^{(q_9)S}}
\end{aligned} \tag{39}$$

By using different superscripts $q_1, \ldots, q_9$ in above equations we emphasize that each of the nine left hand side values may be reached in different discreet elements. The largest among these nine failure strain indicators is then determined and shown in the postprocessor window together with the following characteristics of the first failure occurrence: three failure point coordinates $\tilde{x}, \tilde{y}, \tilde{z}$, three integers $\{l, m, n\}$ identifying the corresponding material brick (meso-volume), the failure mode (''T'', ''C'', or ''S''), the axis index (1, 2 or 3) for tensile and compressive failures, or the plane index (23, 31, or 12) for shear failure.

Step 3. The applied load P_0 or applied displacement U_0 magnitude under which the first analysis has been run is normalized over the largest among all computed failure strain indicators (39). The obtained load magnitude P_1^F constitutes ''first failure load'', or the displacement magnitude U_1^F constitutes ''first failure displacement''.

Step 4. Knowing the first failure occurrence mode and location, initial elastic characteristics of the respective meso-volume brick or discrete element are discounted in accordance with Table 1.

Step 5. Step 1 is repeated. 3-D Mosaic code is run again under first failure load P_1^F or first failure displacement U_1^F in the input.

Step 6. Step 2 is repeated. If any of the failure strain indicators in (39) reaches value 1, the second failure has occurred. The respective failure mode and location are identified.

Step 7. Step 3 is repeated. The ''second failure load'' P_2^F or ''second failure displacement'' U_2^F is determined. All second failure characteristics can be viewed in the respective postprocessor window.

Step 8. Then Step 4 is repeated. If no new failure has occurred in this step, the applied load or displacement magnitude can be increased, and the respective analysis steps repeated.

The process can be continued until all material bricks (meso-volumes) fail in one of the global coordinate directions x, y, z, or in one of the planes y–z, z–x, x–y. Any of these two results can be viewed as total loss of load-bearing capacity of the structure. In current version 3-D MOSAIC code can run in cycles until the ultimate failure condition is reached.

Geometric models of 3-D woven fabrics and composites

Design and fabrication of 3-D woven preforms and composites

3TEX, Inc. has exclusive license to patent issued to North Carolina State University [80] for special method of forming 3-D woven fabrics. Those interested in details of the method, currently applied industrial 3-D weaving process, available automated 3-D weaving machines and their capabilities, are directed to the patent and recent publications [3, 4, 8].

A representative model of 3-D woven fabric is shown in Fig. 6. The principal design parameters are: size of the warp, fill and Z yarns (characterized in yield/lb), number of warp-directional yarns placed within 1 in. (2.54 cm) interval in the width direction (characterized in ends/inch), number of fill-directional yarns placed within 1 in. interval in the longitudinal, fabric formation direction (characterized in picks/inch), and Z-yarn insertion parameter in the width direction (characterized in ends/inch). In addition to that, the designer has to assume cross-sectional shape of each yarn type and specify the path of Z-yarn in through-thickness direction. In principle, having these design parameters enables to generate a Fabric Geometry Model, for example, the one shown in Fig. 6, using Solid Works or other suitable software.

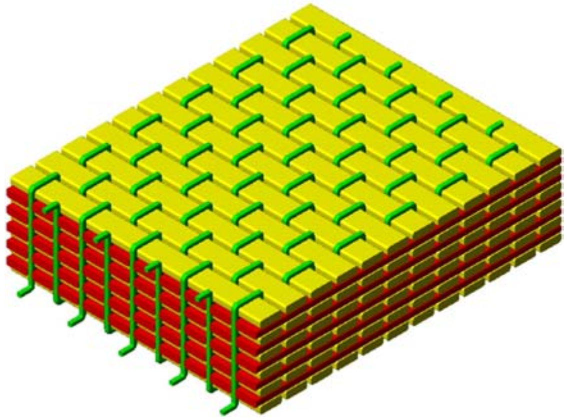

Fig. 6 Representative element of 3-D woven fabric [3]. Five layers of warp yarns shown in red, six layers of filling yarns shown in yellow, and through thickness (Z) yarns shown in green

3TEX has designed and fabricated a variety of single-layer 3-D orthogonal woven S-2 glass fiber fabrics, which are of particular interest for different composite armor systems, see [1, 5, 9, 17]. A photograph of one representative fabric of this class, containing two warp and three fill layers, and having areal weight 3.46 kg/m^2 (93 oz/yd^2) is shown in Fig. 7a. For brevity this fabric will be further identified by its areal weight and called ''93oz fabric''. Both warp layers are made of 250 yield/lb S-2 glass roving; 5 double ends/inch insertion used; 50.8% of total fiber amount in the preform is placed in warp direction. Two outer fill layers are made of 750 yield/lb S-2 glass roving, while the middle fill layer is made of 250 yield/lb S-2 glass roving; double yarn insertion with 5.5 picks/inch used in filling direction; 45.6% of total fiber volume is placed in fill direction. Finally, Z-yarn is 1250 yield/lb S-2 glass roving (5 ends/inch insertion); 3.6% of total fiber amount in the preform belongs to Z-yarns, however only about 2% goes in through thickness direction; rest of it (about 1.6% of total fiber volume) forms ''Z-crowns'', which are clearly seen in Fig. 7a; those are oriented in the warp direction and pass above filling yarns on the fabric surface. The described design yields nearly balanced fabric with respect to the fiber content in warp and fill directions; the fiber content in warp direction, 50.8%, is slightly higher than in fill direction, 45.6%.

Composite panels were fabricated from 93oz S-2 glass fabric by 3TEX using Vacuum Assisted Resin Transfer Molding (VARTM) process with Dow Derakane 8084 Epoxy-Vinyl Ester resin. Fiber volume

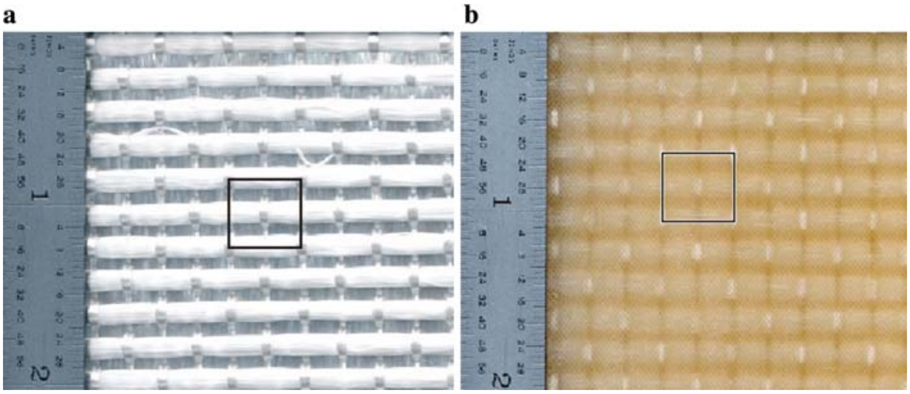

Fig. 7 Face view of 93oz 3-D woven fabric (**a**) and VARTM processed composite (**b**) with representative surface elements in frame

fraction of 49% in produced composite panels was determined in accordance with ASTM D2584 standard. A photograph of composite panel fragment is shown in Fig. 7b. Comparison of Fig. 7a and 7b show that the fiber architecture seen in dry fabric was practically not affected by resin infusion and composite consolidation. Dimensions of the yarns, spaces between them, and their straightness are practically the same in Fig. 7b as in Fig. 7a. The dimensions of representative surface elements shown in Fig. 7 also look identical. The measured thickness of composite panel (ranging between 2.4 mm and 2.6 mm) is slightly smaller than the measured thickness of dry fabric (between 2.6 mm and 2.8 mm).

Computer generated 3-D geometric models of the fabric and composite elements (including selvage edge) are shown in Fig. 8. Photograph of composite panel cross section and detailed view of the fabric model cut side edge are shown in Fig. 9.

Photograph shown in Fig. 9a (this image is representative of all cross-sections of composite) reveals that the Z-yarn path is not what was expected for ''3-D orthogonal weave'' architecture. Indeed, Z-yarn is not exactly vertical, it rather follows a ''broken line'' pattern with three characteristic segments inclined at different angles. In the model of Fig. 9b, which was adjusted to mimic Z-yarn path of Fig. 9a as close as possible, it was assumed that two outer segments are inclined at 35° angle with respect to Z-axis, while the middle segment is exactly vertical. If desired, geometric models shown in Figs. 8 and 9b can be further modified to match the actual Z-yarn path in the composite even closer.

Further, it is clearly seen in Fig. 9a that the horizontal, ''warp-oriented'' segments of Z-yarn are substantially indented into the filling yarn laying under it. Such indentation is caused by tension applied to Z-yarns during weaving. This makes slight difference between Figs. 9a and 9b, because in the latter one the filling and Z-yarns in the ''crown'' area have constant thickness. These details of different yarn placement and their mutual interaction in 3-D woven composite would not considerably influence effective elastic properties or structural response in many loading cases, however they may be significant in ballistic penetration modeling, or double cantilever beam fracture test simulation, or any other problem in which correct modeling of Z-yarn breakage in the ''crown'' area is important. As some experimental observations show, failure of textile composites is often initiated at the crossover regions of yarns placed in different directions. Accordingly, the regions of mutually indented, orthogonally oriented filling and Z yarns should be considered as possible sites of initial failure.

Geometric model of the 93oz fabric composite Unit Cell, corresponding to the fabric and composite models of Figs. 8 and 9, is shown in Fig. 10a. It is worth noting that a ''zig-zag'' path of Z-yarn seen in Fig. 10a (with segments inclined at approximately 35° angle to z-axis) is specific for this particular fabric design. For example,

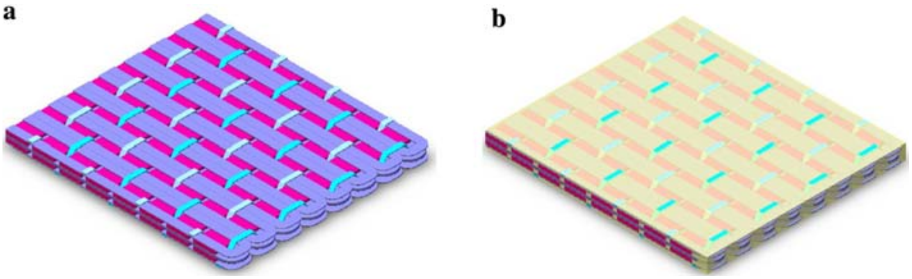

Fig. 8 Computer-generated models of 93oz 3-D woven fabric (**a**) and composite (**b**)

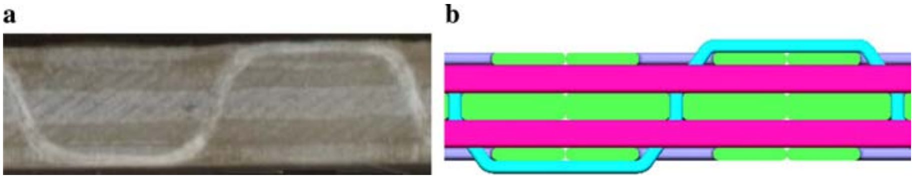

Fig. 9 Photograph of the side edge fragment of composite panel (**a**) and developed fabric model cross section (**b**)

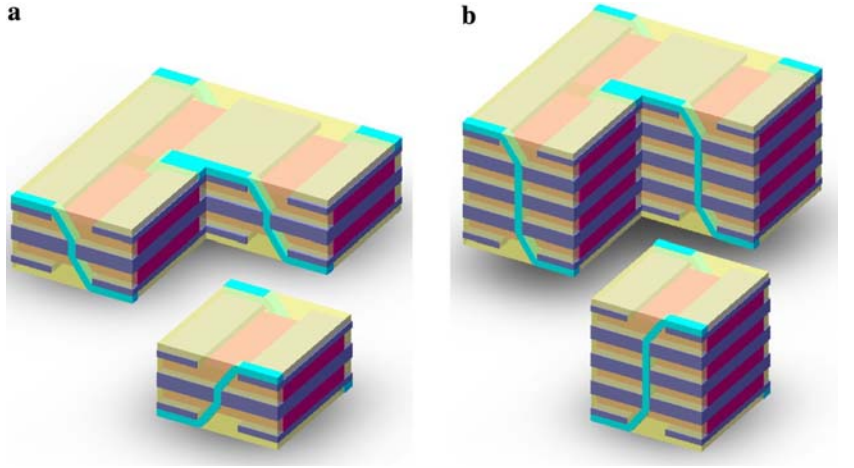

Fig. 10 Unit Cell models of 93oz (**a**) and 190oz (**b**) 3-D woven fabric composites

Unit Cell model of ‘‘190oz fabric’’ composite shown in Fig. 10b has Z-yarn path much closer to straight and vertical; this fabric is similar in its construction to the 93oz one, but contains 4 warp and 5 fill layers and is about twice thicker. Also, even within the same ‘‘2 warp–3 fill layer’’ construction, other fabrics have been designed and manufactured, in which Z-yarn path is much closer to straight and vertical. Particularly, Fig. 11 shows ‘‘98oz fabric’’ model which also has 2 warp and 3 fill layer construction, but with much smaller size of filling yarns in the outer layers and much tighter filling yarn packing. The manufactured 93oz and 98 oz preforms had close thickness and areal weight, however as experimental studies showed, mechanical properties of composites made with these preforms as well as their ballistic and blast performance characteristics differ considerably.

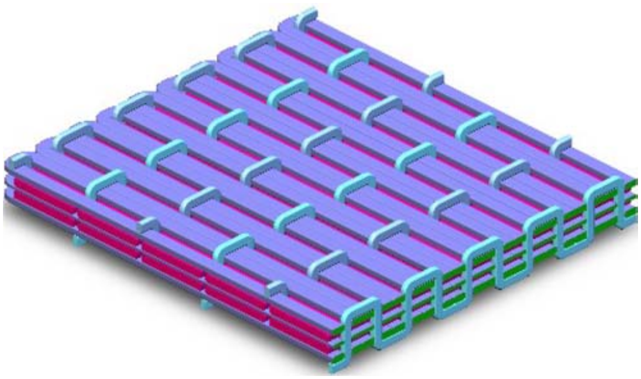

Fig. 11 Geometric model of 98oz 3-D woven fabric showing straight and vertical Z-yarn path

A variety of 3-D woven fabrics with nearly identical areal weight and thickness can be purposefully designed and manufactured for specific applications. It may happen though that the best basic mechanical performance (stiffness and strength) will not translate into the best ballistic, blast or low velocity impact performance. Moreover, even optimal fabric construction found for one particular armor application (say, personnel armor) may not be the best for the other armor applications (in vehicle armor, for example). Design optimization of 3-D woven fabrics for various practical composite applications is currently based on individual designer’s experience and intuition with some help of available experimental data, with practically no role of predictive analysis tools.

The following sections illustrate our initial efforts in the area of multi-scale applications of 3-D Mosaic model and variational analysis approach to 3-D orthogonal woven composites manufactured by 3TEX. This includes the following tasks: (i) 3-D stress/strain analysis of the 3-D woven composite Unit Cell using the methodology described in Section ‘‘Theoretical background of present 3-D Mosaic approach’’; (ii) application of 3-D volumetric averaging methodology described in Section ‘‘Volumetric averaging of stress/strain fields in 3-D Mosaic structures’’ that results in predictions of effective elastic properties of 3-D woven composite, (iii) 3-D analysis of 3-D woven composite beam under 3-point bending load, and (iv) application of progressive failure model and predictions of the sequence of failure events and ultimate in-plane tensile failure load. Numerical results obtained for tasks (ii), (iii) and (iv) will be compared with experimental data.

3-D stress/strain analysis of 3-D woven composite Unit Cell

Derivation of the Unit Cell model

Now we return to analysis of S-2 glass 93oz fabric composite and will start with discussion of its Unit Cell model, shown in Fig. 12a. This is essentially the same model as in Fig. 10a with notations of geometric parameters added. In order to finalize geometric characteristics of the Unit Cell, we applied iterative approach, using both fabric processing parameters and direct measurements made on the produced fabric and composite. The determined characteristics of this geometric model are:

$$\begin{aligned}
&W_x = F_x + Z_x = 2a = 4.618\,\text{mm};\ F_x = 4.326\,\text{mm};\\
&f_x = 3.028\,\text{mm};\ Z_x = 0.292\,\text{mm};\\
&F_y = W_y + Z_y = 2b = 5.08\,\text{mm};\ W_y = 4.171\,\text{mm};\\
&Z_y = 0.909\,\text{mm};\ W_z = 0.637\,\text{mm};\\
&F_z = 0.614\,\text{mm};\ f_z = 0.292\,\text{mm};\ z_z = 0.292\,\text{mm};\\
&Z_z = 2W_z + F_z + 2f_z = 2c = 2.472\,\text{mm};\\
&H_z = Z_z + 2z_z = 3.056\,\text{mm}
\end{aligned} \tag{40}$$

As discussed in Section ‘‘Design and fabrication of 3-D woven preforms and composites’’, the model of Fig. 12a does not account for indentation of the warp-oriented segments of Z-yarns into respective segments of filling yarns on the fabric surfaces. Due to this, thickness of the Unit Cell model is larger than that of the fabricated composite. Also, there is more resin on both faces of the Unit Cell model compared to the actual composite. As the result, total fiber volume fraction in the Unit Cell model of Fig. 12a is a little lower than in actual composite. In order to minimize these discrepancies, the modified Unit Cell model shown in Fig. 12b has been generated; its principal characteristics showed nearly identical to the ones measured on the actual composite. In this model, thin outer layers which contain matrix and small warp-directional segments of Z-yarns, are neglected. So, as seen in Fig. 12b, only those segments of Z-yarn which go in through-thickness direction are kept in the model. Total fiber volume fraction in the composite Unit Cell model of Fig. 12b match the experimental 49% value, under the assumption that so-called ‘‘yarn packing factor’’ (i.e. fiber volume fraction in resin-impregnated yarn) is 60% for all warp, fill and Z-yarns.

The Unit Cell model of Fig. 12b is still rather complex and requires very fine discretization mesh due to the presence of inclined Z-yarn segments. Following [18], this model is further modified for the sake of simplicity of its representation in terms of generic Mosaic parallelepiped of Fig. 1. Specifically, the inclined Z-yarn elements are smeared with their surrounding matrix into homogeneous bricks; this results in the Mosaic parallelepiped model shown in Fig. 13a. The four homogeneous bricks having monoclinic effective elastic properties in x–z plane represent the inclined Z-yarn segments surrounded by matrix. As follows from the equivalency between geometric models of Fig. 12b and 13a, these composite bricks have 16.5% fiber volume fraction.

The obtained Mosaic parallelepiped model of Fig. 13a contains five distinct materials (meso-volumes): three unidirectional composites corresponding to resin impregnated warp, fill and Z yarns, ‘‘smeared inclined’’ Z-yarn composite, and matrix pockets. Further, as illustrated in Fig. 13a, the model is non-uniformly divided into some number of 3-D ‘‘discrete elements’’ by three sets of planes perpendicular to x, y and z axes. This discretization mesh will

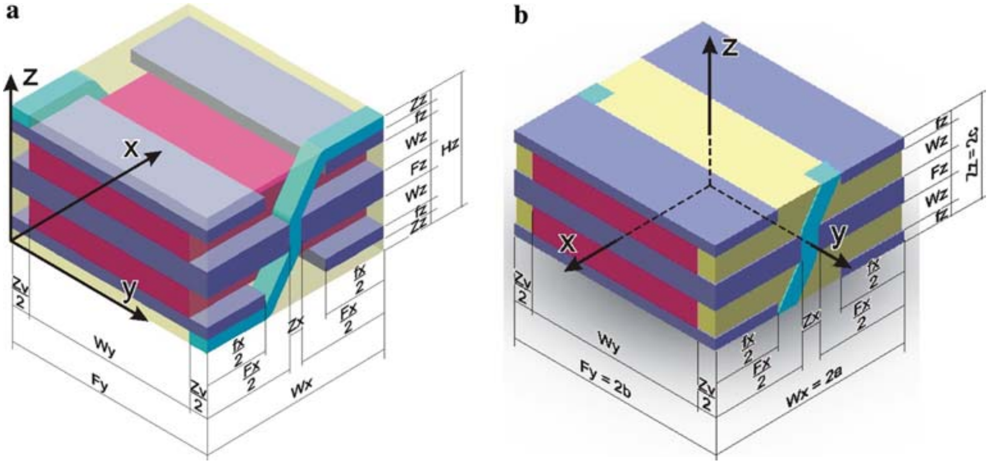

Fig. 12 Unit Cell model of 93oz fabric composite

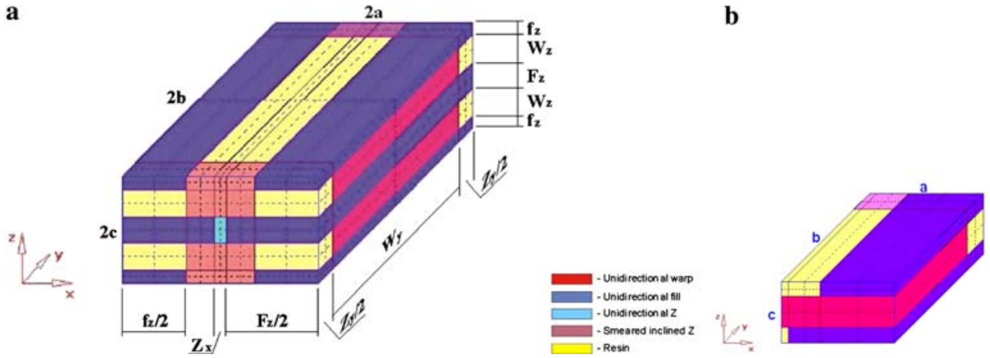

Fig. 13 3-D Mosaic model of 93oz 3-D weave composite Unit Cell (**a**) and its 1/8th part (**b**)

be used in further numerical examples. The other model, which will be used in those problems where symmetry applies with respect to three planes perpendicular to x, y and z axes and passing through the center of the parallelepiped, is 1/8th part of the Unit Cell shown in Fig. 13b.

Elastic properties of the meso-volumes

Properties of all material bricks (meso-volumes) contained in the Mosaic parallelepiped model of Fig. 13a have to be determined prior to analysis and used as input data. This can be done either experimentally or by applying some appropriate predictive analysis method at the lower level of structural hierarchy. For the sake of illustrating a multi-scale capability of 3-D Mosaic analysis approach, effective elastic properties of unidirectional composite made of S-2 glass fiber roving (60% fiber volume fraction) and Dow Derakane 8084 Vinyl Ester-Epoxy resin have been predicted in [18] with the use of micromechanics model shown in Fig. 14. Total fiber volume fraction V_f in the composite is related to geometric parameters a and b by equation $b/a = 1/\sqrt{V_f}$. The condition V_f =0.6 yields b/a=1.29. The following properties of isotropic S-2 glass fiber and isotropic Dow Derakane 8084 Vinyl Ester-Epoxy are further used:

$$E_f = 86.9\,\text{GPa},\ \nu_f = 0.22,\ E_m = 3.17\,\text{GPa},\ \nu_m = 0.35 \qquad (41)$$

First, 3-D stress/strain analysis was performed for Model 2 shown in Fig. 14. Then, “Applied Strain” and “Applied Stress” approaches with volumetric averaging of 3-D stress and strain fields have been applied in accordance with the methodology of Section “Volumetric averaging of stress/strain fields in 3-D Mosaic structures”. Numerical results obtained for effective

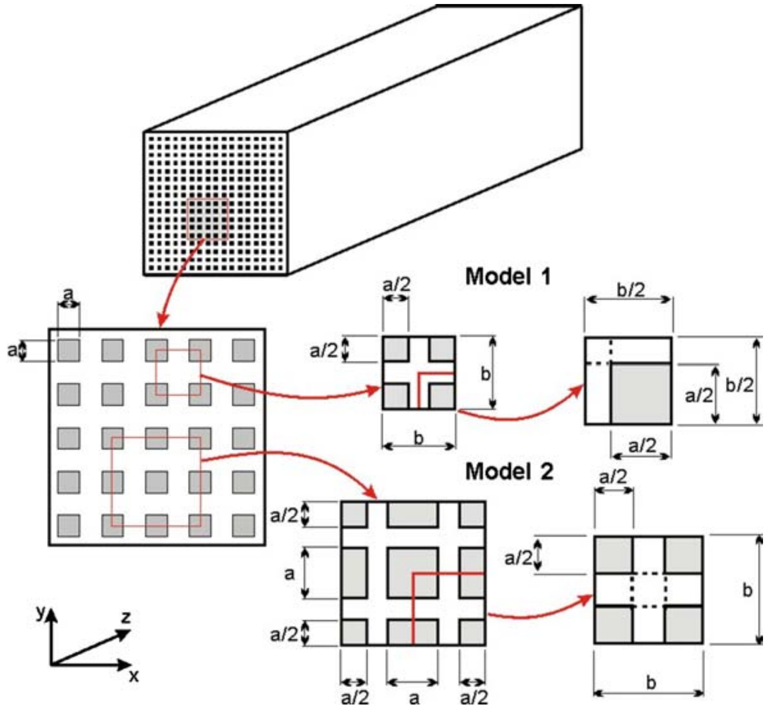

Fig. 14 3-D Mosaic models of unidirectional composite Unit Cells [18]

elastic constants with Bernstein basis functions having degree 3 and degree 4 are presented in Table 3. Numerical results obtained with SAM and experimental data from fiber manufacturer's (Advanced Glassfiber Yarns, LLC) website, are also presented in the table.

It is seen in Table 3 that present results (for both applied displacement and applied stress cases) show clear convergence: the difference between results obtained with degrees 3 and 4 is negligible for all predicted elastic characteristics. A considerable difference is seen between the upper bounds (applied strains) and lower bounds (applied stresses) for $\langle E_L \rangle$, while for $\langle E_T \rangle$ and $\langle v_{TT} \rangle$ the difference is much smaller, and for $\langle v_{LT} \rangle$ it is negligible. Further, the applied strain approach provides upper bounds for $\langle E_L \rangle$ and $\langle E_T \rangle$, and lower bound for $\langle v_{TT} \rangle$. Results for $\langle E_L \rangle$ and $\langle v_{LT} \rangle$ obtained with present approach are very close to the SAM results and are in a good agreement with experimental data. For $\langle E_T \rangle$ the discrepancy with experimental data is more significant; this can be explained by possible difference between Young's modulus of the matrix adopted in the analysis and actual Young's modulus of unspecified "epoxy" resin used in fabrication of this composite. Yet, predictions of $\langle E_T \rangle$ obtained from 3-D Mosaic analysis are much closer to experimental data than respective predictions by SAM. Also it is seen in Table 1 that for $\langle v_{TT} \rangle$ present results are significantly lower than the SAM prediction, and that predicted values of $\langle G_L \rangle$ and $\langle G_T \rangle$ are considerably higher than the SAM predictions. We do not possess experimental data for these characteristics at the time.

In numerical examples considered further in this paper the following effective elastic properties of warp-, fill- and Z-unidirectional composites will be used (index 1 corresponds to fiber direction and indices 2, 3 to transverse directions):

$$\begin{aligned} &E_1 = 53.12\,\text{GPa},\ E_2 = E_3 = 14.66\,\text{GPa}, \\ &G_{12} = G_{13} = 4.24\,\text{GPa},\ G_{23} = 5.78\,\text{GPa}, \\ &v_{12} = v_{13} = 0.266,\ v_{23} = 0.268 \end{aligned} \tag{42}$$

3-D stress/strain analysis of the Unit Cell and convergence study

As a preambule, it is worth noting that 3-D stress/strain analysis of the Mosaic parallelepiped shown in Fig. 13a is complex task, and interpretation of numerical results is non-trivial. The analyzed structure consists of a large number of perfectly bonded bricks representing three unidirectional composites (having identical elastic properties (42) in their coordinate axes 1, 2 and 3 but different orientation), monoclinic composite representing inclined Z-yarn in matrix, and isotropic matrix itself. These distinct material bricks form a complex mixture of parallel and sequential connections. Probably, the best way to illustrate numerical results for this kind of 3-D stress/strain analysis problem is to make color "carpet" plots with two coordinates along in-plane axes of a plot and stress or strain component shown by iso-stress or iso-strain contours with respective values on them. The coordinate system origin is placed in the center of the Unit Cell, so coordinate x varies from $-a$ to a, coordinate y from $-b$ to b, and coordinate z from $-c$ to c.

Both the discretization mesh and degree of Bernstein basis functions can be varied when running specific analysis cases, particularly when performing convergence study. In the numerical examples presented here we kept the discretization mesh shown in Fig. 13a constant and varied degree of basis functions. It has to be noted that continuity conditions for strains and stresses within homogeneous material bricks (10)–(12) were not imposed in the forthcoming numerical examples. Due to this, small computational jumps of strains and stresses may be seen at some lines and points separating discrete elements within homogeneous material brick.

In the first boundary value problem solved, uniformly distributed displacements $-u_x^0$ and u_x^0 are applied in x direction to the sides $x = -a$ and $x = a$ of the Unit Cell. All other sides are free of forces or displacements. Second boundary value problem

Table 3 Elastic properties of V_f = 0.6 S-2 Glass/Dow Derakane 8084 Vinyl Ester-Epoxy unidirectional composite predicted by different analysis methods and obtained experimentally

Analysis Method	Polynomial degree	$\langle E_L \rangle$ GPa	$\langle E_T \rangle$ GPa	$\langle v_{LT} \rangle$	$\langle v_{TT} \rangle$	$\langle G_L \rangle$ GPa	$\langle G_T \rangle$ GPa
Present (applied strain)	3	53.12	14.68	0.265	0.267	4.28	3.92
	4	53.12	14.66	0.266	0.268	4.24	3.92
Present (applied stress)	3	44.50	13.28	0.265	0.295	–	
	4	44.46	13.22	0.265	0.296	–	
SAM		53.42	10.68	0.265	0.449	4.18	3.69
Experimental		56	18	0.27			

considers uniformly distributed displacements $-u_y^0$ and u_y^0 applied in y direction at the sides $y=-b$ and $y=b$, respectively. All other sides are free of forces or displacements. Third boundary value problem was solved for uniformly distributed displacements $-u_z^0$ and u_z^0 applied in z direction at the sides $z=-c$ and $z=c$, respectively. All other sides are free of forces or displacements. Numerical results for one selected strain components in each problem are shown in Figs. 15–17, respectively.

One important conclusion made from these numerical results is, that for all three considered boundary value problems, the symmetry conditions $u_x=0$ at at $x=0$, $u_y=0$ at $y=0$ and $u_z=0$ at $z=0$ can be applied simultaneously without affecting results for computed strains. Analogous study was performed for the stresses and led to the same conclusion. This means that 1/8th of the Unit Cell shown in Fig. 13b can be used in these analysis cases instead of the whole Unit Cell. This allows, in turn, reducing the size of each of the above three computational problems by approximately factor of 8, which is especially useful when conducting convergence studies with higher degree basis functions.

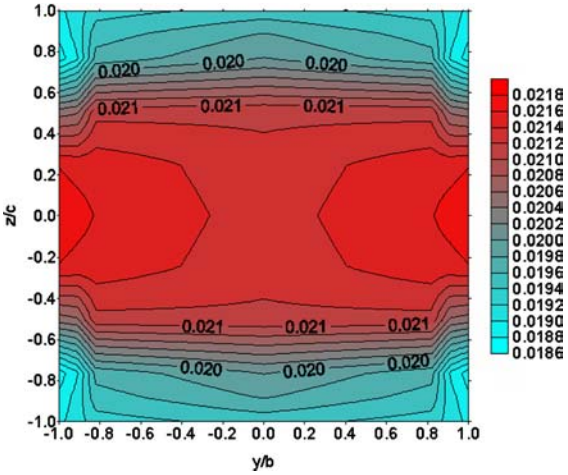

Fig. 15 Distribution of strain ε_x in y–z plane at $x=a$ for applied displacement in x direction

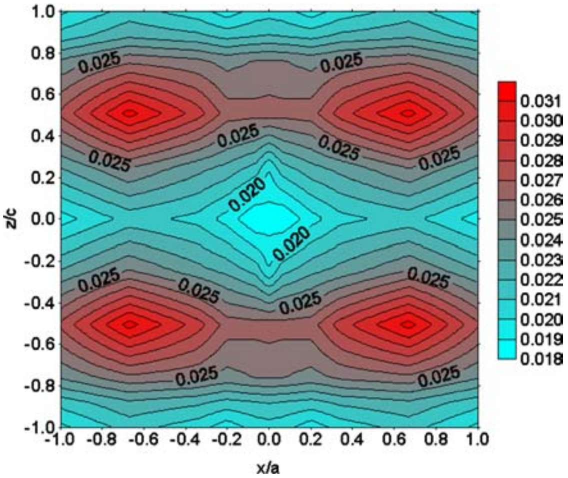

Fig. 16 Distribution of strain ε_y in x–z plane at $y=b$ for applied displacement in y direction

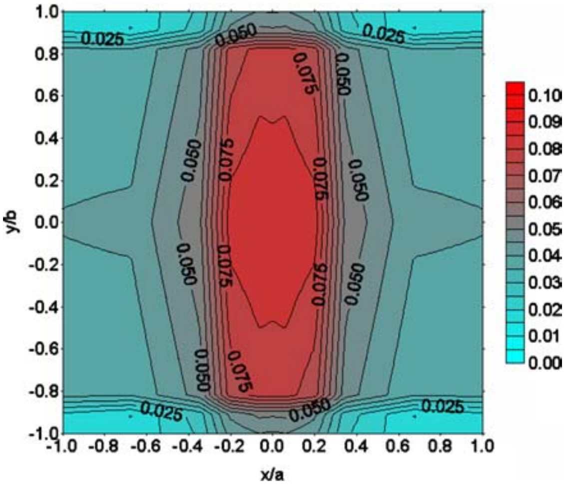

Fig. 17 Distribution of strain ε_z in x–y plane at $y=c$ for applied displacement in z direction

Further, convergence study has been performed for the same three boundary value problems, but solving 1/8th of the Unit Cell (see Fig. 13b) with respective symmetry conditions added. The origin of coordinate system remains in the center of the Unit Cell, so for its 1/8th part coordinate x varies from 0 to a, coordinate y from 0 to b, and coordinate z from 0 to c. Numerical results for the same strain components are presented in Figs. 18–20.

Figure 18 shows some differences among results for degrees 2, 3 and 4, whle the results for degrees 4 and 5 look indistinguishable. One can see in these plots that the strain distribution is rather uniform and the highest strain exceeds the lowest one only by 20%. Yet, even with this nearly uniform strain distribution, local strain gradients are clearly visible, which indicates high resolution of the performed analysis.

Similarly, Fig. 19 shows that there are some differences among results for degrees 2, 3 and 4, while the plots for degrees 4 and 5 look identical. In this case the strain distribution is not as smooth as in the previous case: the highest strain value corresponding to the matrix pocket is about two times higher than the lowest one corresponding to the filling-directional composite. Still, the regions of higher strain gradients are clearly seen.

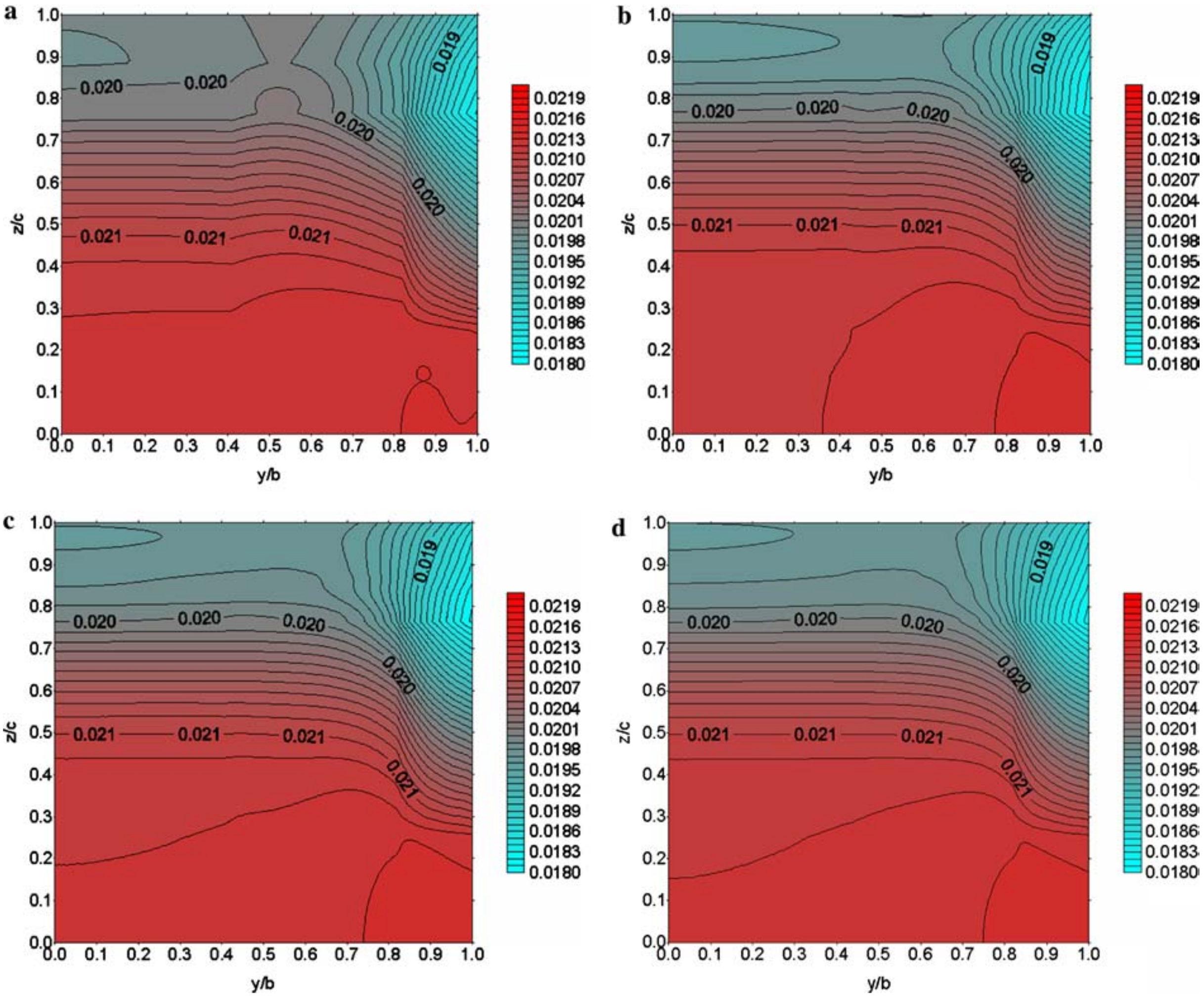

Fig. 18 Distributions of strain ε_x in y–z plane at $x = a$ for Bernstein polynomial degrees 2 (**a**), 3 (**b**), 4 (**c**) and 5 (**d**); displacement applied in x direction

Results in Fig. 20 show again some differences among the strain plots for degrees 1, 2 and 3, while the plots for degrees 3 and 4 look nearly identical. In this case the strain variation is much sharper than in Figs. 18 and 19; the highest strain is about 10 times larger than the lowest one. There are four distinct areas of nearly uniform strains: one of them corresponds to the matrix pocket (highest strain), the second to the filling-directional composite with warp yarn composite below (lower strain), the third to the ‘‘smeared’’ Z-yarn composite (the strain value there is about the same), and the fourth area corresponds to the fill-directional composite with matrix pocket below (the lowest strain is observed there). Also, high strain gradients are visible in the zones between these four nearly uniform strain areas.

Analogous convergence study has been performed for several stress components. The most significant difference is, that the stress variations in this case are much more non-uniform, stress gradients are more pronounced, and some indications of possible singularity points and lines are clearly seen. These effects are illustrated in Figs. 21 and 22.

Figure 21 shows variations of σ_x and σ_z stresses in x-coordinate direction, and Fig. 22 shows their variations along z coordinate. The line along which these variations were plotted in Fig. 21 is the back-top edge of the Mosaic parallelepiped of Fig. 13b. Point $x = 0.344a$ corresponds to the junction of two dissimilar material bricks at free surface. Sharp stress variations and significant differences between stress values computed with polynomial degrees 4 and 5 are seen there. Looks like this may be a singularity point. Note that there is no visible discontinuity of σ_x at that point (this stress component has to be continuous between the bricks), while obvious discontinuity is seen for σ_z (continuity of this stress component is not required). Also, away from that point stress values computed with

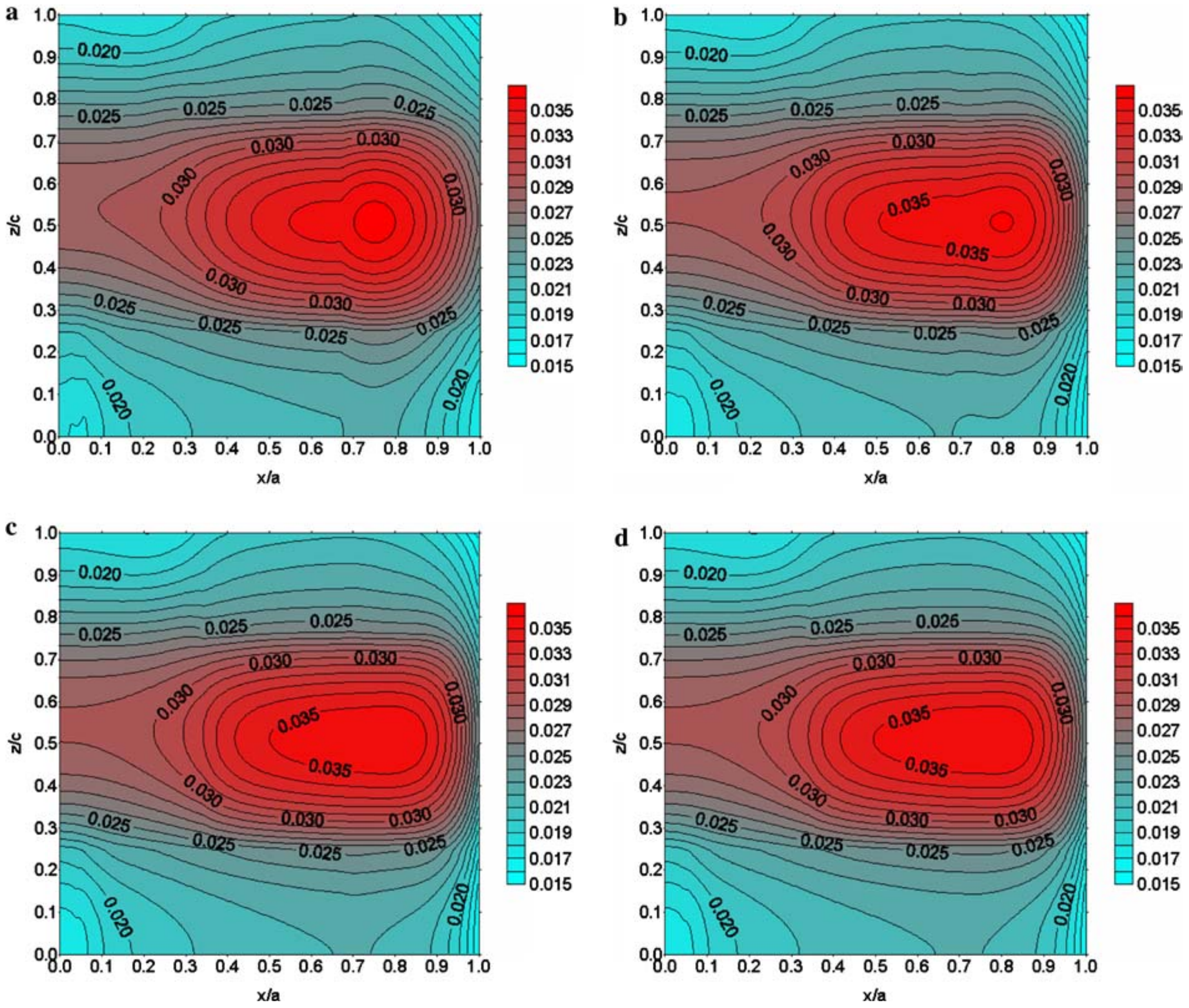

Fig. 19 Distributions of strain ε_y in x–z plane at $y = b$ for Bernstein polynomial degrees 2 (**a**), 3 (**b**), 4 (**c**) and 5 (**d**)

polynomial degrees 4 and 5 are close, and σ_z is close to zero (ideally, it has to be zero at free surface).

The line along which these variations are plotted in Fig. 22 is the right-back edge of the Mosaic parallelepiped of Fig. 13b. It is seen that σ_x variations have sharp peaks and big jumps at two junction points of dissimilar material bricks. Both points are between the filling yarn composite and matrix. The jumps of σ_x seen in Fig. 22a at those points are natural due to significant property difference between unidirectional composite and pure matrix. At the same time, Fig. 22b shows continuous variation of σ_z, as it should be.

We can conclude from numerical results in Figs. 21 and 22 that, at least qualitatively, they are correct. It has to be pointed out that usually the most difficult task of 3-D analysis is to accurately predict stress variations at, or near free surfaces (the classical free edge effect problem for composite laminates is the best-known example of this kind). The lines along the edges of Mosaic parallelepiped with junction points of dissimilar materials have been chosen for illustration intentionally, in order to present most difficult cases.

Stress singularities in the Unit Cell model

Now, after we have revealed that there are possible singularities in the 3-D stress state of the Unit Cell model under consideration, the question is what to do with them. It is not easy to give a simple and satisfactory answer, and the whole issue of stress singularities, which are artificially created when discretizing any textile composite into 3-D blocks of homogeneous materials, deserves separate comprehensive analysis and discussion. Due to limited space here we can afford only short remarks.

First, the analyst has to decide what is the purpose of specific analysis to be performed. If this is prediction of effective elastic properties, then those suspected stress

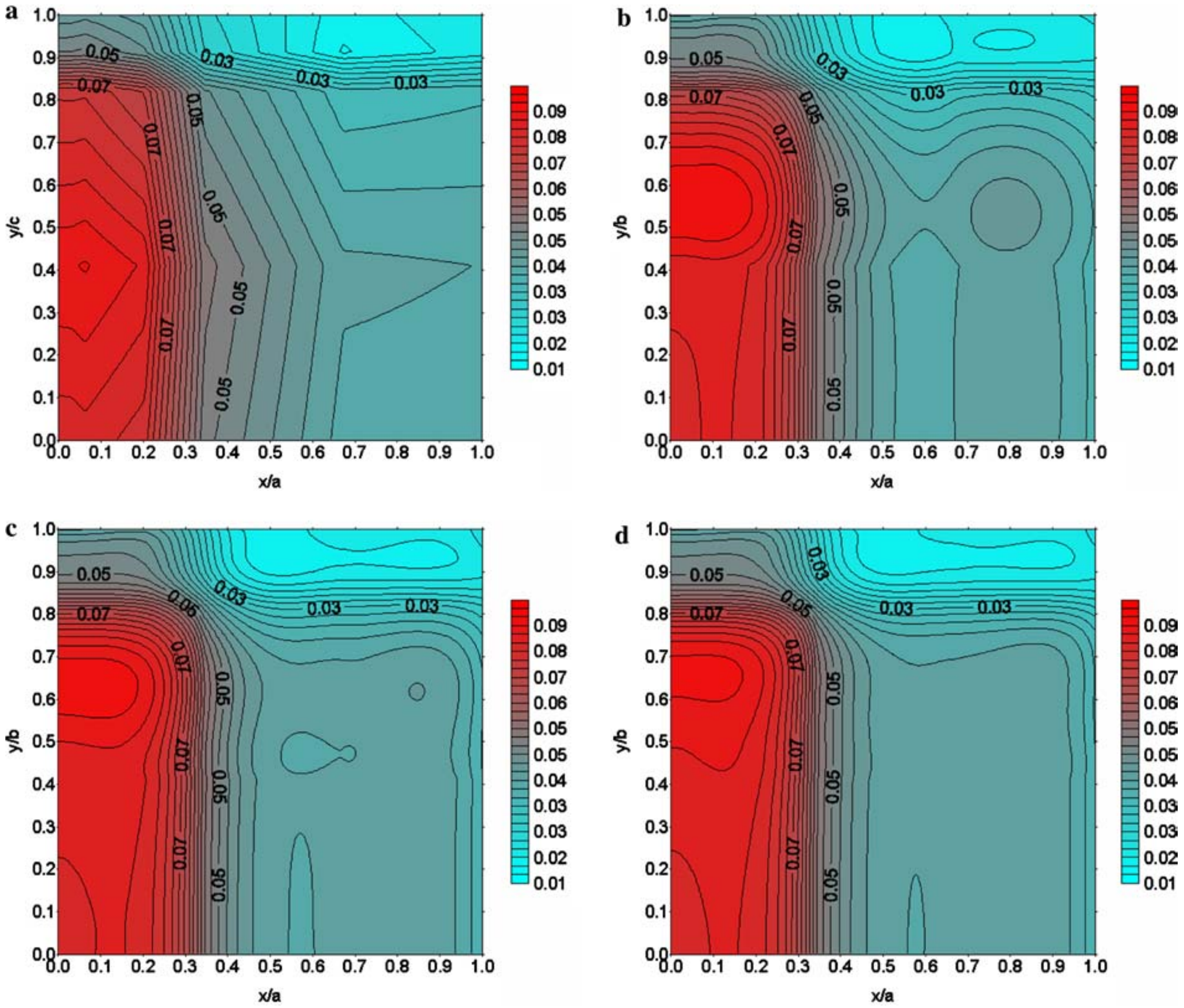

Fig. 20 Distributions of strain ε_z in x–y plane at $z = c$ for Bernstein polynomial degrees 1 (**a**), 2 (**b**), 3 (**c**) and 4 (**d**)

Fig. 21 Variations of σ_x (**a**) and σ_z (**b**) along x coordinate at y=b, z=c for Bernstein basis function degrees 4 and 5

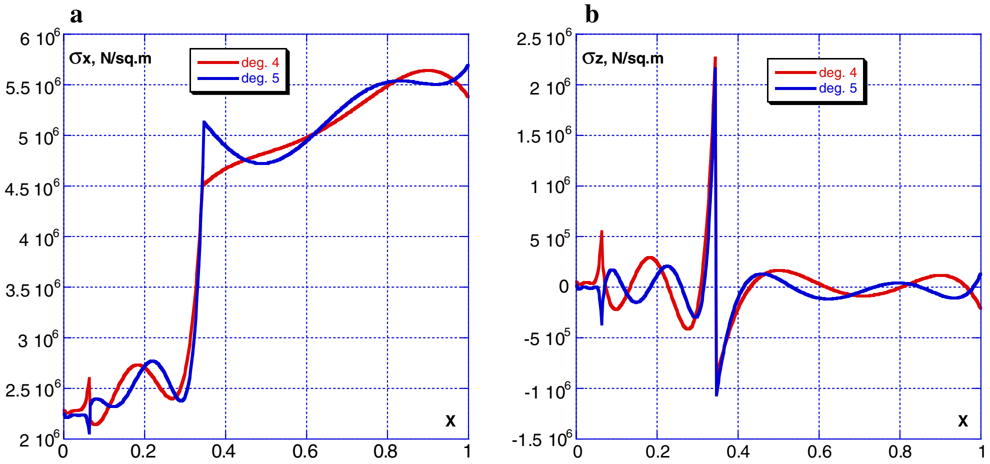

singularities would probably be simply ignored. Indeed, after performing volumetric averaging of stress and strain fields within Mosaic parallelepiped, the contribution of singular stresses in close vicinity of the points or lines of singularity will likely be small, regardless of how accurately their finite-value

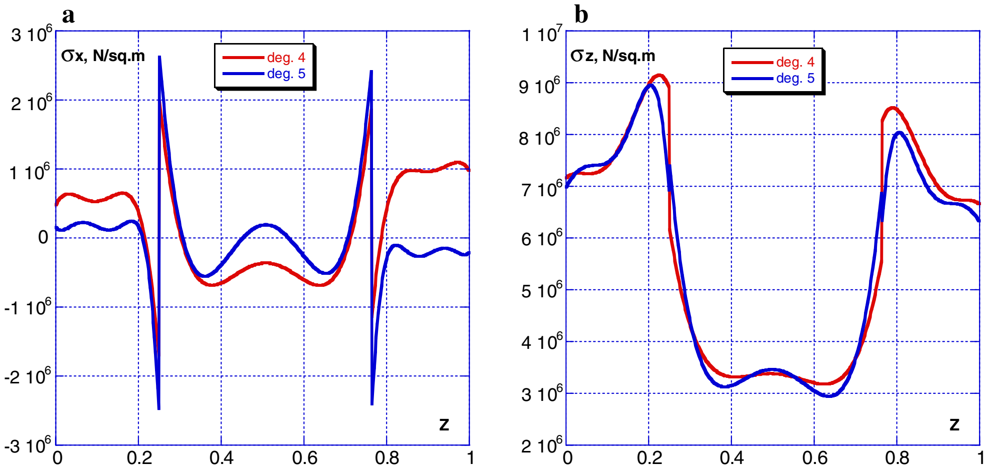

Fig. 22 Variations of σ_x (**a**) and σ_z (**b**) along z coordinate at $x = a$, $y = b$ for Bernstein polynomial degrees 4 and 5

magnitudes have been determined. Next question is, what contribution singular stresses themselves would make. Based on the author's experience from studying numerically stress singularities in several 3-D elasticity problems (including composite bonded joints and composite stiffened panels, where step-wise variations of elastic properties take place) their contribution should also be negligible. Keeping in mind that no mathematical tool is available for analytical determination of the order of singularity in 3-D elasticity problems, the following approach has been used. A close-up stress-coordinate variation was computed in the vicinity of singularity point with increasingly fine computational mesh towards the point. It was found that a sequence of such analysis runs provide converging stress values at some distance from the singularity point. However for some other point, closer to the point of singularity, the stress convergence was not achieved, and further mesh refinement was required. Of course, this process can be continued endlessly with no final success, because in the presence of stress singularity no mesh can provide converged stress exactly at the singularity point. But, having sufficient sequence of stress variations allows one to extrapolate them to the singularity point by some singular analytical function and determine the order of singularity as the best fit to computed finite stresses. Note that the order of stress singularity must to be less than 1 (so-called "weak singularity"), otherwise strain energy stored by elastic body would be infinite.

Further, having an analytical expression for the singular stress, one can integrate it over a very small interval in the vicinity of singularity point and determine what contribution it makes to the total stress integral taken over the length, width or thickness of the solved composite structure. As specific numerical examples showed, the contribution coming from any stress singularity point is negligible. If translating this into the language of volumetric stress averaging methodology described in Section "Volumetric averaging of stress/strain fields in 3-D Mosaic structures", we can expect that the averaged stress will converge with uniformly increasing number of rendering points for any fixed computational mesh or polynomial degree. If, in addition to this, converged results will also be obtained for volumetrically averaged stress when refining computational mesh or polynomial degree, then we can ensure that converged values have been also obtained for effective elastic characteristics.

If the purpose of analysis is predicting initial or progressive failure with the use of some phenomenological failure criterion, then infinite stresses cannot be used, simply because failure of the material would be predicted at infinitesimal load value. Though, extrapolation and averaging of singular stress within some "small interval" around its singularity point (following procedure described in the previous paragraph), would result in a finite averaged stress value that can be used in any phenomenological failure criterion. The only remaining issue with this approach would be that the obtained finite stress value will be sensitive to the length of the averaging interval, so will be the predicted failure load computed at each failure occurrence.

An alternative approach, which may appear more productive, takes into consideration that stress singularities always take place at the interfaces between two or more distinct material bricks at the exterior surfaces, or among three or more distinct material bricks inside Mosaic structure. Using the capability of present approach to incorporate 2-D planar cracks into the model (see Section "Crack propagation modeling"), such cracks can be introduced in the sites of stress singularities. This would allow to re-formulate the problem of singular stresses in ''perfectly bonded'' Mosaic body for the problem of singular stresses at the crack tips in Mosaic body with planar cracks at the interfaces. The latter problem may seem more reasonable mechanistically, though another dilemma arises right a way: according to this logics, the analyst has to introduce small cracks in all singularity sites of Mosaic body, when the structure is exposed even to infinitesimal load level (during handling or shipping, for example). Is such localized cracking under infinitesimal load a reality in textile composites, or we would add another artifact created by the model? It should be obvious from this discussion that there is no perfect solution for all the aforementioned dilemmas, and the next attempt should be in the direction of re-formulating the model itself.

One possible way to re-formulate the model is to dwell into the next lower level of structural hierarchy of the material. Indeed, the above discussed, artificially created stress singularities or ''initial'' interfacial cracks would disappear right after a deeper physical sense is brought into the model. Specifically, each homogenized composite material brick (e.g., textile yarn impregnated with resin) in the Unit Cell model of Fig. 13 consists of thousands and tens of thousands of individual fibers (many of them are in contact) immersed in matrix material. Accordingly, at the fiber-matrix level of hierarchical modeling (illustrated in Fig. 14), there are no more dissimilar bricks of different homogenized composites and matrix, rather there are homogeneous fibers in different directions and matrix filling spaces among them. Now we return to symbolic models of Fig. 2 and face again stress singularities at certain points and lines of the new, much finer model of 3-D woven composite, as discussed in Section ''Meso-volume'' and ''3-D Mosaic'' concepts''. At this point, one can reasonably remind us that graphite, aramid and many other fibers have their own complex micro- and nano-structure (see illustration in Fig. 23) and suggest that the analysis has to be initiated at that next lower level of structural hierarchy. Where, again, we would face new stress singularities. Specifically, each distinct line seen in Fig. 23 inside fibers corresponds to some kind interface between different structural micro-blocks, and stress singularities are possible along those lines.

Chasing stress singularities in the micro- and nano-worlds would only end at the point where the very meaning of ''stress'' is lost. Then, the other fundamental question would arise: how to relate forces acting between atoms and molecules, as considered in Physics, to stresses considered in Continuum Mechanics? This is a very difficult question. Significant efforts in recent years have been by made by several authors to approach this issue from different standpoints, see for example theoretical developments and relevant references in [81, 82]. Our further objective here is more limited and modest: to demonstrate applications of 3-D Mosaic approach at several levels of structural hierarchy to some example problems in which stress singularities should be insignificant. And, importantly, validate theoretical predictions by experimental data.

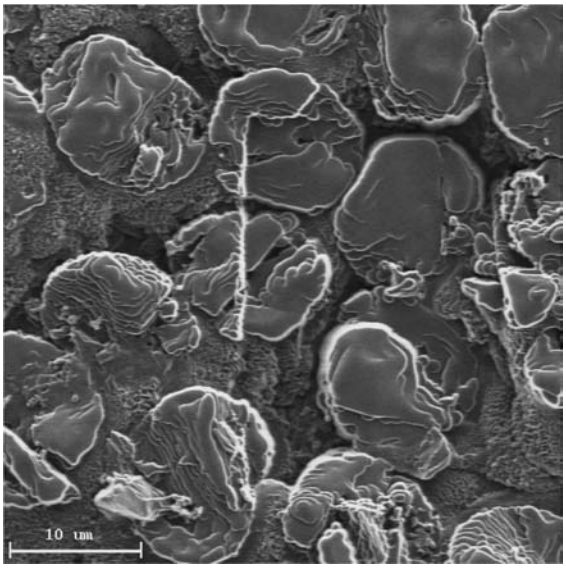

Fig. 23 Cross section of unidirectional T300 carbon fiber/epoxy matrix composite showing fine microstructure within fibers. FEI 610 Focused Ion Beam (North Carolina State University Analytical Instrumentation Facility) was used to sputter away the surface at specified energy level. Courtesy to Dr. Dale Batchelor and Mr. Philip Bradford

Effective elastic property predictions and their experimental verification

Having established certain confidence that 3-D stress/strain fields in the Unit Cell model can be computed with sufficient accuracy when using higher degree Bernstein polynomial basis functions (except for possible points and lines of stress singularity), the methodology of predicting effective elastic properties described in Section ''Volumetric averaging of stress/strain fields in 3-D Mosaic structures'' has been exercised for 3-D woven fabric composite under consideration [18].

After solving all of the necessary 3-D boundary value problems under applied strains and stresses, the computed strain and stress fields have been volumetrically rendered and then averaged. The stress/strain rendering mesh in x, y and z directions was methodically refined, starting from 10 intervals in each direction and ending with 60–80 intervals, until the results for effective elastic constants did not change in first three significant digits. Additionally, the analysis was run for Bernstein basis function degrees 3, 4 and 5. Converged numerical results obtained for the Unit Cell of Fig. 13 with the use of 5th degree Bernstein polynomials are presented in Table 4. Also, for comparison purpose we present in the table theoretical results obtained with SAM and CAM. Theoretical results are complemented in Table 4 by experimental data.

Mechanical characterization of this composite was performed at Institute of Polymer Mechanics (Riga, Latvia) under contract from 3TEX. Elastic and strength characteristics were obtained for the following loading cases applied separately in warp and fill directions: tension (according to ASTM D3039 standard), compression (ASTM D3410), and in-plane shear (following standards ASTM D4255 and ASTM D5379).

Results in Table 1 let us make some comparisons and draw conclusions about the accuracy of different methods in predicting effective elastic properties of 3-D woven composites. First, similar to the SAM/CAM, present analysis enables for predicting upper and lower bounds of effective elastic constants. It is seen from the table that for Young's moduli, the 3-D Mosaic applied strain and applied stress analyses provide much closer bounds than the bounds predicted by SAM/CAM. Further, for the three Young's moduli the upper bounds predicted by present analysis and by SAM are very close. It is also seen that the experimental tensile moduli in warp and fill directions are approximately in the middle between the upper and lower bounds predicted by present analysis. The experimental moduli obtained from compression tests are considerably higher and go beyond the upper bounds. This result is surprising, because it is usually expected that ‘‘compressive'' elastic moduli of textile composite should be lower than the ‘‘tensile'' ones. Other experimental studies of similar 3-D woven S-2 glass composites did not show this ‘‘anomaly''.

Further, the CAM predictions of all Poisson's ratios are higher than the respective SAM results. At the same time, 3-D Mosaic analysis with applied strains predicts one Poisson's ratio lower and the other two Poisson's ratios higher than the respective values predicted by applied stress analysis. Overall, as seen from Table 4, the Poisson's ratios predicted by present analysis and by SAM are sufficiently close. Experimental value of v_{12} is between the present analysis and SAM results. All three shear moduli predicted by 3-Mosaic analysis are significantly higher than the respective values predicted by SAM. Experimental value of G_{12} provided by Two-Rail Shear method is quite close to the present analysis result, while OAM prediction yields significantly lower value.

As an example of more detailed comparison of available theoretical and experimental results, Fig. 24 shows experimental stress–strain curves for five warp-directional and five fill-directional specimens tested for uniaxial in-plane tension. Theoretical results obtained with 3-D Mosaic approach under applied strains or applied stresses, as well as results provided by SAM and CAM are plotted in the figure. It is seen that experimental stress–strain curves for both groups of five specimens go between the upper and lower bounds provided by both analysis tools. The upper bounds predicted by 3-D Mosaic and SAM analyses are very close, while the lower bounds predicted by 3-D Mosaic analysis are significantly higher (and closer to experimental data) than respective CAM lower bounds.

3-D Mosaic simulations of 3-point bending test and their experimental verification

Next example considers 3-point bending test simulation of the same 93oz 3-D woven S-2 glass fiber composite

Table 4 A comparison of predicted and experimental effective elastic constants of 93oz 3-D woven S-2 Glass/Dow Derakane 8084 Epoxy-Vinyl Ester resin composite

Theoretical/ experimental method	Effective elastic characteristics								
	$\langle E_1 \rangle$ GPa	$\langle E_2 \rangle$ GPa	$\langle E_3 \rangle$ GPa	$\langle v_{12} \rangle$	$\langle v_{13} \rangle$	$\langle v_{23} \rangle$	$\langle G_{12} \rangle$ GPa	$\langle G_{13} \rangle$ GPa	$\langle G_{23} \rangle$ GPa
Present analysis (applied strain)	27.31	25.70	9.98	0.125	0.432	0.448	3.58	3.52	3.34
Present analysis (applied stress)	20.59	17.70	9.60	0.134	0.381	0.358	–	–	–
SAM	27.54	24.89	9.72	0.093	0.402	0.402	3.16	3.11	2.98
CAM	14.51	13.13	8.30	0.099	0.425	0.430	3.16	3.02	2.97
Experimental (tension)	24.68	20.75	N/A	0.11	N/A	N/A			
Experimental (compression)	30.82	28.61	N/A	N/A	N/A	N/A			
Experimental (two-rail shear)							3.86	N/A	N/A
Experimental (V-notch beam)							4.50	N/A	N/A

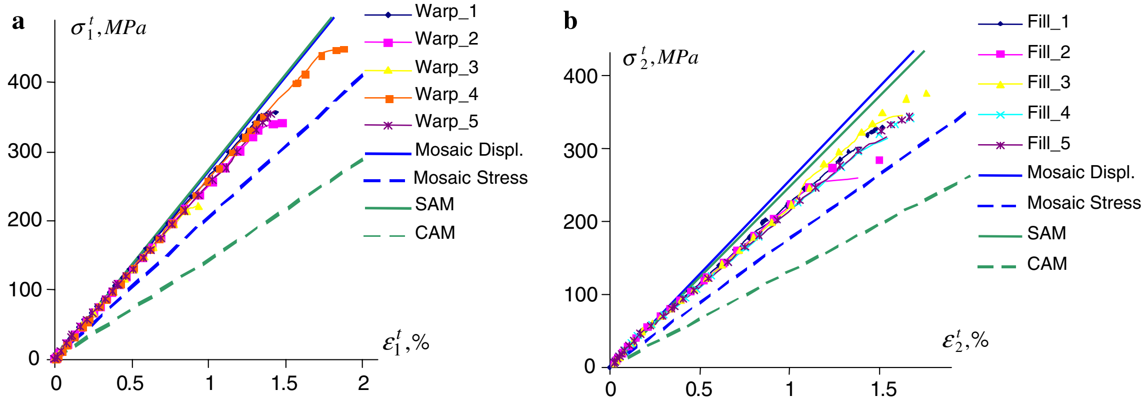

Fig. 24 Experimental and theoretical stress–strain curves for warp-directional (**a**) and fill-directional (**b**) specimens under uniaxial in-plane tensile loading

made with Dow Derakane 8084 Epoxy-Vinyl Ester resin. 3-point bending tests were performed at Institute of Polymer Mechanics (Riga, Latvia) under contract with 3TEX. The test procedures followed ASTM D790 (16:1) standard.

Schematic of a 3-point bending test is shown in Fig. 25. Here, P is surface load intensity (force/area). The acting force is assumed normal to the surface and uniformly distributed over the area $S_{\text{load}} = 2a_4 \times 2b$. Each of the rigid supports has area $S_{\text{sup}} = a_2 \times 2b$. Coordinate axis x goes in longitudinal direction, axis y across the specimen, and axis z in through thickness direction. The boundary condition imposed along each rigid support surface is $u_z = 0$. Owing to the problem symmetry, 1/4th part of the specimen can be solved, with additional symmetry conditions: $u_x = 0$ along cross section $x = a$, and $u_y = 0$ along cross section $y = b$; both cross sections pass through the center of the specimen.

Two different computational models belonging to two hierarchical levels of 3-D woven composite were developed for this analysis. Quarter of a specimen analyzed using "Homogenized Composite Model" (HCM) is shown in Fig. 26. In this model, elastic properties of 3-D woven composite under consideration (as predicted by 3-D Mosaic analysis) are taken from Table 4:

$$\begin{gathered} E_1 = 27.31\,\text{GPa}, \quad E_2 = 25.70\,\text{GPa}, \quad E_3 = 9.98\,\text{GPa}, \\ G_{12} = 3.58\,\text{GPa}, \quad G_{13} = 3.52\,\text{GPa}, \quad G_{23} = 3.34\,\text{GPa}, \\ \nu_{12} = 0.125, \quad \nu_{13} = 0.432, \quad \nu_{23} = 0.448 \end{gathered} \tag{43}$$

Here, material axes 1, 2 and 3 correspond to warp, fill and Z fabric directions and coincide with axes x, y and z of the specimen cut in warp direction. For the specimen cut in fill direction, indices 1 and 2 in (43) have to be interchanged.

Another model named here "Layered Composite Model" (LCM) is shown in Fig. 27. In this model, there are five distinct composite layers in the specimen, each treated as 3-D orthotropic solid. Two of them are reinforced in warp direction, and another three in fill direction. Each of these layers also contains small amount of out-of-plane Z-fiber reinforcement, which is "smeared" together with respective

Fig. 25 Schematics of 3-point bending test simulation

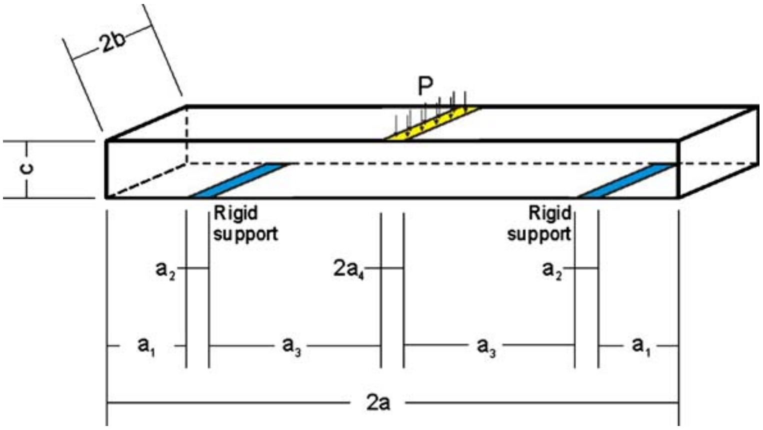

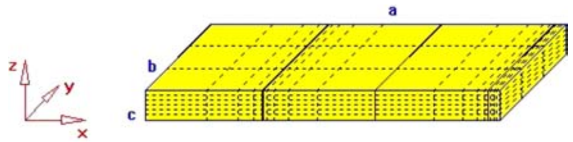

Fig. 26 "HCM" of 93oz S-2 glass 3-D weave composite and computational mesh used in the analysis

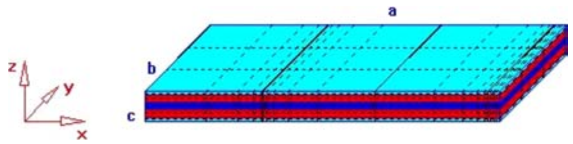

Fig. 27 "LCM" of 93oz S-2 glass 3-D weave composite and computational mesh used in the analysis

major in-plane reinforcement. Thickness of each layer and its fiber volume fraction were calculated using 93oz composite Unit Cell of Fig. 12b. According to that model, both warp layers have equal thickness and equal in-plane fiber volume fraction. Two outer fill layers have equal thickness and equal in-plane fiber volume fraction, while the middle fill layer has different thickness and different in-plane fiber volume fraction. Z-reinforcement was accounted as the second direction reinforcement in the layer, according to Fig. 12b geometry.

The following elastic characteristics were computed for each layer using SAM:

Fill Layers 1 and 5:

$$\begin{aligned}&E_1 = E_3 = 6.78\,\text{GPa}, \quad E_2 = 36.12\,\text{GPa},\\ &G_{12} = G_{23} = 2.54\,\text{GPa}, \quad G_{13} = 2.31\,\text{GPa},\\ &\nu_{12} = 0.055, \quad \nu_{13} = 0.47, \quad \nu_{23} = 0.291\end{aligned} \tag{44}$$

Fill Layer 3:

$$\begin{aligned}&E_1 = E_3 = 9.73\,\text{GPa}, \quad E_2 = 50.25\,\text{GPa},\\ &G_{12} = G_{23} = 3.78\,\text{GPa}, \quad G_{13} = 3.35\,\text{GPa},\\ &\nu_{12} = 0.052, \quad \nu_{13} = 0.453, \quad \nu_{23} = 0.269\end{aligned} \tag{45}$$

Warp Layers 2 and 4:

$$\begin{aligned}&E_1 = 44.45\,\text{GPa}, \quad E_2 = E_3 = 8.31\,\text{GPa},\\ &G_{12} = G_{13} = 3.18\,\text{GPa}, \quad G_{23} = 2.85\,\text{GPa},\\ &\nu_{12} = \nu_{13} = 0.278, \quad \nu_{23} = 0.461\end{aligned} \tag{46}$$

Geometric parameters of the modeled beam specimen, noted in Fig. 25, are:

$$\begin{aligned}&a = 30\,\text{mm}, \quad b = 7.0\,\text{mm}, \quad c = 2.5\,\text{mm},\\ &a_1 = 9.9\,\text{mm}, \quad a_2 = 0.1\,\text{mm}, \quad a_3 = 19.0\,\text{mm}, \quad a_4 = 1.0\,\text{mm},\\ &c_1 = c_5 = 0.292\,\text{mm}; \quad c_3 = 0.614\,\text{mm}, \quad c_2 = c_4 = 0.637\,\text{mm}\end{aligned} \tag{47}$$

In addition to notations introduced in Fig. 25, the following are used here for the LCM: c_1 and c_5 are thicknesses of fill layers 1 and 5, c_3 is thickness of fill layer 3, c_2 and c_4 are thicknesses of warp layers 2 and 4.

First, special computational experiments have been performed to study the effect of support width a_2 on the predicted displacements, strains and stresses. The results showed that for this particular geometry the value a_2 = 0.1 mm is the threshold value, below which changing the support width does not affect numerical results for displacements, strains and stresses outside support area. Another set of numerical experiments showed that a_4 = 1.0 mm is within the range where width of loading nose does not affect results.

Third degree Bernstein basis functions were used in the x, y and z coordinate directions. Computational meshes are shown in Figs. 26 and 27 for HCM and LCM, respectively. In the latter model case, two equal intervals were used through the thickness of each layer. It was shown by convergence study that such through-thickness mesh yields sufficiently accurate predictions of displacements, strains and stresses (with exception for small areas above rigid supports and below loading nose).

Experimental results obtained in 3-point bending tests are shown in Fig. 28a, b for five warp-directional and five fill-directional specimens, respectively. In addition to experimental curves, two theoretical lines are plotted in each figure; those are straight due to linear elastic analysis performed. It is seen that for both groups of five specimens, HCM (red lines) predicts lower central deflection compared to experimental values. The difference is more significant in the case of warp-directional specimens. At the same time, black lines corresponding to LCM perfectly fit in the center among five experimental curves for both groups of warp-and fill-directional specimens.

It is easy to interpret the above results. Obviously, the HCM is insensitive to actual location of the layers of warp and fill yarns through the thickness of 3-D woven fabric composite. When "smearing" warp-directional fibers through the thickness, their contribution to the overall bending stiffness is increased (due to a contribution of individual fiber into overall bending stiffness is proportional to the cube of fiber distance from the specimen mid-plane). Such increase in overall bending stiffness of the warp-directional specimens is caused by smearing, because certain amount of warp fibers get closer to the outer surfaces of the specimen than they actually are. In the case of fill-directional specimens, the two thinner outer filling layers are located farther from the mid-plane in actual composite,

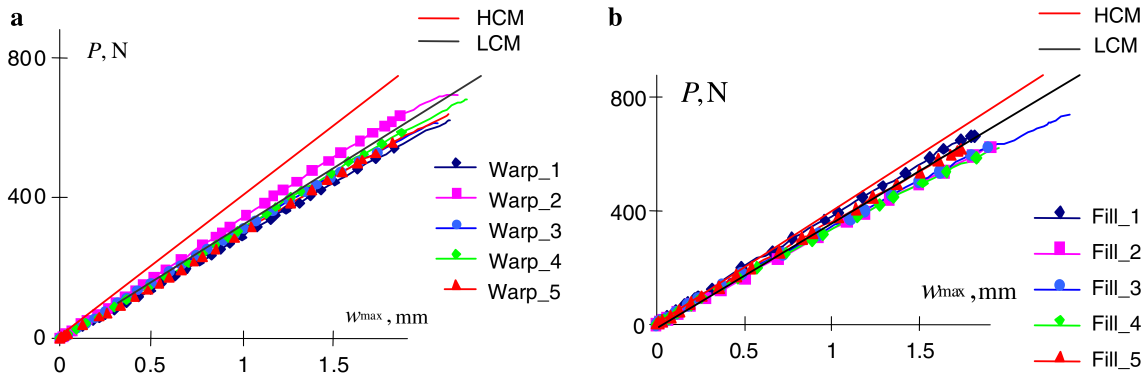

Fig. 28 Experimental load-central deflection curves for five warp-directional specimens (**a**) and five fill-directional specimens (**b**) tested in 3-point bending; theoretical lines show the HCM and LCM predictions

thus their contribution to the overall bending stiffness is underestimated in HCM. At the same time, the counter-effect is that the third (and the thickest) filling yarn layer is located near mid-plane in actual composite, so in HCM its effect on the overall bending stiffness is overestimated.

Results presented in Fig. 28 can be viewed as significant success in modeling 3-D woven composite using 3-D Mosaic analysis approach. Indeed, such excellent agreement with 3-point bending test data was achieved after going through three levels of multi-scale modeling: (i) modeling unidirectional composite and computing its effective elastic properties, (ii) modeling 3-D weave Unit Cell and computing its effective elastic properties, and (iii) 3-D simulation of a "global" 3-point bending problem with the use of LCM or HCM, both utilizing elastic properties of 3-D woven composite based on the Unit Cell model.

Progressive failure modeling of 3-D weave composite Unit Cell

Problem formulation

3-D stress/strain analysis of 3-D woven composite Unit Cell has to be performed as the first step of progressive failure analysis described in Section "Progressive failure analysis using 3-D Mosaic model". The 93oz 3-D woven fabric composite Unit Cell shown in Fig. 13a is used here for a basic illustration of the developed approach. The fiber material is S-2 glass, the matrix material is Dow Derakane 8084 Epoxy-Vinyl Ester resin. Due to the symmetry of this Unit Cell with respect to three orthogonal planes passing through the Unit Cell center, 1/8th part shown in Fig. 13b can be solved instead of the whole Unit Cell. Geometric parameters of the Unit Cell are given in (40).

Uniaxial in-plane tensile loading case is considered here with uniformly distributed displacement u_x^0 applied in x-direction. The following boundary conditions were imposed in the boundary value problem under consideration:

$$\begin{aligned}&u_x = 0 \text{ at } x = 0;\ u_x = u_x^0 \quad \text{at } x = a;\ u_y = 0 \text{ at } y = 0;\\ &u_z = 0 \quad \text{at } z = 0\end{aligned} \tag{48}$$

Initial ("undamaged") elastic characteristics of the constituent materials incorporated in the 3-D weave composite Unit Cell model have been defined above, see Eqs. (41) for matrix and (42) for unidirectional composite.

Another set of input data required for this analysis are ultimate strains of matrix and unidirectional composite in tension, compression and shear. These characteristics were obtained from available literature data for S-2 glass composites with the use of some extrapolations. Specifically, the following ultimate strains were adopted for all unidirectional warp-, fill- and Z-directional composites:

$$\begin{aligned}&\varepsilon_1^T = 2.9\%, \quad \varepsilon_2^T = 0.6\%, \quad \varepsilon_3^T = 0.6\%, \quad \varepsilon_1^C = 1.6\%,\\ &\varepsilon_2^C = 1.8\%, \quad \varepsilon_3^C = 1.8\%, \quad \varepsilon_4^S = 2.0\%,\\ &\varepsilon_5^S = 2.0\%, \quad \varepsilon_6^S = 2.0\%\end{aligned} \tag{49}$$

The following ultimate strains were adopted for matrix material:

$$\begin{aligned}&\varepsilon_1^T = \varepsilon_2^T = \varepsilon_3^T = 2.0\%, \quad \varepsilon_1^C = \varepsilon_2^C = \varepsilon_3^C = 2.5\%,\\ &\varepsilon_4^S = \varepsilon_5^S = \varepsilon_6^S = 3.0\%\end{aligned} \tag{50}$$

For "smeared" bricks containing inclined Z-fiber (axis 1 is oriented in through thickness direction, axis 2 in warp direction and axis 3 in fill direction), the ultimate strains were taken as following:

$$\varepsilon_1^{\mathrm{T}}=2.0\%,\ \varepsilon_2^{\mathrm{T}}=1.5\%,\ \varepsilon_3^{\mathrm{T}}=0.6\%,\ \varepsilon_1^{\mathrm{C}}=1.6\%,\\ \varepsilon_2^{\mathrm{C}}=1.7\%,\ \varepsilon_3^{\mathrm{C}}=1.8\%,\ \varepsilon_4^{\mathrm{S}}=2.0\%,\ \varepsilon_5^{\mathrm{S}}=2.0\%,\ \varepsilon_6^{\mathrm{S}}=2.0\% \tag{51}$$

The above ultimate strain values may be not exactly as they are in the actual 3-D woven fabric composite, yet it is believed that they are close enough to reasonably predict the sequence of major failure events and estimate the ultimate failure load. Yet, if the discrepancy between theoretical and experimental results will be significant, we can ‘‘calibrate’’ the model (by adjusting ultimate strains in the first place).

Another group of input data which have to be specified, are the discount factors entering in Table 1. With no experimental data available, just for illustrative purpose, we take all of them equal 0.1. These values can also be changed when calibrating theoretical predictions against experimental data.

Progressive failure process

After all of the necessary input data have been determined, we can perform numerical simulations of the 1/8th Unit Cell progressive failure process.

The predicted sequence of failure events, obtained from the analysis with ultimate strain values (49)–(51) is illustrated in Fig. 29. Not to surprise, for the loading case under consideration, no failure occurrences have been predicted from compressive or shear strains in the entire course of progressive failure of this 3-D Weave composite. A brief description of the sequence of failure events follows.

First Failure took place in unidirectional Z-reinforced composite brick shown in Fig. 29(a), in *x*-direction (which corresponds to direction 2 in the principal axes of the unidirectional composite; fibers in the failed brick are oriented in the material direction 1). Failure condition $\varepsilon_2^{\mathrm{T}} = 0.6\%$ was satisfied.

Second Failure occurred in unidirectional fill-reinforced composite brick shown in Fig. 29b, in *x*-direction (which corresponds to direction 2 in the principal axes of this material; fibers in the failed brick are oriented in the material direction 1). Failure condition $\varepsilon_2^{\mathrm{T}} = 0.6\%$ was satisfied.

Third Failure is analogous to the Second Failure and has occurred in unidirectional fill-reinforced composite brick shown in Fig. 29c, in *x*-direction. Failure condition $\varepsilon_2^{\mathrm{T}} = 0.6\%$ was satisfied.

Fourth Failure occurred in ‘‘smeared’’ composite brick containing inclined Z-fiber shown in Fig. 29d, in *x*-direction. Failure condition $\varepsilon_2^{\mathrm{T}} = 1.5\%$ was satisfied.

Fifth Failure occurred in matrix brick shown in Fig. 29e, in *x*-direction. Failure condition $\varepsilon_1^{\mathrm{T}} = 2.0\%$ was satisfied.

Sixth Failure occurred in matrix brick shown in Fig. 29f, in *x*-direction. Failure condition $\varepsilon_1^{\mathrm{T}} = 2.0\%$ was satisfied.

Seventh Failure occurred in matrix brick shown in Fig. 29g, in *x*-direction. Failure condition $\varepsilon_1^{\mathrm{T}} = 2.0\%$ was satisfied.

Eighth Failure occurred in warp-reinforced composite brick shown in Fig. 29h, in *x*-direction (which is direction 1 in the principal axes of this unidirectional composite). Failure condition $\varepsilon_1^{\mathrm{T}} = 2.9\%$ was satisfied.

Stress re-distribution and effective moduli reduction

After the Eighth Failure had occurred, in accordance with adopted elastic property reduction scheme, elastic moduli of all constituent bricks lost 90% of their value in *x* direction, which resulted in approximately 90%

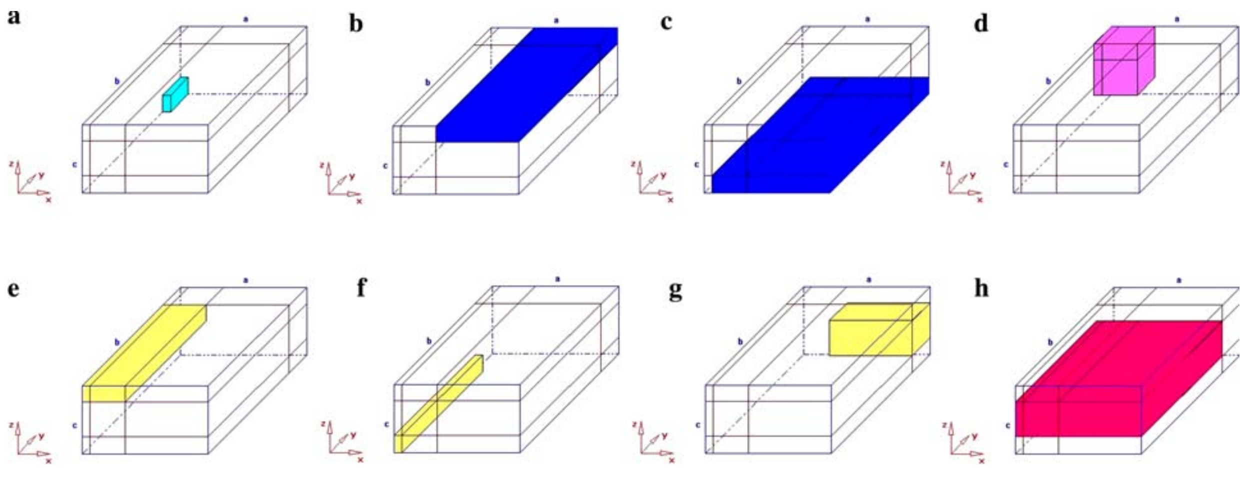

Fig. 29 Illustration of the predicted sequence of failure events

drop of effective elastic modulus $\langle E_1 \rangle$ of the Unit Cell in that direction. Progressive failure analysis was terminated at that point, under assumption that the composite Unit Cell has totally lost its load-bearing ability in that direction.

The following plots presented in Fig. 30 illustrate the computed re-distribution of σ_x stress at the loaded surface $x=a$ in the initial (prior to the first failure) state of the Unit Cell and after some of the failure occurrences. For comparison purpose, in all of the cases the applied displacement was taken $u_x^0 = 0.05$ mm, which corresponds to $\varepsilon_x^0 = 2.165\%$. Obviously, all of the intermediate failures have occurred prior to reaching this strain level.

When comparing Fig. 30a and b, it is seen that significant drop of the stress took place in the areas occupied by the two fill-reinforced bricks. Figure 30c illustrates a visible drop of stress in the area occupied by a large resin brick, which is located to the right from the warp yarn brick. Finally, after failure of the major load-bearing element (the warp yarn brick), the stress distribution becomes very similar to the initial one, as comparison of Figs. 30a and d shows. However, the stress level in case (d) is substantially lower than in case (a).

It is also informative to compare the maximum and average σ_x magnitudes for the four aforementioned states of the Unit Cell. The maximum stress values are: 1.167 GPa (a), 1.204 GPa (b), 1.211 GPa (c) and 0.1216 GPa (d). Therefore, the reduction of x-directional moduli in all other material bricks by 10 times has resulted in only 4.4% overstress on the warp-reinforced brick. The respective computed average $\langle \sigma_x \rangle$ values are: 0.5903 GPa (a), 0.5134 GPa (b), 0.5048 GPa (c), and 0.0619 GPa (d). Residual effective modulus of the composite in x-direction then is estimated by simple equation $\langle E_1 \rangle = \langle \sigma_x(a) \rangle / \varepsilon_x^0$. By substituting the above determined $\langle \sigma_x \rangle$ values together with the value $\varepsilon_x^0 = 0.02165$ in this equation, one obtains the following estimates for $\langle E_1 \rangle$: 27.26 GPa (a), 23.71 GPa (b), 23.32 GPa (c), and 2.86 GPa (d). Therefore, after all eight failure occurrences, effective modulus of this composite in the loading direction has dropped down to 10.5% of its initial value.

Strength predictions

Results provided by the progressive failure analysis also enable for predicting strain values corresponding to initial and ultimate failures. In the performed analysis, initial failure had occurred under applied displacement $u_x^i = 0.0128$ mm, which corresponds to initial failure strain $\varepsilon_x^{iT} = 0.554\%$. The respective initial failure stress in the warp direction of 3-D woven composite is then estimated as $\sigma_x^{iT} = \langle E_1 \rangle \varepsilon_x^{iT} = 151$ MPa. Then, the ultimate tensile failure strain was predicted as $\varepsilon_x^{uT} = 2.165\%$, which corresponds to the ultimate tensile stress value $\sigma_x^{uT} = 679$ MPa, if using initial effective elastic modulus 27.26 GPa. However, before the final, eighth failure, this effective elastic modulus has been already discounted down to 23.32 GPa value. Accordingly, it is more correct to use this modulus for calculation of the

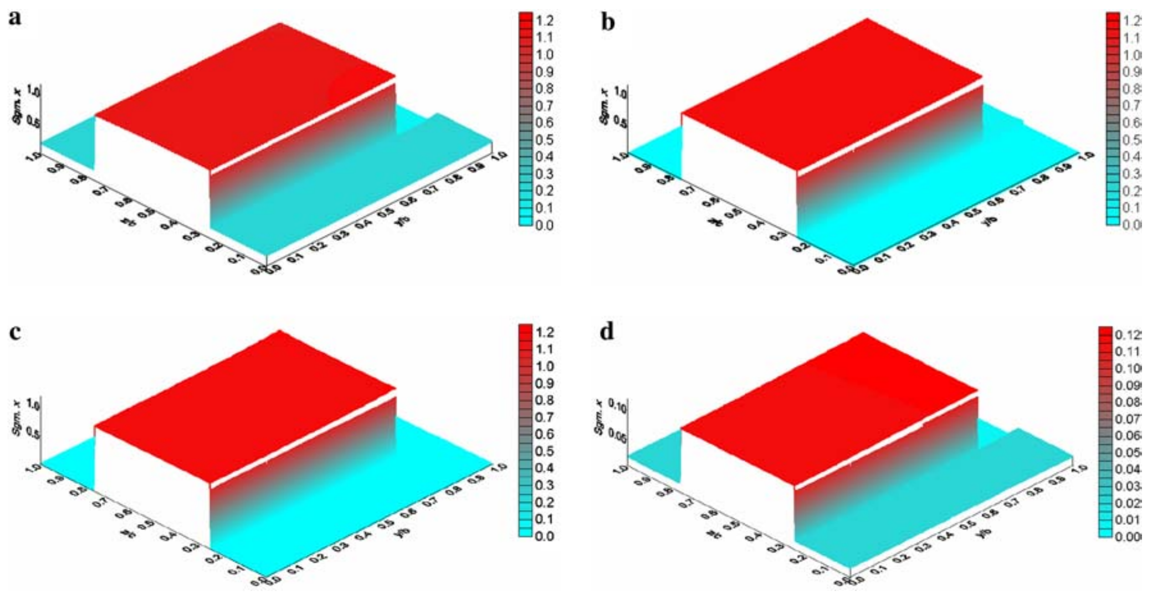

Fig. 30 Distributions of σ_x in y–z plane at $x = a$ prior to First Failure (**a**), after Third Failure (**b**), after Seventh Failure (**c**), and after Eighth Failure (**d**)

ultimate failure stress, which yields $\sigma_x^{uT} = 581$ MPa. A relatively large difference between these two strength estimates can be reduced by increasing discount factor values.

The predicted strength values now can be compared with experimental result for the warp-directional tensile strength available for this 3-D woven composite, which is 717 ± 24 MPa. The experimental value is slightly higher than the strength predicted with the initial modulus, and significantly higher than the strength predicted with the discounted one. So, the comparison suggests that first, the assumed ultimate strains, primarily those in (49), were taken too low, especially considering that ultimate strain of S-2 glass fiber is about 5%. Specifically, the ultimate strain value 2.9% was taken for unidirectional S-2 glass Vinyl Ester-Epoxy composite from the literature, not from mechanical characterization of this material. Secondly, the adopted discount factors, all equal 0.1, are too low, especially in this analysis where discounts were applied to entire meso-volume bricks after each failure event. It is not difficult to make both aforementioned adjustments of the input data (“calibrate” the model) in order to get as close as desired agreement between theoretical and experimental strength values.

Analogously, the progressive failure analysis can be performed for in-plane tension in fill and Z directions, then for all three compressive loading cases, and then for all three shear loading cases. After “calibrating” all of the model predictions against their respective experimental counterparts, a full set of basic strength characteristics would be predicted for 3-D woven composite under consideration. Then, having those basic strength characteristics, one would be able to use them as input data for any higher hierarchical level failure analysis of structural parts made from this 3-D woven composite.

The value of having “calibrated” theoretical results for all “elementary” loading cases is, that they would identify those values of the input ultimate strains (49)–(51) and discount factors (Table 1) for constitutive material blocks which brought theoretical predictions in desirable agreement with experimental data for this particular 3-D woven composite. After that, the same ultimate strains and discount factors can be used in strength predictions of many other 3-D woven composites built from the same material blocks. The fact that predictive analysis results perfectly matched experimental data for one of them, would provide confidence that theoretical prediction for the others will be sufficiently accurate. Results of such combined theoretical–experimental study for 3-D woven S-2 glass fiber composites will be reported elsewhere.

Progressive failure analysis tool based on 3-D Mosaic model and variational analysis approach can be applied to any type of multi-axial, complex loading; either displacements or stresses may be independently imposed at each exterior surface element. Any kind of composite material or structure, which is suitable for modeling in terms of generic 3-D Mosaic parallelepiped of Fig. 1 can be analyzed by use of current version of computer code possessed by 3TEX. The analysis approach has also been extended to dynamic loading with 3-D transient stress/strain fields analyzed, progressive failure process simulated, and dynamic failure loads predicted.

Conclusions

This paper presented principal aspects of hierarchical, multi-scale 3-D Mosaic structural analysis tool, including its methodological concepts, theoretical background, computational algorithms, and demonstration of its capability to solve complex and diverse 3-D stress/strain, failure and fracture mechanics problems for textile composites. It is believed that this transparent analysis approach, based on a very elegant mathematical theory with consistent utilization of mechanistically justified material models, has gained its place among other available 3-D structural analysis tools. The approach is opened to various new generalizations, can be formulated as either 3-D Ritz-type variational analysis approach or 3-D *p*–*s*-type combined hexahedral 8-noded finite element with Bernstein shape functions. The developed software package can be easily included into other finite element codes.

Another goal pursued in this work was to present historic retrospect and state-of-the-art assessment in the area of modeling and analysis of textile composites, with the focus on 3-D woven composites. General theoretical backgrounds and specific modeling and analysis approaches thoroughly discussed here often contain inherent contradictions and inconsistencies, which may be hidden in complex details of computational algorithms, but show in the results one way or the other. Those subtle aspects of modeling and analysis of textile composites were brought here to open discussion, which should motivate and facilitate future developments of computational models and analysis methods.

Specific problems solved, numerical results presented, and practical conclusions and recommendations made in this paper may be useful for generating property database for textile composites, which is on enormous demand from the industry. One area, where 3-D woven composites find fast growing interest and practical applications, is ballistic armor and blast mitigation systems; generating reliable material property database for them is of a great importance. Yet, there are very few theoretical studies reported up to date on computational modeling and analysis of 3-D woven composites under impact, ballistic and blast effects, see [22–26]. 3-D Mosaic approach has been extensively used in modeling impact and blast effects of 3-D woven composites, sandwich panels with 3-D woven composite skins, and some other relevant material systems. Some results of those studies can be found in [22, 24, 26]. Also, attempts were made to quantify progressive damage of 3-D woven S-2 glass composites during ballistic penetration [24] and perforation [25] at the Unit Cell level. Commercial finite element code LS-DYNA was used in the latter two works. Particularly, [25] presented, probably, first attempt ever to predict exit velocity of projectile after ballistic perforation of 3-D woven composite, based on mechanistic, not phenomenological approach. A comparison of theoretical results with ballistic test data presented in that work is encouraging. This direction of research is fast growing, and many new results are expected in the near future.

Acknowledgments Current version of computer code 3-D MOSAIC used in this work for generating numerical results was developed by Intelligent Software Solutions, Inc. (Raleigh, North Carolina, USA) under contracts from 3TEX, Inc. The author is especially grateful to Mr. Alexander Birger for continuous assistance and technical support in the code utilization. The author is grateful to Dr. Dmitri Mungalov (3TEX) for valuable assistance in processing numerical results and illustrative material preparation. Special credits to Dr. Vladimir Kulakov and Mr. Alexander Arnautov (Institute of Polymer Mechanics, Riga, Latvia), who performed mechanical characterization of 3-D woven composite under contract from 3TEX, Inc. and provided experimental results included in his work.

References

1. Bogdanovich AE, Singletary JN (2000) In: Proceedings of European conference on composite materials ECCM9, June 4–7. CD publication, Brighton, UK
2. Singletary JN, Bogdanovich AE (2001) In: Proceedings of the 46th international SAMPE symposium and exhibition, Long Beach, CA, May 6–10, vol 46, Book 1. SAMPE publication, pp 835–846
3. Mohamed MH, Bogdanovich AE, Dickinson LC, Singletary JN, Lienhart RB (2001) SAMPE J 37(3):8
4. Dickinson L, Mohamed M (2000) In: Proceedings of the ASME Aerospace Division, AD-vol 63, Book No. H01214-2000, pp 3–8
5. Singletary J, Bogdanovich A, Coffelt R, Gama BA, Gillespie JW Jr, Hoppel CPR, Fink BK (2001) In: Proceedings of the American Society for Composites, 16th technical conference, September 9–12. CD publication, Blacksburg, VA
6. Stobbe D, Mohamed M (2003) In: Proceedings of 48th international SAMPE symposium, May 11–15, 2003. SAMPE Publication, Long Beach, CA, pp 1372–1380
7. Mohamed M, Schartow R, Knouff B (2003). In: Proceedings of 48th international SAMPE symposium, May 11–15. SAMPE Publication, Long Beach, CA, pp 1714–1726
8. Mohamed MH, Bogdanovich AE, Coffelt RA, Schartow R, Stobbe D (2005) In: CD proceedings of the textile institute 84th annual world conference, March 22–25, Raleigh, NC
9. Bogdanovich A, Coffelt R, Grogan J, Shukla A (2005) In: CD proceedings of the 26th international SAMPE Europe conference, Paris, France, April 5–7, pp 245–250
10. Tamuzs V, Tarasovs S, Bogdanovich A, Singletary J (2002) In: Book of abstracts, 3rd ESIS TC4 conference on polymers and composites, fracture of polymers, composites and adhesives, Les Diablerets, Switzerland, September 15–18
11. Tamuzs V, Tarasovs S, Vilks U, Bogdanovich A, Singletary J (2002) In: Booklet of abstracts, 10th European conference on composite materials (ECCM-10), Brugge, Belgium, June 3–7
12. Tamuzs V, Tarasovs S, Vilks U (2003) Compos Sci Technol 63:1423
13. Masters JE, Ifju PG, Pastore CM, Bogdanovich AE (1992) In: Proceedings of third NASA advanced composites technology conference, June 8–11, 1992, Long, Beach, CA. NASA Conference Publication 3178, Part 2, pp 523–536
14. Pastore CM, Bogdanovich AE, Gowayed YaA (1993) Compos Eng 3(2):181
15. Bogdanovich AE, Pastore CM (1996) Mechanics of textile and laminated composites. Chapman & Hall, London
16. Weissenbach G (2004) Issues in the analysis and testing of textile composites with large representative volume elements. Dissertation.com, Boca Raton, Florida, USA
17. Bogdanovich AE (2003) Innovative materials for lightweight armor – Phase II annual progress report. Under Contract DAAD17-01-C-0086, Army Research Laboratory, ARL-CR-524, June 2003
18. Bogdanovich AE (2003) In: Proceedings of 35th international SAMPE technical conference, vol 35, Dayton, OH, September 28–October 2, 2003
19. Bogdanovich A (2004) In: Proceedings of the 25th Jubilee international SAMPE Europe conference, Paris, France, March 30–April 1, 2004, pp 393–398
20. Desplentere F, Lomov SV, Woerdeman DL, Verpoest I, Wevers M, Szucs P, Bogdanovich A (2003) In: Proceedings of 48th Int. SAMPE symposium and exhibition, May 11–15, vol 48, Book 2. SAMPE Publ., Long Beach, CA, pp 1335–1347
21. Desplentere F, Lomov SV, Woerdeman DL, Verpoest I, Wevers M, Bogdanovich A (2005) Compos Sci Technol 65:1920
22. Bogdanovich AE, Yushanov SP (2000) Compos Part A: Appl Sci Manuf 31A(8):795
23. Bogdanovich AE, Yushanov SP (1999) In: Proceedings of The American Society for composites, fourteenth technical conference, September 1999, Dayton, OH, pp 151–160
24. Gama BA, Haque MdJ, Gillespie JW Jr, Bogdanovich AE (2004) In: CD Proceedings of 49th international SAMPE symposium and exhibition, May 16–20, 2004. SAMPE publication, Long Beach, CA
25. Gama BA, Bogdanovich AE, Coffelt RA, Haque MdJ, Rahman M, Gillespie JW Jr (2005) In: CD Proceedings of SAMPE'05 conference, Long Beach, CA, May 1–5

26. Bogdanovich AE (2005) Book of abstracts, 3rd international conference on structural stability and dynamics (ICSSD), Kissimmee, FL, June 19–22, 2005
27. Fowser S, Wilson D (1986) In: Proceedings of 3-D composites, working-group meeting sponsored by NASA Langley Research Center and the Department of the Navy, Annapolis, Maryland, November 5–7, 1985. NASA Conference Publication 2420, pp 91–108
28. Ko FK (1989) In: Chou T-W, Ko FK (eds) Chapter 5 in Textile structural composites, composite materials series, vol 3. Elsevier Science Publishers B.V., Amsterdam, pp 129–171
29. Byun J-H, Chou T-W (1990) J Textile Inst 81(4):538
30. Chou T-W (1992) Microstructural design of fiber composites. Cambridge University Press, Cambridge, England
31. Tarnopol'skii YuM, Zhigun IG, Polyakov VA (1992) Spatially reinforced composites. Technomic Publishing, Lancaster-Basel
32. Bogdanovich AE, Pastore CM (1992) In: Proceedings of the ASME summer mechanics and materials conferences, Tempe, AZ, April 28–May 1, 1992, Topics in composite materials and structures (V. Birman and A. Nagar eds.). The ASME publication, AD-vol 26, AMD-vol 133, pp 13–19
33. Bogdanovich AE, Pastore CM (1994) In: Proceedings of the 1994 international mechanical engineering congress & exhibition, Chicago, IL, November 6–11, 1994. The ASME publication, Reprint 94-WA/AERO-3, pp 1–12
34. Hartranft D, Pravizi-Majidi A, Chou T-W (1995) In: Proceedings of mechanics of textile composites conference sponsored by the NASA, Hampton, VA, December 6–8, 1994. NASA Conference Publication 3311, Pt. 2, October 1995, pp 251–313
35. Cox BN, Dadkhah MS (1995) J Compos Mater 29(6):785
36. Cox BN, Carter WC, Fleck NA (1994) Acta metall mater 42(10):3463
37. Xu J, Cox BN, McGlockton MA, Carter WC (1995) Acta Metall Mater 43(9):3511
38. Ishikawa T, Watanabe N, Bansaku K, Ono Y (1997) In: Proceedings of the 11th int. conference on composite materials (ICCM-11), Gold Coast, Australia, 14–18 July 1997, pp 189–200
39. Tan P, Tong L, Steven GP (1997) Compos Struct 38(1–4):261
40. Tan P, Tong L, Steven GP (1997) Compos Part A: Appl Sci Manuf 28:903
41. Yushanov SP, Bogdanovich AE, Mohamed MH (1999) In: Proceedings of the 12th annual technical conference of the ASC, October 1997, Dearborn, MI. Also in J Thermoplastic Compos Mater 12(1):70
42. Naik RA, Jarmon DC, Weeks CA, Logan CP (1998) In: Proceedings of the 43rd int. SAMPE symposium and exhibition, Anaheim, CA, May 31–June 4, 1998, vol 2. SAMPE publication, pp 2057–2069
43. Tan P, Tong L, Steven GP (1998) J Reinforced Plastics Compos 17(6):545
44. Tan P, Tong L, Steven GP (1999) J Reinforced Plastics Compos 18(2):151
45. Tan P, Tong L, Steven GP (2000) Compos Part A: Appl Sci Manuf 31:273
46. Swan CC, Kim HJ, Lakes RS (2000) In: Proceedings of the 41st AIAA/ASME/ASCE/AHS/ASC Structures, structural dynamics, and materials conference and exhibit, Atlanta, GA, 3–6 April, 2000. Paper A00-24798, AIAA-2000-1783, pp 1–7
47. Yushanov SP, Bogdanovich AE (2000) Mech Compos Mater 36(4):501
48. Zuorong C, Shouwen Y, Xiqiao F, Lu M, Ye L (2002) Compos Part B: Eng 33:241
49. Kregers AF, Melbardis YG (1978) Polym Mech 14(1):3
50. Kregers AF (1979) Mech Compos Mater 15(5):790
51. Kregers AF, Teters GA (1979) Mech Compos Mater 15(4):617
52. Kregers AF, Teters GA (1981) Mech Compos Mater 17(1):30
53. Kregers AF, Teters GA (1982) Mech Compos Mater 18(1):14
54. Lagzdins A, Tamuzs V, Teters G, Kregers A (1992) Orientational averaging in mechanics of solids. John Wiley & Sons
55. Tarnopol'skii YM, Polyakov VA, Zhigun IG (1973) Polym Mech 9(5):853
56. Abolinsh DS (1966) Polym Mech 2(3):372
57. Pastore CM (1993) Compos Manuf 4(4):217
58. Brandt J, Drechler K, Arendts F-J (1996) Compos Sci Technol 56(3):381
59. Yushanov SP, Bogdanovich AE (1998) Int J Solids Struct 35(22):2901
60. Bogdanovich AE (1992) In: Proceedings of the IUTAM symposium "local mechanics concepts for composite material systems", Blacksburg, VA, 28–31 October 1991. Springer-Verlag, Berlin-New York, pp 355–382
61. Bogdanovich AE (1993) In: Proceedings of the sixth conference on advanced engineering fibers and textile structures for composites, FIBER-TEX 1992, Philadelphia, PA, October 27–29, 1992, NASA Conference Publication 3211, pp 271–304. Also Compos Manuf 4(4):173
62. Bogdanovich AE, Pastore CM (1996) Compos Sci Technol 56:291
63. Bogdanovich AE, Pastore CM, Birger AB (1993) In: Proceeding of the ninth international conference on composite materials, Madrid, Spain, July 1993, vol 4, Composites design. Woodhead Publishing Limited, pp 495–501
64. Pastore CM, Bogdanovich AE, Birger AB (1992) In: Proceedings of the 2nd international symposium on textile composites in building construction, Lion, France, 1992. Part 2. Textiles, fibres, composite materials and structures. Editions Pluralis, Paris, France, pp 35–44
65. Bogdanovich AE, Pastore CM, Greenhalgh ES, Birger AB (1993) In: Proceedings of the American Society for composites, eighth technical conference, Cleveland, OH, October 1993. Technomic Publishers, pp 851–861
66. Bogdanovich AE (1993) In: Advanced composites'93, international conference on advanced composite materials, Wollongong, Australia, February 1993. A Publication of TMS Minerals/Metals/Materials, pp 79–91
67. Bogdanovich AE, Birger AB (1992) In: Proceedings of The ASME winter annual meeting, symposium on damage mechanics in composites, Anaheim, CA, 1992, AMD-vol 150/AD-vol 32. The ASME Publication, pp 275–293
68. Bogdanovich AE, Birger AB (1993) In: Proceedings of the 1st joint mechanics meeting of ASME/ASCE/SES, symposium on non-classical problems of the theory and behavior of structures exposed to complex environmental conditions, Charlottesville, VA, June 1993, AMD-vol 164. The ASME Publication, pp 155–167
69. Bogdanovich AE, Birger AB (1994) Comput Struct 52(2):237
70. Bogdanovich AE (1994) In: Proceedings of the American Society for composites, ninth technical conference, Newark, DE, September 1994. Technomic Publishing Co., Lancaster, PA, pp 1168–1181
71. Bogdanovich AE, Pastore CM, Deepak BP (1995) Compos Eng 5(9):1105
72. Bogdanovich AE, Deepak BP (1997) Compos Part B 28B(4):345

73. Bogdanovich AE, Yushanov SP (2000) Compos Sci Technol 60(12–13):2407
74. Bogdanovich AE (2000) Comput Methods Appl Mech Eng 185(2–4):279
75. Bogdanovich AE (2001) Mech Compos Mater 37(5/6); Pt. 1, p 525; Pt. 2, p 539
76. Bogdanovich AE, Yushanov SP (1998) In: Proceedings of the 39th AIAA/ASME/ASCE/AHS/ASC Structures, structural dynamics, and materials conference and exhibit, April 1998, Long Beach, CA. AIAA Publication, Part 3, pp 1616–1626, Paper A98-25163
77. Bogdanovich AE, Yushanov SP (1999) J Reinforced Plastics Compos 18(18):1689
78. Bogdanovich AE, Yushanov SP (2000) In: Proceedings of 21st international conference SAMPE Europe 2000, April, Paris. SAMPE Publication, Markus A. Erath (Editor), pp 547–558
79. Davis PJ (1975) Interpolation & approximation. Dover Publications, Inc., New York
80. Mohamed MH, Zhang Z-H (1992) Method of forming variable cross-sectional shaped three dimensional fabrics. U.S. Patent No. 5,085,252, issued February 4
81. Shen SP, Atluri SN (2004) CMC – Comput Mater Continua 1(1):59
82. Shen SP, Atluri SN (2004) CMES: Comput Model Eng Sci 6(1):91